Morphology and Crystal Orientation of

Ferroelectric P(VDF-ran-TrFE)

Nanostructures in Porous Aluminium Oxide

Dissertation

zur Erlangung des akademischen Grades

Dr. rer. nat.

vorgelegt dem
Institut für Physik der Naturwissenschaftlichen Fakultät II
der Martin-Luther-Universität Halle-Wittenberg

von

Nitin Shingne

geboren am 07.01.1979 in Amravati, Indien

Gutachter:

1. Prof. Dr. Thomas Thurn-Albrecht, MLU

2. Prof. Dr. Jörg Kreßler, MLU

3. Prof. Dr. Bernd Stühn, TU Darmstadt

Eröffnung des Promotionsverfahrens: 17. December 2010

Öffentliche Verteidigung: 27. April 2011

Contents

Chapter 1

Introduction

Ferroelectric materials are commonly used in memory devices of cell phones, cameras, radio frequency identification (RFID) and due to their pyroelectric and piezoelectric properties in sensors and actuators for a wide range of applications. Inorganic ceramics are the most common materials being used in ferroelectric applications [1–3]. However, with the discovery of ferroelectricity in poly(vinylidene fluoride), PVDF, in 1969 and further development of new ferroelectric polymers especially poly(vinylidene fluoride-trifluoroethylene), P(VDF-TrFE), led to applications of the ferroelectric polymers in electronics, acoustic devices, sensors and actuators [4]. Increasingly ferroelectric materials are sought for new applications in nanotechnology, like ferroelectric random access memory (FeRAM), nanoscale sensors and actuators which need lower power with better sensitivity. We have studied ferroelectric P(VDF-TrFE) nanostructures, prepared by using porous anodic aluminium oxide (AAO) templates. The practical applications of the ferroelectric nanostructures depend on the crystal orientation and morphology of the nanostructures. Therefore basic understanding of the morphology and crystal orientation in the 2D confinement of the AAO templates is of fundamental interest towards making fully functional polymer ferroelectric devices. Furthermore, ferroelectric P(VDF-TrFE) is a semi-crystalline polymer, confining it to the nanoscale can lead to important changes in the structure which we want to investigate.

Many important structural changes in the polymers takes place at the nanoscale and confining the polymers to the nanoscale can put a new light on our understanding of the polymer properties. For example, molecular chain dynamics, the length scale that is responsible for glass transition, T_g, lamellae thickness and microphase separation in block copolymers happens at nanoscale and confining the polymer is an important way to study these properties.

It was shown that the block copolymers confined in AAO nanopores show different morphologies than that can be observed in the bulk. For the block copolymers in the AAO nanopores, it was argued that the cylinders with high degree of curvature imposed on the planar lamellar morphology of block copolymers causes a frustration of chain packing at the interface which lead to different morphologies [5,6]. Study of T_g is also an active area of research to explain the dynamics of glass transition and substrate polymer interaction at the nanoscale [7–9]. Another area of interest in nano-confinement is polymer crystallization, crystal orientation and polymorphic phases. It was shown that in 2-dimensional (2D) confinement of AAO template, PVDF crystallites have preferential orientation with c-axis parallel to the template surface. It was argued that the crystal growth kinetics lead to the preferred orientation [10]. Also, it was shown that crystallization of PVDF in AAO nanopores lead to changes in polymorphic α-form to the γ-form [11]. The crystallization of PEO sandwiched between multilayered coextruded film with confinement of 20 nm showed lamellae with high aspect ratio resembling single crystals and having two orders of magnitude of reduction in gas permeability [12].

To study the effect of confinement on polymers, the confinement can be achieved by various methods. Self assembly of block copolymers where one block forms different morphologies like cylinder, spheres or lamellaes in a matrix of another block is one of the system to study the confinement effects. Polymer crystallization and orientation in block copolymers where the crystallisable block is confined into an amorphous matrix have been studied extensively [13–15]. Polymer thin films is also an area where the confinement effects on the chain conformation, glass transition and melting temperature of polymers have been studied [8, 16]. Park et al. have prepared thin films of P(VDF-TrFE) by spin coating on a substrate and studied the confinement effect on ferroelectric polarization and effect of different substrates on the orientation of the crystallites [17,18]. Another way to fabricate confined polymer nanostructures by using AAO template was shown by C.R. Martin and also by Steinhart et al. [19, 20]. This method of producing nanostructures is very useful as it provides arrays of nanostructures with precisely adjustable aspect ratios. Different kinds of polymers can be used to form the nanostructures and different infiltration mechanism like melt, solution or direct polymerization inside the AAO nanopores can be chosen [21]. A Variety of interesting properties have been studied using the porous alumina templates. Apart from some of the examples mentioned above, porous alumina templates are also used to study the Rayleigh instabilities and crystal orientation of polyethylene inside the nanopores, hypersound propagation in polymer/AAO nanocomposite, nanorods arrays for biosensing, etc [22–25].

The P(VDF-TrFE) confined into AAO nanopores have been studied by

Lutkenhaus et al., they have shown enhancement in ferroelectric phase in the confinement with the crystals having preferred c-axis orientation parallel to the template surface [26]. Wang et al. have shown that the spontaneous polarization in P(VDF-TrFE) nanotubes, prepared by using AAO template, can be switched under the electric field [27]. Hu et al. have prepared P(VDF-TrFE) nanocells using nano-embossing, it was shown that in the nanocells the P(VDF-TrFE) crystals have preferred orientation with a and c axes oriented in the plane of the substrate with b axis orientation perpendicular to the substrate. The piezoresponse force microscope measurements showed the ferroelectric properties of the nanocells [28].

Despite the recent progress in understanding the ferroelectric P(VDF-TrFE) in confinement, there are many questions which remain unanswered. In this research work we have studied the development of morphology of P(VDF-TrFE) nanostructures inside the AAO nanopores. The relationship between crystal orientation and morphology was also studied. Another important aspect of P(VDF-TrFE) are the phase transitions. The ferroelectric to paraelectric phase transition (Curie transition), melting and crystallization of the P(VDF-TrFE) nanostructures were studied by differential scanning calorimetry. There are studies which show that the annealing of P(VDF-TrFE) in the paraelectric phase leads to increase in lamellae thickness and decrease in the Curie transition temperature, T_C [29–32]. But it is not known if the lamellae thickness have a direct effect on the T_C. The P(VDF-TrFE) confined in the AAO nanopores gave us a unique way to restrict the lamellae thickness and then study its effect on the T_C. Furthermore, the important task was to find out how the ferroelectric dipoles are oriented in the nanostructures because this is the most important criteria which decides the ferroelectric properties of the nanostructures. Wide angle x-ray scattering (WAXS) was used to find out how the crystallites are oriented in the P(VDF-TrFE) nanostructures. This work shows the preferred orientation of the polar b-axis, along which the dipoles are oriented, in the P(VDF-TrFE) nanostructures. The driving force for the preferred orientation is also discussed. Further, the relationship between the morphology, extent of confinement and the crystal orientation in the nanostructures is analyzed. We have also studied how the preferred orientation of the P(VDF-TrFE) crystallites develops during the crystallization in the paraelectric phase and then during the phase transition from paraelectric phase to the ferroelectric phase using temperature dependent WAXS. We hope that the new insight we gained in the crystal structure and morphology of the P(VDF-TrFE) nanostructures will lead to development of the fully functional ferroelectric polymer nanostructures.

Chapter 2

Sample System: P(VDF-TrFE)

2.1 Ferroelectric Polymers

'Ferroelectrics are materials in which the unit cell of the crystal is polar and the direction of polarization can be changed by the application of electric field' [33]. Ferroelectric materials are also piezoelectric and pyroelectric. A polar structure with some instability is important for a material to be ferroelectric. The instability is essential to make the spontaneous polarization reversible. The polarity arises from the dipole moment associated with charge separation between adjacent atoms. In polymers the dipole moment arises between the covalently bonded atoms along the polymer chain or between adjacent chains [34].

Ferroelectricity in polymers was discovered in the late 1970s in Polyvinylidene fluoride (PVDF). The formation of highly polar bonds between fluorine and carbon atoms coupled with all trans chain conformation which leads to the orientation of the dipoles in one direction is responsible for the ferroelectricity of the PVDF in the ferroelectric β-phase. However, PVDF directly crystallized from the melt does not show ferroelectricity and is non polar because PVDF shows polymorphism with four different crystalline forms. Direct crystallization from melt leads to formation of non-polar α-phase. The highly polar β-phase is obtained by special treatments like stretching the polymer under electric field [35]. This particular drawback lead to the suggestion that addition of TrFE (trifluoroethylene) unit into PVDF could induce direct crystallization into the ferroelectric β-phase [36]. In the poly(vinylidene fluoride-ran-trifluoroethylene), P(VDF-TrFE), copolymer because of the similar size of the hydrogen and fluorine atoms, VDF and TrFE units are randomly distributed along the molecular chain to form a random copolymer that co-crystallize into a single crystalline phase sim-

ilar to PVDF ferroelectric β-phase. This gives the copolymer application advantage over the homopolymer. Also the addition of TrFE unit lead to increase in the crystallinity of the copolymer. The P(VDF-TrFE) copolymer in 50 - 80 mol% of VDF content shows Curie transition, related to phase transition between ferroelectric and paraelectric crystalline phases. The ferroelectric properties and Curie temperature are affected by TrFE content in P(VDF-TrFE) [36–38].

2.2   P(VDF-ran-TrFE)

P(VDF-TrFE) is a random copolymer of vinylidene fluoride (VDF) and tri-fluoroethylene (TrFE), the repeating unit of P(VDF-TrFE) is shown in figure 2.1. Figure 2.2 shows the orthorhombic unit cell (lattice parameters: a = 9 $\mathring{A}$, b = 5.16 $\mathring{A}$ and c = 2.55 $\mathring{A}$) of ferroelectric phase of the P(VDF-TrFE), as shown all the fluorine atoms are oriented along the b-axis of the unit cell [34]. This lead to polarization of the dipoles along the b-axis, in figure 2.2 the dipole orientation is indicated by the arrows.
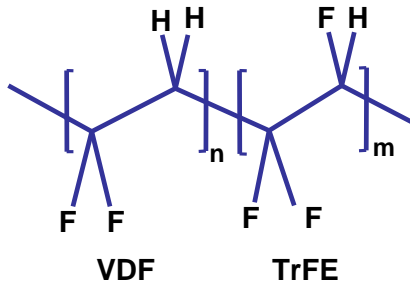

Figure 2.1: Repeating unit of poly(vinylidene fluoride-ran-trifluoroethylene)
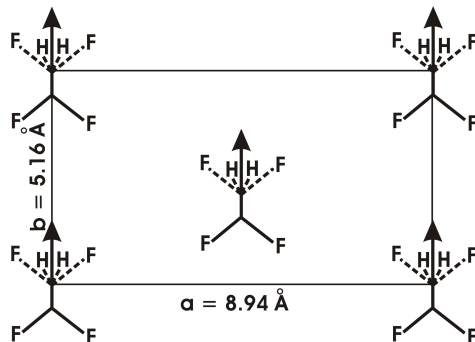

Figure 2.2: Unit cell of poly(vinylidene fluoride-ran-trifluoroethylene)

P(VDF-TrFE) shows Curie transition temperature which is typical, but not necessary, characteristic of ferroelectric materials. In the ferroelectric phase the copolymer is in all trans configuration with all dipoles pointing

6

perpendicular to the chain axis which renders it with the ferroelectricity. In the paraelectric phase the chains are highly mobile and the configuration changes from all trans to trans-gauche-trans-gauche conformation and the dipoles are rotating around the chain axis therefore the copolymer looses its ferroelectricity. Figure 2.3 shows the P(VDF-TrFE) lattice in the paraelectric hexagonal phase and low temperature, ferroelectric pseudo-hexagonal phase. The main planes are also indicated in the lattice by considering an orthorhombic unit cell in both the phases. By cooling the sample from the paraelectric phase to the ferroelectric phase, below the Curie temperature, the lattice parameter a is decreased and the hexagonal symmetry is lost. The Curie temperature is thus characteristic of the ferroelectric materials at which the polar ferroelectric phase is transformed into a non-polar paraelectric phase.

Previous studies have shown that the transformation of the copolymer into the ferroelectric phase always occur through the hexagonal phase. That is, it is not possible to crystallize the copolymer directly into the ferroelectric phase without going through the hexagonal phase. In the study the copolymer was directly quenched to the low temperature (ferroelectric phase) from the melt and it was observed that initially the melt is always transformed into the hexagonal phase and then to the ferroelectric orthorhombic phase. This behavior was attributed to Oswald state rule: the thermodynamically unstable but kinetically preferable high temperature phase can appear first even when the thermodynamically more stable low temperature phase should be created [39].

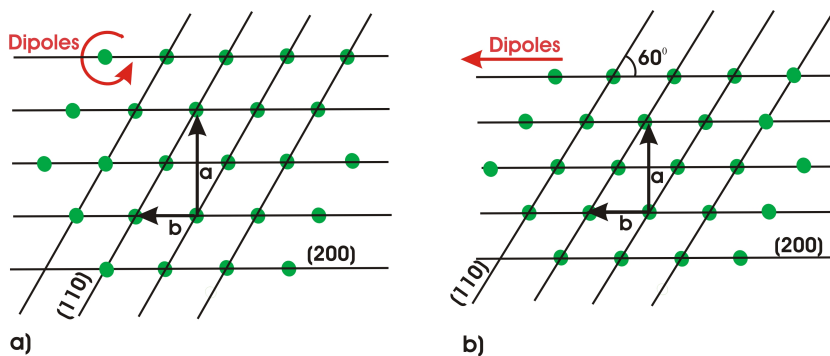Apart from the ferroelectric low temperature phase and paraelectric high

Figure 2.3: Lattice of the P(VDF-TrFE) showing the main planes in a) paraelectric hexagonal phase and b) ferroelectric pseudo-hexagonal phase. In both the phases an orthorhombic unit cell is considered.
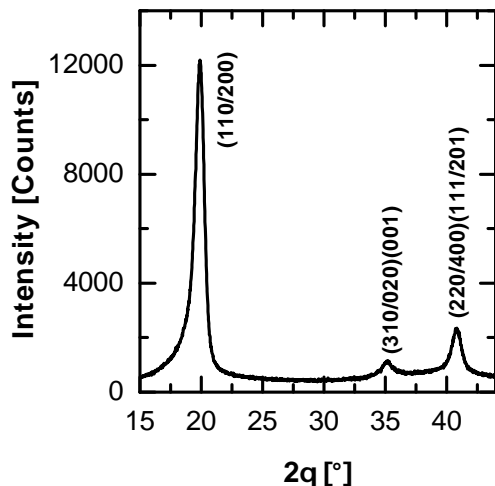
Figure 2.4: X-ray diffraction pattern of bulk P(VDF-TrFE) with 70 mol% VDF

temperature phase a third crystalline phase called the 'cooled phase' is observed for the copolymer with VDF content between 50 - 65 mol%. Cooled phase is composed of mixture of low temperature pase and high temperature phase with disordered chain conformations which are frozen during cooling from the high temperature phase. The cooled phase can be observed in the x-ray scattering by the broadness of the (110/200) peak. Also, the DSC scan during heating shows a first peak for ferroelectric to cooled phase transformation and a second peak, before melting, for cooled phase to paraelectric phase transformation [37, 40]. Our polymer which has 70 mol% VDF does not show the cooled phase.

The figure 2.4 shows x-ray diffraction pattern of bulk P(VDF-TrFE) at room temperature. The x-ray pattern shows three prominent peaks for 2θ angles between 15-45°. Due to the pseudo-hexagonal symmetry of the crystal lattice there are multiple reflection at the same Bragg's angle.

2.2.1 Characterization of P(VDF-TrFE)

The P(VDF-TrFE) sample in the form of granules was provided by Piezotech, SA, France. The company did not provide the specifications of the P(VDF-TrFE) sample therefore we carried out GPC and NMR measurements to determine the molecular weight and the ratio of VDF and TrFE units.

2.2.2 SAXS Measurements

In P(VDF-TrFE) the lamellae thickness is quite high. Small angle x-ray scattering measurements performed by different research groups have shown that the long period, lamellae thickness plus the amorphous thickness, in

8

P(VDF-TrFE) varies in the range of 20 nm (as cast) to 400 nm (annealed in paraelectric phase) depending on the annealing conditions [41–43]. The sample with 73/27 mol% VDF/TrFE, cooled from $170°C$ with a cooling rate of 1 K/min to room temperature shows a long period of 110 nm with crystallinity of 93% [41]. The high lamellae thickness is the result of the highly mobile paraelectric phase in P(VDF-TrFE). The molecular chains in the paraelectric phase can slide along the chain direction leading to the thickening of the lamellae. Annealing in the paraelectric phase can also lead to extended chain crystals (ECC) [43, 44].

We want to study the crystallization of P(VDF-TrFE) in the AAO nanopores with the diameters ranging from 35 nm to 400 nm. The large lamellae thickness in bulk P(VDF-TrFE) will be restricted in the confinement provided by the AAO nanopores. Therefore, it is necessary to know the lamellae thickness in the P(VDF-TrFE) to determine the confinement effects on the lamellae. In order to determine the lamellae thickness of the P(VDF-TrFE) SAXS measurements were carried out on a slowly cooled sample and on a sample quenched in nitrogen. The cooled sample was prepared by heating the P(VDF-TrFE) to $200°C$ and allowing it to cooled in the furnace to room temperature. The quenched sample was prepared by reheating the cooled sample to $200°C$ and then putting it into liquid nitrogen. The SAXS measurements were carried out with a Kratky compact camera in transmission geometry. $CuK\alpha$ radiation with wavelength of 1.5405 $\mathring{A}$ was used. Figure 2.5 shows the desmeared SAXS pattern for the cooled and quenched bulk P(VDF-TrFE) sample. The cooled sample does not show any peak in the SAXS pattern which indicate that the long period is larger than 100 nm, which is the resolution of the SAXS. The quenched sample shows a peak corresponding to the long period of 45 nm. The SAXS pattern is plotted on a double logarithmic
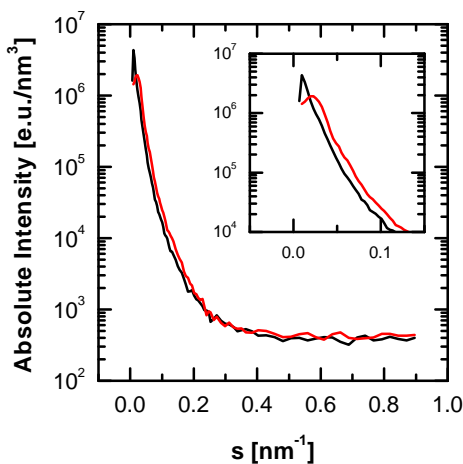
Figure 2.5: Desmeared SAXS intensity for slowly cooled bulk PVDF-TrFE (black curve) and quenched bulk PVDF-TrFE (red curve)
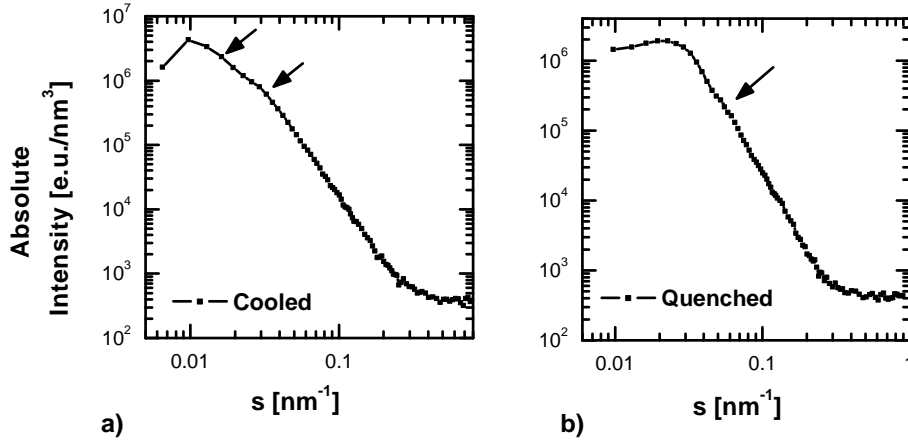
Figure 2.6: Desmeared SAX intensity for bulk P(VDF-TrFE) plotted on a double logarithmic scale, a) cooled and b) quenched samples. The arrows point the shoulder on the SAXS patterns corresponding to higher orders.

scale in figure 2.6. The cooled sample in the plot, figure 2.6 a, does not show the main peak but shows two shoulders corresponding to the higher orders of the main peak. The higher orders suggest that the long period of cooled P(VDF-TrFE) should be 125 nm. This confirms that the cooled P(VDF-TrFE) has a large lamellae thickness. The quenched sample, figure 2.6 b, shows a peak corresponding to 45 nm of long period and the higher order shoulder indicated by a arrow.

2.2.3 Gel Permeation Chromatography: Molecular Weight

Gel permeation chromatography (GPC) was performed to characterize the molecular weight of the P(VDF-TrFE). Dimethylformamide (DMF) was used as a solvent and calibration was done with polystyrene as a standard. The GPC results are shown in table 2.1.

Sample	M_n (g/mol)	M_w (g/mol)	M_w/M_n
P(VDF-TrFE)	100008	209740	2.09

Table 2.1: Molecular weight of P(VDF-TrFE) measured by GPC

2.2.4 Themogravimetric Analysis

The P(VDF-TrFE) nanostructures samples were prepared by melting the polymer at $200°C$ and $250°C$ and it was necessary to know that the P(VDF-TrFE) does not degrade in this temperature range. Therefore thermogravitemetry analysis (TGA) was carried out with Mettler Toledo TGA/SDTA851 on the P(VDF-TrFE) sample. The sample was heated with 1 K/min and mass of the sample was recorded. Figure 2.7 shows the mass of P(VDF-TrFE) against temperature. The figure shows that the mass of P(VDF-TrFE) start decreasing at $400°C$. This means that degradation of the P(VDF-TrFE) begins at $400°C$, the sample is completely degraded at around $500°C$. The degradation temperature is well above the temperature of $250°C$ at which the samples were prepared.
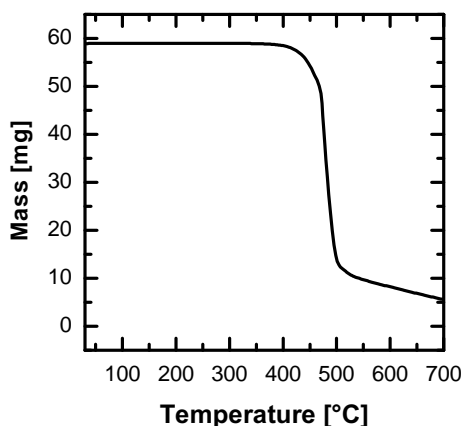
Figure 2.7: TGA of P(VDF-TrFE), the mass of the sample starts decreasing at $400°C$

2.2.5 Nuclear Magnetic Resonance

The composition of the VDF and TrFE units in the P(VDF-TrFE) was determined by hydrogen NMR, H-NMR. Protonated acetone was used as a solvent for the P(VDF-TrFE) and proton NMR spectra was measured. The area under the peak for the TrFE and VDF unit shows a ratio of 1:6.7. The H-NMR is sensitive to the presence of hydrogen atoms. Since the VDF unit contain two hydrogen atoms and the TrFE unit contain one hydrogen atom, the VDF peaks will be twice as strong as the peaks corresponding to the TrFE unit. Therefore, the ratio of TrFE to VDF unit is 1:3.35. This gives the composition of 30:70 for TrFE:VDF in the P(VDF-TrFE) sample. The NMR spectra from the P(VDF-TrFE) is attached in the appendix-II.

11

2.3 P(VDF-TrFE) Nanostructures: Sample Preparation

Nanoporous anodic aluminium oxide (AAO) was used to fabricate the P(VDF-TrFE) nanostructures. The AAO templates were prepared by two step anodization process as described in reference [20,45]. The AAO nanopores show well ordered honeycomb structure. They are mechanically stable and chemically inert in the temperature range necessary for the formation of polymer nanostructures [21]. Pore diameter of 35 nm, 60 nm 180 nm and 400 nm with pore depth of 100 μm was used to prepare the P(VDF-TrFE) nanostructures. A anodic aluminium oxide template of 400 nm diameter is shown in figure 2.9.

The P(VDF-TrFE) nanostructures were prepared by wetting of the AAO template at certain wetting temperature. The wetting temperature is the temperature at which the polymer melt infiltration is carried out. The wetting of P(VDF-TrFE) was carried out in a precision furnace. The furnace consist of a cylindrical sample chamber, the temperature of which was controlled by an Eurotherm V2604 temperature controller. The furnace can be operated in inert atmosphere, it is connected with a vacuum pump and argon supply. Initially the bare AAO template was put into the furnace connected to a vacuum pump and the temperature was raised to the chosen wetting temperature so that the moisture from the template is removed. After 10 minutes at the wetting temperature, P(VDF-TrFE) granules were put on the template and the polymer melt was spread on the surface by a spatula. The polymer was then allowed to wet the template for a certain amount of wetting time, as shown in figure 2.9 *a*. The polymer was then crystallized by cooling it with a cooling rate of 1 K/min to 30 °C. During the wetting and cooling of the sample vacuum is constantly applied. Two types of the samples were prepared. In one case after the wetting process the samples were allowed to cool in the presence of the bulk surface film on the template surface, these are
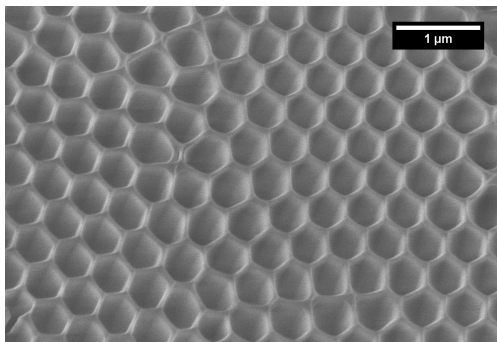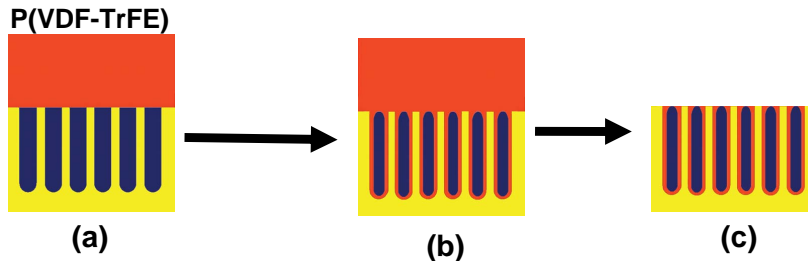

Figure 2.8: Empty pore of 400 nm

Figure 2.9: P(VDF-TrFE) nanostructures preparation: a) melting of the P(VDF-TrFE) granules on the template surface, b) the polymer is allowed to crystallize with surface film and c) crystallization of the polymer without surface film

called *samples with surface film*. Second type of samples were prepared by taking the samples with surface film and then the surface film on the samples was removed with the help of a scalpel. The sample was then put into the furnace and the temperature was raised to $200°C$ for 10 minutes and then the sample was cooled with a cooling rate of 1 K/min to $30°C$, this type of sample is called *sample without surface film*. For the samples with surface film, the bulk polymer film is in contact with the nanostructures inside the AAO nanopores as shown in figure 2.9 *b*. For the samples without surface film each nanostructure crystallizes separately as shown in figure 2.9 *c*.

Quenched samples were prepared by removing the sample from the furnace directly to the room temperature.

Samples for x-ray diffraction

For the x-ray diffraction measurements the surface film of the samples was removed and aluminium edges of the AAO templates were cut.

Samples for DSC

For DSC measurements, the surface film was removed from the samples as well the aluminium base was etched away by the copper chloride solution. The copper chloride solution consist of 1.7 gm of $CuCl_2.H_2O$, 50 ml concentrated HCl and 50 ml deionized water. The whole solution containing the template was placed in a water/ice mixture in order to remove the exothermic heat. The solution dissolves the aluminium and only alumina (Al_2O_3) matrix embedded with P(VDF-TrFE) remains. A piece of 5 mm diameter was cut from the alumina-P(VDF-TrFE) sample to put inside the DSC pan.

Samples for TEM analysis

For TEM analysis the first step is to remove the aluminium from the AAO template (as done for the DSC) after that the alumina matrix has to be dissolved to get the individual nanotubes/nanorods. Following steps were followed to get the individual nanostructures

1. the PVDF-TrFE embedded inside the alumina was placed in a 40 mol% KOH solution for 20 minutes

2. after dissolving the alumina the solution was kept in a centrifuge for 10 minutes at 140 revolutions/minute

3. the solution was removed from the centrifuge and a small mass of the nanostructures were accumulated at the bottom of the small bottle, the KOH was removed from the bottle

4. distilled water was added to the bottle containing the nanostructures and vigorously mixed, again the mixture was put into the centrifuge for 10 minutes and excess water was removed

5. step 4 was repeated for three more times

6. finally distilled water was added and mixed with the nanostructures, afterwards with the help of pipet a small droplet of the solution was added on the TEM grid to deposit the nanostructures for observations

Samples for SEM analysis

For the SEM observations, gold was sputtered on the sample under vacuum for 30 seconds with deposition current of 30 mA. Some samples were broken along the pore axis in order to observe the cross-section of the samples.

Chapter 3

Experimental Methods

Various characterization methods were used for the determination of the morphology, phase transitions and the orientation of the P(VDF-TrFE) nanostructures.

3.1 X-Ray Diffraction

X-ray diffraction was performed on the P(VDF-TrFE) nanostructures by using a Phillips X'pert diffractometer. $CuK\alpha$ radiation with wavelength of 1.5405 Å was used. Further details about the diffractometer are discussed in chapter 4.

3.1.1 Bragg Formulation of X-Ray Diffraction by Crystals

In crystalline materials, for certain sharply define wavelengths, incident and diffraction directions, intense peaks of scattered radiation can be observed. W. L. Bragg accounted for this by regarding a crystal as made out of parallel planes of atoms/molecules, spaced a distance 'd' apart. The conditions for a sharp peak in the intensity of the scattered radiation are,

1. that the x-rays should be specularly reflected, i.e. the angle of incidence equals the angle of reflection, by the atoms/molecules in any one plane and

2. that the reflected rays from successive planes should interfere constructively
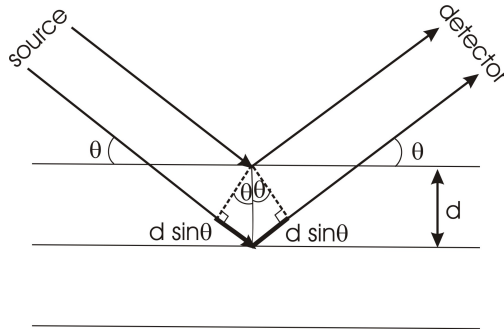
Figure 3.1: Bragg reflection from particular family of lattice planes

Rays specularly reflected from adjacent planes are shown in figure 3.1. The path difference between the two rays is $2dsin\theta$, where θ is the angle of incidence [46]. For the rays to interfere constructively, this path difference must be an integral number, n, of wavelengths, λ, leading to the Bragg condition,

$$n\lambda = 2dsin\theta \qquad (3.1)$$

3.1.2 Von Laue Formulation of X-ray Diffraction by a Crystal

In the van Laue approach one regards the crystal as composed of identical microscopic objects (sets of ions or atoms) placed at the sites R of a Bravais lattice, each of which can reradiate the incident radiation in all directions. Sharp peaks will be observed only in directions and at wavelengths for which the rays scattered from all lattice points interfere constructively.

To find the condition for constructive interference, consider a plane incident wave (figure 3.2) traveling in the direction specified by the unit vector $\mathbf{S}_0$ is scattered by the particles located at two points, O and P. A detector is placed in the direction specified by the unit vector $\mathbf{S}$ at a distance far from these scattering centers. If the scattering is coherent and there is no
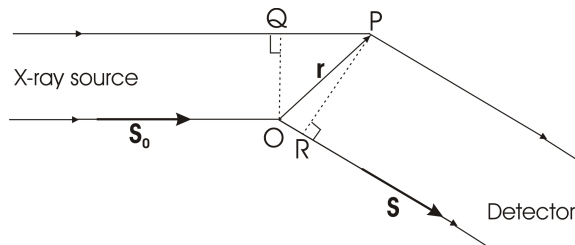

Figure 3.2: Geometry of path length difference

phase change on scattering, the phase difference $\Delta\phi$ between the two waves scattered at O and P and arriving at the detector depends only on the path length differences δ between the two rays,

$$\Delta\phi = \frac{2\pi\delta}{\lambda} \tag{3.2}$$

Designating the position of the second scatterer relative to the first as $\mathbf{r}$, we have

$$QP = \mathbf{S}_0 \cdot \mathbf{r} \tag{3.3}$$

$$OR = \mathbf{S} \cdot \mathbf{r} \tag{3.4}$$

And therefore the phase difference is,

$$\Delta\phi = \frac{2\pi}{\lambda}(\mathbf{S}_0 \cdot \mathbf{r} - \mathbf{S} \cdot \mathbf{r}) \tag{3.5}$$

$$\Delta\phi = -2\pi\mathbf{s} \cdot \mathbf{r} \tag{3.6}$$

where,

$$\mathbf{s} = \frac{\mathbf{S} - \mathbf{S}_0}{\lambda} \tag{3.7}$$

Diffraction will be observable only when the scattering vector $\mathbf{s}$ coincides with one of the reciprocal lattice vector, that is

$$\mathbf{s} = \mathbf{r}^\star_{hkl} = h\mathbf{a}^\star + k\mathbf{b}^\star + l\mathbf{c}^\star \tag{3.8}$$

Also the interplanar spacing d is given by,

$$\mid \mathbf{r}^\star_{hkl} \mid = \frac{1}{d_{hkl}} \tag{3.9}$$

The scattering vector is also represented as $\mathbf{q}$, related to $\mathbf{s}$ by

$$\mathbf{q} = 2\pi\mathbf{s} \tag{3.10}$$

3.1.3 Texture Analysis

Texture or crystallographic orientation refers to how the atomic planes in a volume of crystals are positioned relative to a fixed reference frame [47]. For the texture measurements, a sample is placed in a x-ray goniometer and the Bragg's angle 2θ is kept constant corresponding to a particular set of lattice planes (hkl). The sample is then rotated in the goniometer and whenever

there are crystallites which satisfies the Bragg's condition, a diffracted intensity is measured. The resulting diffracted intensity is plotted against the rotation angle to represent the texture. Figure 3.3 shows sample coordinates in real space and in reciprocal space. In the real space the sample is placed in the XY plane at position O (figure 3.3 a), the incoming beam and the detector is situated in the YZ plane. The scattering vector, $\mathbf{s}$, is directed along the Z'-axis in the reciprocal space (figure 3.3 b). For texture measurements the sample can rotate around X,Y and Z axis by an angle ω, ψ and ϕ, respectively, while keeping the Bragg's angle 2θ constant. For the ψ-scans, the sample is rotated around Y-axis in the XZ plane, in the real space (fig-
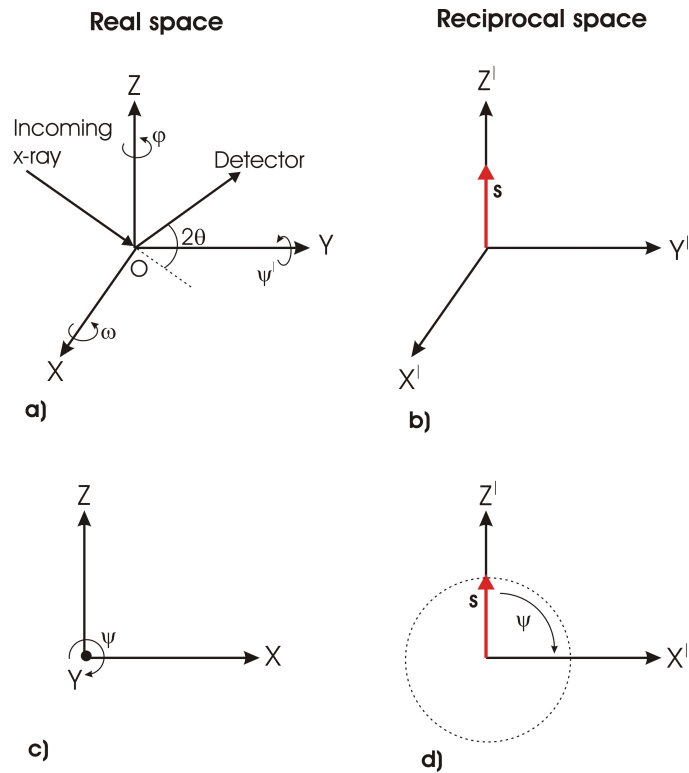
Figure 3.3: Texture measurement, a) the sample in real space, positioned at 'O' can be rotated around X, Y and Z axes by angle ω, ψ, ϕ and the Bragg angle, 2θ, is kept constant during the texture measurement. b) the scattering vector $\mathbf{s}$ in reciprocal space, corresponding to the Bragg angle 2θ, is directed along the Z'-axis. c) for ψ-scan, the sample is rotated around Y-axis by the angle ψ, in real space, d) in reciprocal space the scattering vector $\mathbf{s}$ rotates in $X'Z'$ plane by an angle ψ.
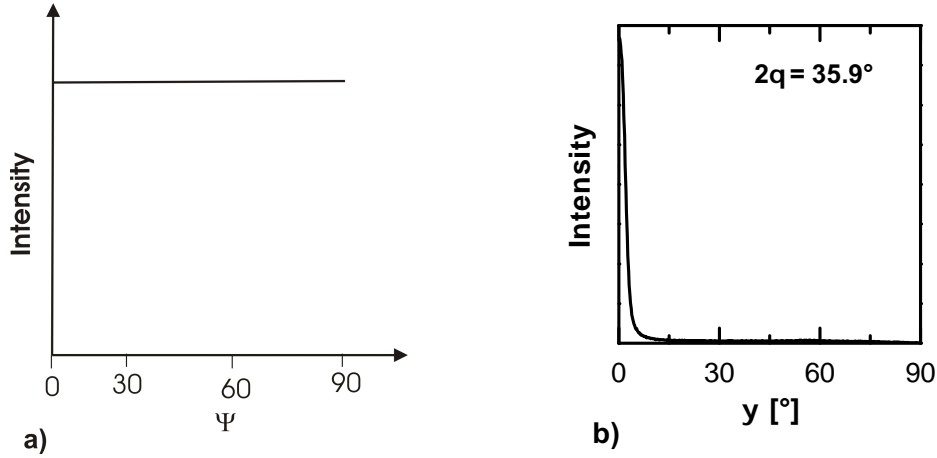
Figure 3.4: ψ-scans for a) an isotropic sample, the scattered intensity remains constant, schematic representation and b) highly oriented Tetracosane ($C_{24}H_{50}$) in 60 nm AAO nanopores

ure 3.3 c) and the scattering vector **s** then rotates in the $Z'X'$ plane in the reciprocal space (figure 3.3 d). Rotating the sample around Y-axis (for the ψ-scan) leads to non-coplanar geometry of the sample, that is the sample is no longer in the XY plane which causes defocusing effects which are discussed in details in chapter 4.

In the ψ-scan the intensity of the particular Bragg's reflection is measured as a function of angle ψ. For an isotropic sample the ψ-scan will show constant intensity, provided geometrical effects are neglected, as shown in the schematic representation in figure 3.4 a. ψ-scan for a highly oriented sample is shown in figure 3.4 b, the sample is tetracosane ($C_{24}H_{50}$) in 60 nm AAO nanopores. The ψ-scan corresponds to the (110) reflection at $2\theta = 36°$, the narrow width of the ψ-scan at 0° shows that the (110) planes are preferentially oriented parallel to the template surface. Figure 3.5 shows the x-ray diffraction set up used for measuring the texture of the P(VDF-TrFE) nanostructures in the AAO nanopores. The Bragg's angle θ and the tilt angle ψ is shown in the figure.

Only ψ-scans were used to study the orientation of the crystallites because we wanted to measure the orientation distribution of the crystallites with respect to the pore axis. The pore axis of the AAO nanopores is oriented along the Z-axis in figure 3.3 a. The ψ-scans corresponds to the rotation of the sample in the XZ plane which gives the orientation of the crystallites with respect to the pores axis. The crystal orientation in the sample plane is expected to be random therefore the ϕ-scan which measures the orientation of the crystals in the plane of the sample was not necessary.
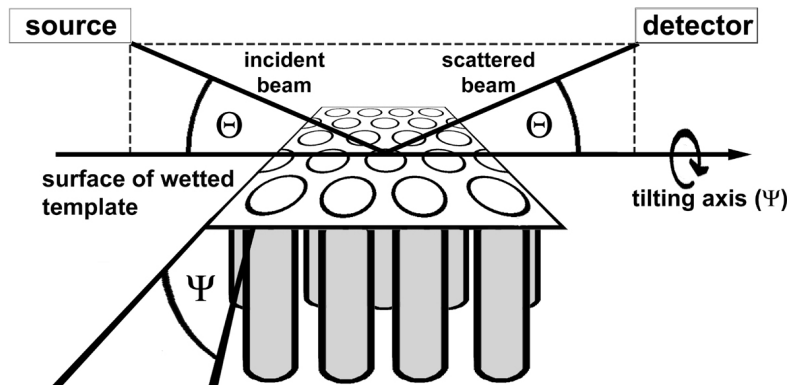
Figure 3.5: Schematic representation of x-ray scattering set-up. The alumina template was put in such a way that the surface is normal to the plane corresponding to the incoming and scattered x-ray beam. For ψ-scans the 2θ angle corresponding to certain lattice planes was kept constant and the sample was rotated around the ψ-axis.

3.2   Differential Scanning Calorimetry

Calorimetry means the measurement of heat [48]. There are many kind of calorimeters, most common for polymer characterization is the power compensation differential scanning calorimetry. DSC is very useful in determining thermodynamic parameters of the substances such as specific heat and its changes, enthalpy and entropy of phase transitions and the kinetic characteristics of processes. DSC is also main method to find crystallinity in the material. We have used power compensated Perkin Elmer DSC-7 to characterize the bulk P(VDF-TrFE) and the nanostructures.

The power compensation DSC consist of a measuring system having two microfurnaces, each containing a temperature controller and a heater, as shown in figure 3.6. Both microfurnaces are situated in aluminium blocks which are thermally decoupled. A control circuit supplies the same heating power to both the microfurnaces. In case of a ideal thermal symmetry, temperature of both the furnaces is the same. When a sample reaction occurs, the thermal symmetry is broken and temperature difference between the two furnaces occurs. This temperature difference is compensated by the temperature controller by increasing or decreasing the heat supply by an additional heating power ΔP to the sample furnace. The compensating heating power (ΔP) is proportional to the temperature difference ΔT between the sample and the empty pan. A heat flow rate ϕ_m is assigned to the ΔP [48].

During the DSC measurement, the absolute heat flow rate (ϕ_m) is di-
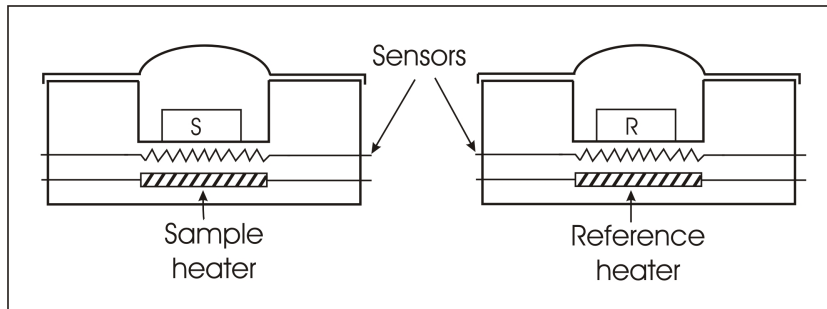
Figure 3.6: Power compensation DSC

vided by mass of the sample, the resulting heat flow is then plotted against temperature. Figure 3.7 shows the heat flow curves for the PVDF, which shows the melting and the crystallization peaks. This heat flow curve can be converted in specific heat (C_P) curve. To plot specific heat curve, first the temperature program for heat flow measurement is prepared such that before and after each heating and cooling step an isothermal step is added and applying this temperature program, the heat flow versus temperature measurement is obtained. In the next step the sample is removed from DSC and is replaced by an empty aluminium pan of approximately same weight as that of empty sample pan and with the same temperature program used for sample, heat flow is measured. To plot the specific heat curve, heat flow of empty aluminium pan is subtracted from the heat flow of the sample. The substraction of heat flow from empty aluminium pan is done for correction of heat flow from the aluminium pan which contain the sample. The heat flow is then divided by scan rate (Q) and mass (g) of the sample which

Figure 3.7: Heat flow curves of PVDF measured during heating and cooling by DSC

21

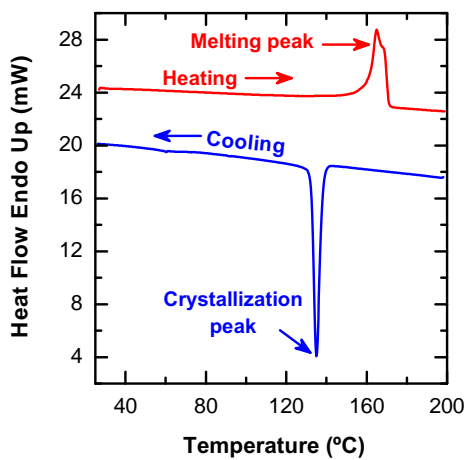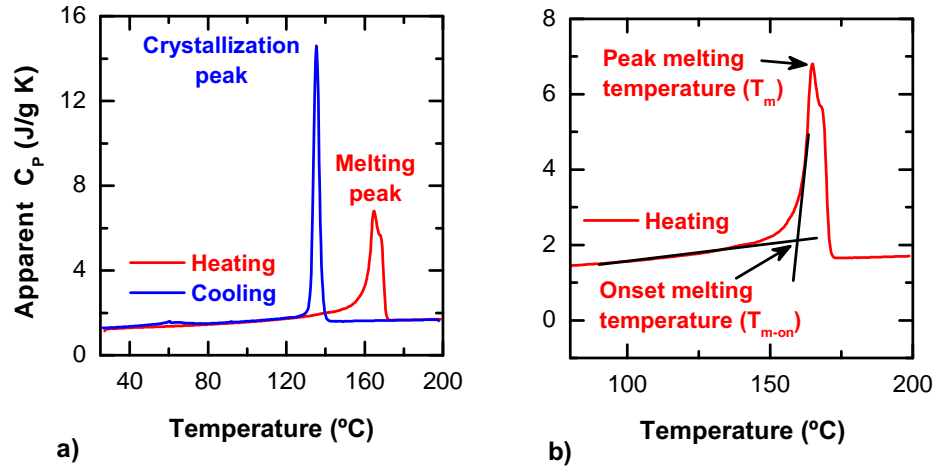Figure 3.8: Typical specific heat (C_p) curves for PVDF, a) heating and cooling scan and b) melting peak of DSC, onset melting temperature (T_{m-on}) and the peak melting temperature (T_m) is indicated

gives specific heat curve as shown in figure 3.8 *a* for PVDF. The melting temperature or crystallization temperature can be determined from the heat flow curve or the (C_P) curve. There are two ways to determine the melting or crystallization temperature from the respective peaks in the heat flow or (C_P) curves:

1. Peak melting/crystallization temperature: here the peak maxima for melting/crystallization is designated as the peak melting/crystallization temperature

2. Onset melting/crystallization temperature: the onset temperature is determined at the cross-section of two lines one plotted at the base of the peak and second line from a peak temperature tangent to the melting endotherm.

The onset melting temperature and peak melting temperature is shown in figure 3.8 *b* from the heating scan of PVDF.

Specific heat capacity (C_P) is the amount of heat per unit mass required to raise the temperature by one degree Kelvin, which can be calculated as follows. The heat flow rate is given by

$$\phi_m = \frac{q}{t} \tag{3.11}$$

$$Q = \frac{\triangle T}{t} \tag{3.12}$$

Then the C_P can be calculated as,

$$C_p = \frac{\phi_m}{Q \cdot m} \; [J/gK] \qquad (3.13)$$

where,

ϕ_m - heat flow rate [mW] or [mJ/s]

q - heat [J]

t - time [s]

$\triangle T$ - Change in temperature

Q - scan rate

C_p - specific heat capacity [J/g K]

m - mass of sample [g]

From the C_P curve, enthalpy of melting (H_m) and crystallization can be calculated. The area under the melting and crystallization peak gives melting and crystallization enthalpy of the material, respectively. The calculated enthalpy can be used to determine degree of crystallinity (D_C) of the sample if the enthalpy of the sample having 100% crystallinity is known.

3.3   Electron Microscope

3.3.1   Transmission Electron Microscope

The basic design of transmission electron microscope (TEM) is shown in figure 3.9. The electrons are generated at the cathode and are accelerated by the anode. The diverging electron beam is exactly focused on the sample by the condenser lens. The electron beam passing through the sample goes through the objective aperture to the objective lens and forms the single stage magnified image of the sample. In the plane of this intermediate image the selector aperture is located. The intermediate lens and projector lens successively enlarge the first intermediate image two more times. The three stage magnified image is visible on the fluorescent screen also the image can be captured by a digital camera connected to a computer. The image in the electron microscope is produced by scattering and diffraction of electrons by the sample [49]. Also the contrast in the image can come from the absorption of the electrons by the sample, path of the electrons in thicker region will
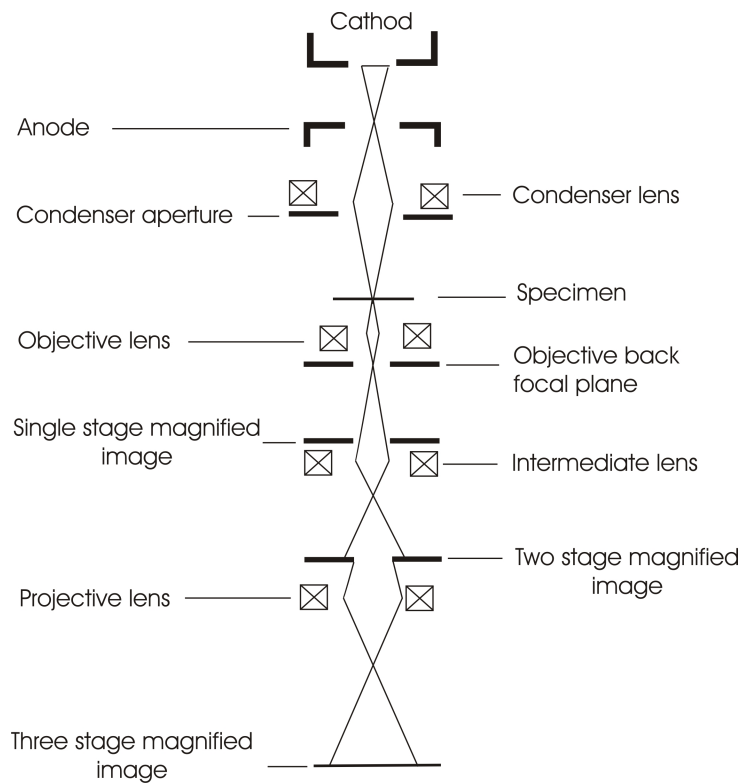
Figure 3.9: Schematic design of transmission electron microscope

be longer than the thinner section of the sample, the thinner section then will be brighter than the thick section of the sample. For analyzing the P(VDF-TrFE) nanostructure, JEOL 1010 electron microscope with 100 kV acceleration voltage was used.

3.3.2 Scanning Electron Microscope

Field emission scanning electron microscope (FESEM), JEOL-7500F was used for analyzing the P(VDF-TrFE) nanostructures. Acceleration voltage of 2 kV was used to determine the morphology with LEI (lower secondary electron image) detector.

Chapter 4

Texture Analysis in Reflection

Texture determination was explained in chapter 3.1 which can be carried out in a four axis diffractometer. This technique of texture determination was developed by Schulz [50]. The technique can be used in reflection or transmission mode. We have carried out the texture measurements, ψ-scans, in reflection mode which has some limitations. It was observed that during the ψ-scan, as the angle ψ is increased the diffracted intensity decreases even for an isotropic sample. Therefor the decrease in intensity is not related to the sample orientation but it is the geometrical effects that causes the decrease in the intensity. The effect was called defocusing effect. Various aspects of the defocusing effects were studied by different groups like the 2θ dependence, width of the opening of the detector and the absorption effects [47, 51–54]. In this chapter various aspects of the defocusing effects are considered and studied in order to gain understanding of the causes of defocusing. Finally some suggestions are made in order to improve the measurable ψ range.

A Phillips X'pert x-ray diffractometer was used for determining texture in the P(VDF-TrFE) nanostructures. To determine the limitations of ψ-scan, a systematic investigation was carried out on an isotropic cobalt oxide sample. The cobalt oxide sample was 10 mm $\times$ 10 mm in size with thickness of 500 μm. Figure 4.1 shows the $\theta - 2\theta$ scan and ψ-scan of the cobalt oxide (Co_2O_3) sample. In the ψ scan (figure 4.1 b), the intensity remains constant until 8° and then continuously fall with increasing the angle ψ. The angle at which the intensity starts to decrease is called critical angle ψ_c, as shown in figure 4.1 b. It is expected that for an isotropic sample the intensity should remain constant during the ψ-scan. But fall in intensity at ψ_c, in figure 4.1 b, shows that the defocusing effects can limit the measurable ψ range. This can be a serious limitation for the texture analysis because for an ideal ψ-scan it is expected that ψ_c is as close as possible to 90°. Therefore it is important to investigate the reasons behind the fall of intensity in the ψ-scan: a) it will
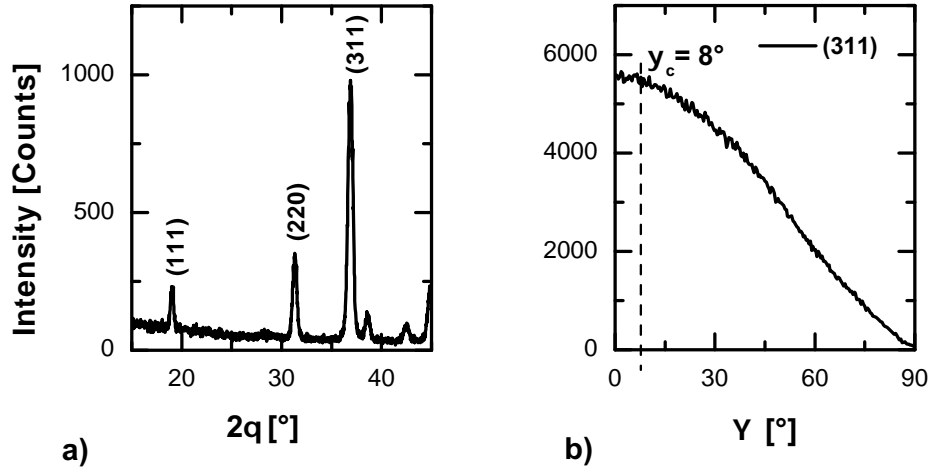
Figure 4.1: XRD pattern of cobalt oxide isotropic sample a) $\theta - 2\theta$ pattern and b) ψ-scan corresponding to (311) lattice planes at $2\theta = 36°$

provide a tool to improve the ψ_c and b) for more accurate analysis of the texture. In order to find the causes of the intensity decrease in the ψ-scan three main hypothesis were considered:

1. Increase in the angle ψ leads to increase in the illuminated area which, for a finite sample size, extend outside the sample surface at some critical angle ψ_c leading to reduction in the diffracted intensity.

2. Increase in ψ lead to increase in the scattering volume therefore there is an interplay between the scattered intensity and absorption of the x-rays depending on the material and the sample thickness

3. For a large sample surface, the finite detector viewing area can limit the ψ_c

The defocusing effects results from the non-planar geometry of the ψ-scan, that is during the ψ-scan half of the sample goes up and the other half goes down from the original sample plane. With the help of measurements on cobalt oxide sample, all these effects were considered and following conclusions were made:

1. The most important effect was found to be the limited sample area. The diffracted intensity reduces as the continuously increasing illuminated area spill out of the sample surface above a certain critical angle ψ_c. It was found out that by reducing the slit width of the incoming x-ray

26

beam, there is a considerable increase in the critical angle ψ_c. Also, for further experiments the sample size was increased.

2. For an isotropic sample, the diffracted intensity during the ψ-scan depend on the sample thickness. For a thin sample, $t \ll 1/\mu$, the diffracted intensity increases with increasing ψ, where t is thickness and μ is the linear absorption coefficient. On the other hand, for a thick sample, $t \gg 1/\mu$, the diffracted intensity is independent of the angle ψ.

3. In case of our instrument, the detector viewing area only plays a role for larger sample area therefore it is not a severe limitation

Understanding the diffractometer is essential to discuss the above mentioned effects therefore, first, the set-up of the diffractometer is described.

4.1   Set-up of the Diffractometer

Figure 4.2 shows the quasi-parallel geometry of the Phillips X'Pert diffractometer. The divergent x-rays are generated in the x-ray tube using a copper target. The x-ray beam is then directed onto the sample through a cross-slit. The standard opening for the cross-slit is 1 mm in height and 2 mm in width, both of these openings can be changed by adjusting two separate screws situated on the cross-slit. The incoming x-rays illuminates the sample with illuminated spot height h_θ and width w. On the detector side, the diffracted x-rays goes through a parallel plate collimator and a flat crystal graphite monochromator to the proportional detector.

4.1.1   Illuminated area on the sample

To understand the role of changing illuminated area during the ψ-scan we need to know the dimensions of the illuminated area on the sample during the x-ray diffraction measurements, taking into account the divergence of the x-ray beam. Figure 4.3 shows top view of the incident beam side of the x-ray diffractometer, the view shows x-ray beam on the sample at $\theta = 90°$. The x-rays are coming from the Cu target onto the sample through a slit opening of 1 mm in height, d, and 2 mm in width, c, these are the standard values for everyday measurements. In this section, the geometry of the set-up and the divergence of the x-rays is considered to calculate the illuminated area on the sample.
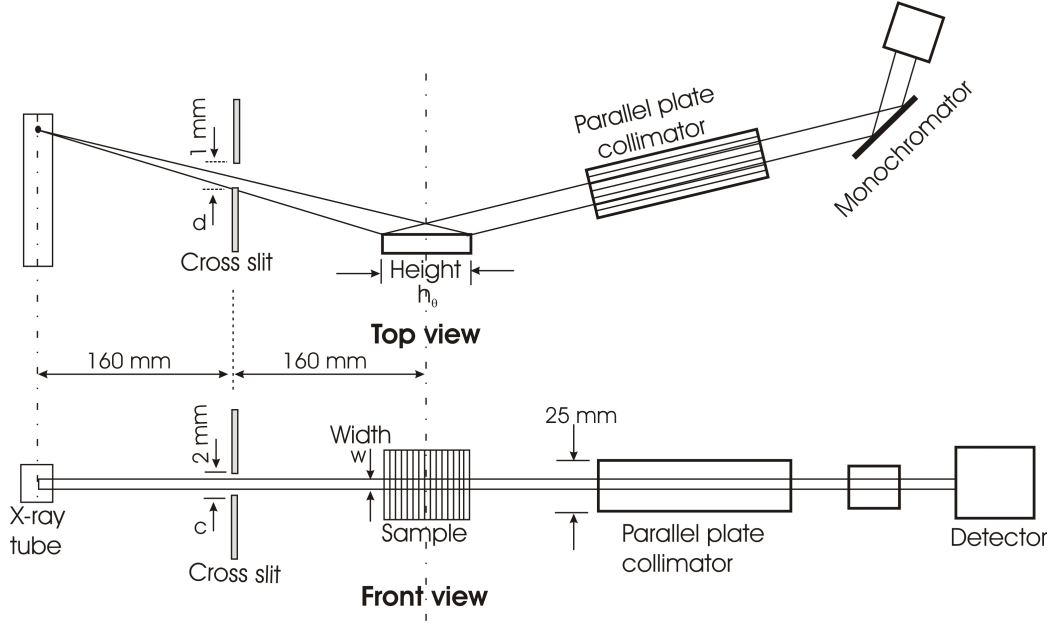
27

Figure 4.2: Geometric set up of Phillips X'pert four axis x-ray diffractometer

In the x-ray tube, the x-rays are generated by a point target of copper, the dimensions of the copper target are: length $e = 12\ mm$; breadth $a = 0.4\ mm$ and the take off angle is $6°$.

from figure 4.3, the length b of the copper target is,

$$b = e \times sin6° = 12 \times sin6° = 1.254\ mm \qquad (4.1)$$

b gives the length of the Cu target as seen from the sample surface.

The beam divergence, α, from a point source is given by d/Y_h, where Y_h is the distance between the point source and slit opening d [55]. In the figure 4.3, the values X_h, Y_h and P_h are unknown, the subscript h, stands for the values for calculation of the height of the illuminated beam. We will use another subscript w, to calculate width of the profile. In the figure 4.3, the divergent angles α_h and α_1 are shown. It is clear from the figure 4.3 that $\alpha_h = \alpha_1$. Also the point source is considered to be situated at O and we need to find Y_h to calculate α. With $Y_h = L - X_h$ and $X_h = L - Y_h$, the divergent angle is given by

$$\alpha_h = \frac{d}{Y_h} = \frac{d}{L - X_h} \qquad (4.2)$$

$$\alpha_1 = \frac{d}{X_h} = \frac{b}{L - Y_h} \qquad (4.3)$$
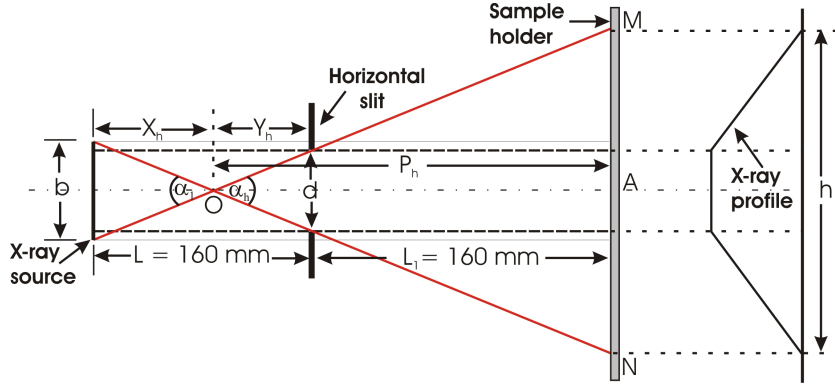
Figure 4.3: Incident beam side of the diffractometer, top view. The diverging x-rays are coming onto the sample at $\theta = 90°$. Subscript h is indicated for dimensions used for the calculation of *height* for the illuminated beam. Similarly subscript w can be used to calculated the width of the illuminated beam.

From the relation $\alpha = \alpha_1$ and solving for Y_h, we have

$$Y_h = \frac{Ld}{b+d} \tag{4.4}$$

Where L is the distance between the Cu target and slit opening, d, with the Cu target length, b. Putting the value of Y_h in equation 4.2, we have divergent angle for height

$$\alpha_h = \frac{b+d}{L} \tag{4.5}$$

similarly the divergent angle for width is

$$\alpha_w = \frac{a+c}{L} \tag{4.6}$$

The divergent angle α is calculated from point O in the figure 4.3. The distance between the sample and point O is

$$P_h = L_1 + Y_h \tag{4.7}$$

Putting the value of Y from equation 4.4 and simplifying, we have for height

$$P_h = \frac{L_1 b + L_1 d + Ld}{b+d} \tag{4.8}$$

29

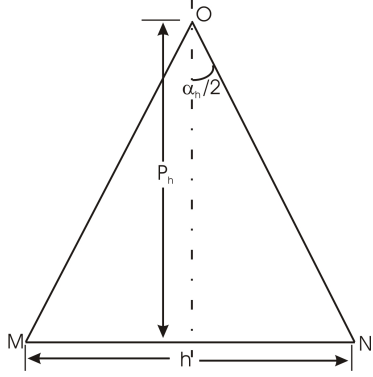Figure 4.4: Shows the triangle MON from the figure 4.3 with h as the height of the illuminated profile

Similarly for width,

$$P_w = \frac{L_1a + L_1c + Lc}{a + c} \qquad (4.9)$$

From the figure 4.4, the illuminated height h, on the sample at $\theta = 90°$ is

$$
\begin{aligned}
tan(\alpha_h/2) &= \frac{h/2}{P_h} \\
h &= \frac{P_h tan(\alpha_h/2)}{2} \qquad (4.10)
\end{aligned}
$$

putting the value of P_h from equation 4.8 in above equation, we have for illuminated height

$$h = \frac{(L_1b + L_1d + Ld)tan(\alpha_h/2)}{2(b + d)} \qquad (4.11)$$

where, L_1 is the distance between slit opening and the sample, b is the length of copper target, d is the slit opening for height and α_h is the divergent angle for the height. Similarly the illuminated width can be calculated,

$$w = \frac{P_w tan(\alpha_w/2)}{2} \qquad (4.12)$$

putting the value of P_w from equation 4.9 in above equation, the illuminated width can be give by

$$w = \frac{(L_1a + L_1c + Lc)tan(\alpha_h/2)}{2(a + c)} \qquad (4.13)$$

where, α_w is the divergent angle for the width, a is the width of the copper target and c is the slit opening for the width. Table 4.1 shows the illuminated height and width calculated from the equation 4.11 and equation 4.13,

30

	Slit opening	Illumination on sample
height	d = 1 mm	h = 3.25 mm
width	c = 2 mm	w = 4.4 mm

Table 4.1: Opening of the x-ray slit and the dimensions of the illuminated area on the sample at $\theta = 90°$, due to diverging x-rays

respectively. The parameters were used from the standard geometry of the diffractometer. With copper target length of $b = 1.254\ mm$ and width of $a = 0.4\ mm$. The dimensions are calculated for $\theta = 90°$, with change in θ the change in illuminated height is given as $h_\theta = h/sin\theta$.

4.2 Limitations in Texture Determination

As discussed earlier, the critical angle, ψ_c, is limited by the defocusing effects. In this section the effects of finite sample size, absorption and detector limitations are discussed in relation with the ψ_c.

4.2.1 Limitations Due to Finite Sample Size

During the ψ-scan when the angle ψ is increased, the size of the illuminated spot changes and at some angle ψ_c the illumination spills over the sample surface and the detected intensity starts reducing with increasing the angle ψ. Here, the defocusing effect is considered for a finite size of the sample and the critical angle ψ_c is calculated. The theoretical results are finally compared with the experimental results.

Figure 4.5 shows the illuminated area on a finite sample surface with increasing angle ψ. As the angle ψ increases, the illuminated area increases beyond the sample size which leads to the loss in diffracted intensity. In order to calculate the critical angle, ψ_c, where the intensity drop is maximum, we need to calculate the area of the illumination as a function of ψ. This area of illumination then can be separated in two parts, first the area which remain on the sample and second area which spills over the sample. Diffracted intensity will come only from the illuminated area on the sample. The calculations are applied to the cobalt oxide sample with the dimensions of the illuminated spot taken from section 4.1.1.

Figure 4.5 a shows the width, e, and breadth, f, of the sample while w and h_θ are width and height of the illuminated area at $\psi = 0°$. Here, the illuminated area is considered at $2\theta = 36.8°$ where the ψ-scan for the
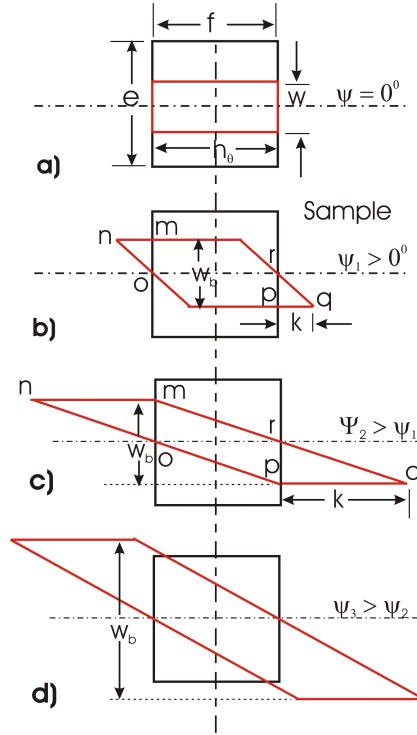
Figure 4.5: Schematic representation of change in illuminated area with increasing ψ angle on the sample surface (black: sample and red: illuminated area)

cobalt oxide sample is measured. During the ψ-scan the illuminated width increases, the increasing width, w_b, can be given by

$$w_b = \frac{w}{cos\psi} \tag{4.14}$$

Due to the increase in the width, the illuminated area increases and some part of the illuminated area spills over the sample area, the area which spills out is $\triangle mno$ and $\triangle pqr$, shown in figure 4.5 b, c. The area of the triangles can give us how much of the illumination is lost during the ψ-scan.

Area of the $\triangle pqr$ is,

$$A(\triangle pqr) = \frac{1}{2} \times k \times \frac{1}{2} \times \frac{w}{cos\psi} \tag{4.15}$$

The k is a unknown in this equation. It can calculated by considering the vertical displacement of the sample during the ψ-scan. Figure 4.6 shows the illuminated area on the sample at $\psi = 0°$ (solid line). By rotating the
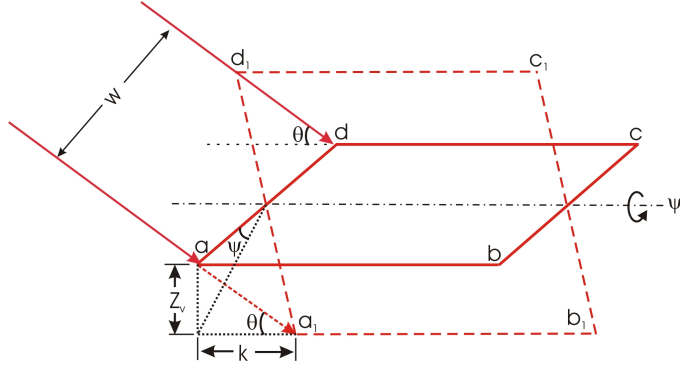
Figure 4.6: Schematic representation of change in illuminated area with increasing ψ angle (solid line: illuminated area at $\psi = 0°$ and dashed line: illuminated area at $\psi > 0°$)

sample by an angle ψ around the ψ-axis , the change in illuminated area is shown by the dashed line. For clarity, the sample is not shown in the figure. Due to the rotation of the sample by an angle ψ, the illuminated edge has moved down from its original position by a distance Z_v, as shown in figure 4.6. The vertical distance as a function of ψ can be given by

$$tan\psi = \frac{Z_v}{w/2}$$

$$Z_v = \frac{wtan\psi}{2} \tag{4.16}$$

This vertical displacement causes distortion of the illuminated area. During the ψ-scan, one edge of the illuminated height moves backward and the other moves forward due to the upward and downward movement of the sample, respectively. We can calculate the forward movement of k, from the figure 4.6

$$k = \frac{Z_v}{tan\theta} \tag{4.17}$$

putting the value of Z_v from equation 4.16, we have

$$k = \frac{wtan\psi}{2tan\theta} \tag{4.18}$$

putting the value of k from the equation 4.18 in the equation 4.15, we have

$$A(\triangle pqr) = \frac{1}{4} \times \frac{wtan\psi}{2tan\theta} \times \frac{w}{cos\psi} \tag{4.19}$$

33

Area outside the sample surface is the sum of the triangles $\triangle mno$ and $\triangle pqr$, therefore loss of illuminated area from the sample is

$$A_T = 2 \times \frac{1}{4} \times \frac{wtan\psi}{2tan\theta} \times \frac{w}{cos\psi}$$

$$A_T = \frac{1}{4} \cdot \frac{w^2 tan\psi}{tan\theta \cdot cos\psi} \tag{4.20}$$

The above equation is valid only until the $\triangle mno$ and $\triangle pqr$ are triangular. They are triangular only up to an angle ψ_h when the moving front $k \leq h$, further increase in k with angle ψ leads to a non-triangular area, figure 4.5 d. For simplicity, the calculations are limited to the angle ψ_h. Let at ψ_h,

$$k = h_\theta \tag{4.21}$$

where $h_\theta = h/sin\theta$ is the height of illuminated beam at an angle θ.

$$\frac{wtan\psi_h}{2tan\theta} = h_\theta$$

$$\psi_h = tan^{-1}\left(\frac{2h_\theta tan\theta}{w}\right) \tag{4.22}$$

The above equation gives the limitations for the calculations for loss of illumination on the sample, A_T, due to the spill-over effect. Considering the illuminate height 3.25 mm, calculated in section 4.1.1 and for $2\theta = 36.72$, the peak in the x-ray pattern for cobalt oxide, the ψ_h for the illuminated width of 4.4 mm and 1.4 mm is 57° and 78°, respectively.

The equation 4.20 is also limited for a width, w_b equal to the sample width, e, at certain angle ψ_w. For $w_b = e$ and from equation 4.14, we have

$$\frac{w}{cos\psi_w} = e$$

$$\psi_w = cos^{-1}\left(\frac{w}{e}\right) \tag{4.23}$$

Beyond the angle ψ_w we have to consider the illuminated spot width going outside the width of the sample. For this reason the calculations are limited up to ψ_w. For sample width, e, of 10 mm and illuminated width of 4.4 mm and 1.4 mm, ψ_w is 64° and 82°, respectively. Therefore, decreasing the width of illumination spot or increasing the sample size will reduce the spill over of the illumination in the width direction.

The equation 4.20 shows the spill over of illumination from the sample. It also shows that reducing the illumination spot width, w, and increasing θ can

	Slit opening	Illumination on sample
height	d = 1 mm	h = 3.25 mm
width	c = 0.5 mm	w = 1.4 mm

Table 4.2: Opening of the x-ray slit and the dimensions of the illuminated area on the sample at $\theta = 90°$, due to diverging x-rays.

reduce the spill over effect. Therefore, the default vale of the slit opening, c, was reduced from 2 mm to 0.5 mm for further analysis. This results in reduced width of illumination on the sample which is given in table 4.2, calculated by equation 4.13. The calculations were limited up to the limiting angle ψ_h which for $w = 1.4\,mm$ is 82°.

To study the ψ dependence of the illuminated area on the sample, first the area of the parallelogram, in figure 4.5 indicated by red line, is calculated. The area of the parallelogram is

$$A_p = \frac{w}{cos\psi} \times h_\theta \tag{4.24}$$

where, h_θ is the illumination height at the scattering angle θ. The fraction of the beam on the sample, after the loss of illumination due to spill over effect, can be calculated as,

$$B_f = \frac{A_p - A_T}{A_p} \tag{4.25}$$

where, A_T is the illuminated area lost due to spill-over effect, given by equation 4.20. The fraction of the beam on the sample (B_f) against the angle ψ is plotted in the figure 4.7 for the illuminated width of 4.4 mm and 1.4 mm. The plots are limited to the angle ψ_h, given by equation 4.22.

Comparison with fraction of the beam on the sample surface, B_f, in figure 4.7 and the actual ψ-scan shown in figure 4.8 show the common trend that the loss in the illuminated beam on the sample surface is also leading to decrease in intensity in the ψ-scans. There is considerable improvement when w is decreased, the fraction of the beam on the sample remains high for larger ψ angles, as shown in figure 4.7 b and there is also actual improvement in the ψ-scan, figure 4.8 b. Qualitatively B_f and reduction in intensity in the ψ-scan show the same ψ dependence. But there are some differences, the decrease in the B_f is rapid, in case of $w = 4.4\,mm$ in figure 4.7 a, than the actual ψ-scan in the figure 4.8 a.

These differences could arise from some assumptions made for the calculations which may underestimate or overestimate the illumination on the
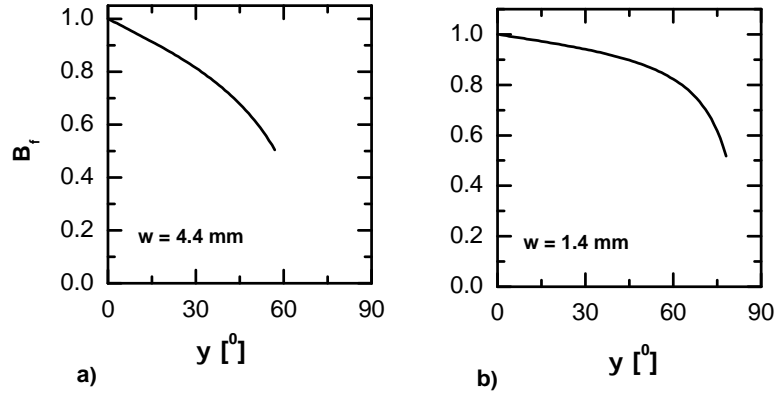
Figure 4.7: Fraction of the illuminated beam on the sample with increasing ψ angle; a) for illuminated width of 4.4 mm and b) for illuminated width of 1.4 mm
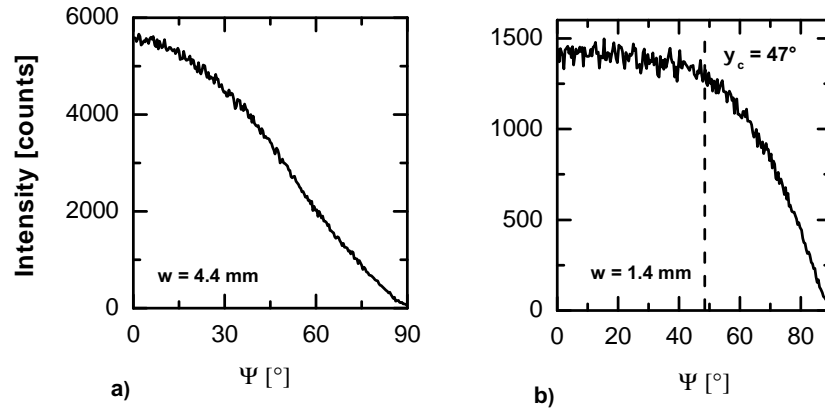

Figure 4.8: ψ-scan of Co_2O_3 isotropic sample at $2\theta = 36.8°$, a) for illuminated width of 4.4 mm and b) for illuminated width of 1.4 mm

sample surface. The main assumption is that the sample is illuminated with uniform flux with a rectangular illuminated spot, which is not the case, the intensity distribution of the illumination has a trapezoidal shape. Which means that the central area inside the illuminated spot has the maximum flux than at the edges. Considering the fact that the calculations were done for the uniform flux, the differences are not surprising.

There is a vast improvement for containing the loss of illumination when the width, w, of the illuminated spot is reduced from 4.4 mm to 1.4 mm. This marked improvement is due to the dominant role played by the quadratic

term w in the equation 4.20. Reducing w decreases the spill-over of the illuminated beam from the sample and the loss in intensity during the ψ-scan is minimized. Simultaneously increasing the sample dimensions could lead to increase in the ψ_c.

4.2.2 Absorption of X-Rays During the ψ-scan

During the ψ-scan, the illuminated area on the sample increases, which should result in the increase in the diffracted intensity. The increase in the diffracted intensity during the ψ-scan was not observed. It was found that the diffracted intensity is dependent on the absorption coefficient, μ, and the sample thickness, t, during the ψ-scan. Effects of absorption coefficient and sample thickness on ψ-scans are discussed in this section. First we look at how the illuminated area on the cobalt oxide sample is increasing with ψ. As shown in figure 4.5, the illuminated area on the sample can be calculated by subtracting the area of the triangles which spill over the sample surface from the total area of the illuminated spot, given by

$$
\begin{aligned}
A_I &= \frac{w}{cos\psi} \times h_\theta - \frac{1}{4}\frac{w^2 tan\psi}{tan\theta cos\psi} \\
A_I &= \frac{w}{cos\psi}\left(h_\theta - \frac{1}{4}\frac{w tan\psi}{tan\theta}\right)
\end{aligned}
\tag{4.26}
$$

As in the last section A_I was calculated for cobalt oxide sample and at $2\theta = 36.78°$, the illuminated spot width, $w = 1.4$ mm, and $h_\theta = 10.3\,mm$. Using the equation 4.26, the illuminated area on the sample (A_I) is plotted against ψ in the figure 4.9, it shows that with increasing ψ the illuminated area on the sample increases. But the ψ-scan measurements on cobalt oxide
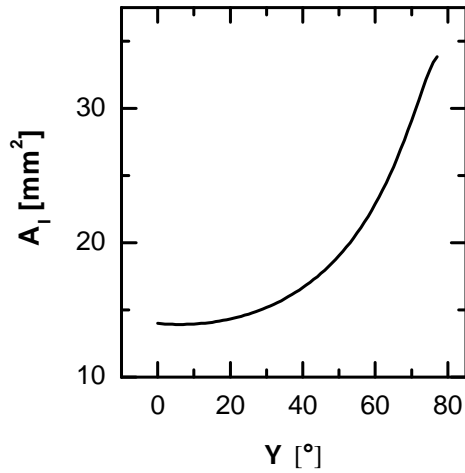

Figure 4.9: Change in illuminated area on cobalt oxide sample with the angle ψ

37

sample, for same geometry, as shown in figure 4.8 b, does not show any increase in diffracted intensity. Therefore it is possible that absorption of the x-rays by the sample must have played a role.

During the transit of the x-rays through a sample the intensity is attenuated due to absorption of the x-rays by the matter, the attenuated intensity I, is give by the following equation,

$$I = I_0 e^{-\mu l} \tag{4.27}$$

where, I_0 is the initial flux of the x-rays, μ is the linear absorption coefficient and l is the path length of the x-ray through the sample [55].

During the ψ-scan, in reflection, the path x-rays have to travel through the sample is shown in figure 4.10. The path length is given by

$$l = \frac{x}{sin\theta \cdot cos\psi} \tag{4.28}$$

Let us consider a layer thickness, dx, inside the sample then the irradiated volume is

$$dv = \frac{A \cdot dx}{sin\theta \cdot cos\psi} \tag{4.29}$$

If i(2θ) is the intensity of scattering per unit volume of the sample then the contribution to the total scattering intensity in reflection by the layer dx at the depth x is,

$$dI = i(2\theta)\frac{Adx}{sin\theta cos\psi}exp\left(-2\mu\frac{x}{sin\theta cos\psi}\right) \tag{4.30}$$

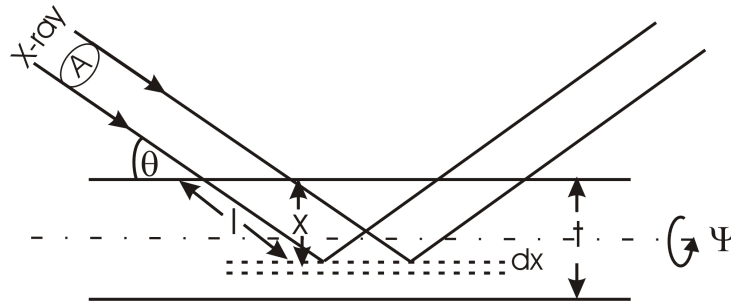Integrating the above equation with respect to x from 0 to t,

Figure 4.10: Path length (l) of the x-rays through the sample during the $\theta - 2\theta$ and ψ-scan measurement in reflection mode

$$I = i(2\theta)\frac{A}{2\mu}\left[1 - exp\left(-2\mu\frac{t}{sin\theta cos\psi}\right)\right] \qquad (4.31)$$

where, t is the thickness of the sample. For thick sample $t \rightarrow \infty$ or $\mu t \gg 1$, the above equation becomes,

$$I_\infty = i(2\theta)\frac{A}{2\mu} \qquad (4.32)$$

where I_∞ is the diffracted intensity for infinitely thick sample. The above equation shows that for the thick samples the diffracted intensity is independent of the angle ψ during the ψ-scan.

For the thin samples with $\mu t \ll 1$, the equation 4.31 can be rewritten as

$$
\begin{aligned}
I &= i(2\theta)\frac{A}{2\mu}\left[1 - \left(1 - \frac{2\mu t}{sin\theta cos\psi}\right)\right] \\
I &= i(2\theta)\cdot\frac{At}{sin\theta cos\psi}
\end{aligned}
\qquad (4.33)
$$

Equation 4.33 shows that for thin samples ($t \ll 1/\mu$), the diffracted intensity increases with increase in the angle ψ during the ψ-scan.

It is clear from the equations 4.32 and 4.33, that the diffracted intensity during the ψ-scan will change depending on the sample thickness. To differentiate between the thick and thin samples and the role it plays during the ψ-scans of cobalt oxide and P(VDF-TrFE) embedded in alumina, we need to know the linear absorption coefficient μ of each sample. The linear absorption coefficient is calculated by,

$$\mu = \rho\sum_j(\frac{\mu}{\rho})_j w_j \qquad (4.34)$$

where ρ is the overall density of the sample and $((\mu/\rho)_j)$ and w_j are the mass absorption coefficients and weight fractions of the jth atomic component in the sample [55].

The cobalt oxide which was in powder form was mixed with wax to use it for the XRD measurements. The sample was 500 μm thick. The density of cobalt oxide is 6.11 g/cm^3 (from the supplier) and density of wax is 0.93 g/cm^3, the mass absorption coefficients were obtained from reference [55]. Considering 1:1 proportion for cobalt oxide and wax the linear absorption coefficient, μ, was found out to be 717.13 cm^{-1}. Also, the absorption length, $1/\mu = 13.9\mu$m, which is negligibly small compared to the sample thickness of 500 μm and from equation 4.32 we can say that the absorption will exactly

balance the increasing scattering volume during the ψ-scan for cobalt oxide - wax sample.

In similar way the linear absorption coefficient for alumina (Al_2O_3) was found to be 102.9 cm^{-1} considering the density of the alumina as 3.25 g/cm^3 [56]. Which gives $1/\mu = 97\mu$m, which is less than the sample thickness of 100 μm. The absorption length and the sample thickness is similar which will have negligible effect on the diffracted intensity during the ψ-scan.

4.2.3   Detector Limit

If we consider an infinitely large sample, for which the limitation considered in *section 4.2.1* is no longer valid, then at larger ψ angles the detector has to receive diffraction from a large illuminated area. The detector opening can restrict the incoming diffracted x-rays to the detector reducing the critical angle ψ_c.

Figure 4.11 shows the change in illuminated area on an infinitely large sample with increasing the angle ψ, also shown is the detector area where the detector can see the illuminated area. The critical ψ_c, in the figure 4.11 c, is reached when the illuminated width is exactly equals to the detector height d_d and there will be loss in intensity if we consider that the incoming flux is now being distributed over a larger area which is invisible to the detector. To find the detector area from which the detector can accept the diffracted rays for an infinitely large sample, the sample position was changed vertically to simulate the effect similar to the ψ-scan. As shown in figure 4.12 the sample is put at a mean position with X, Y and Z co-ordinates at zero and the sample was moved in such a way that the sample remains always illuminated by the x-rays. Changing the Z position then lead to some critical value Z_c where the sample edge touches the detector edge, changing the Z value beyond will then lead to reduction in intensity because then the detector can not see some part of the sample.

To calculated the detector opening, we know that illuminated height, h, on the sample is $h_\theta = h/sin\theta$. Similarly for the detector opening d_d the detector height on the sample at an angle θ will be $h_d = d_d/sin\theta$.

Also in the figure 4.12 the $\triangle abc$ is a isosceles triangle with e as the mid point of ab. The $l(ae)$, designated as X, is given by,

$$X = \frac{1}{2}(\frac{h_d}{2} - \frac{h_\theta}{2}) = \frac{1}{4}(\frac{d_d}{sin\theta} - \frac{h}{sin\theta})$$
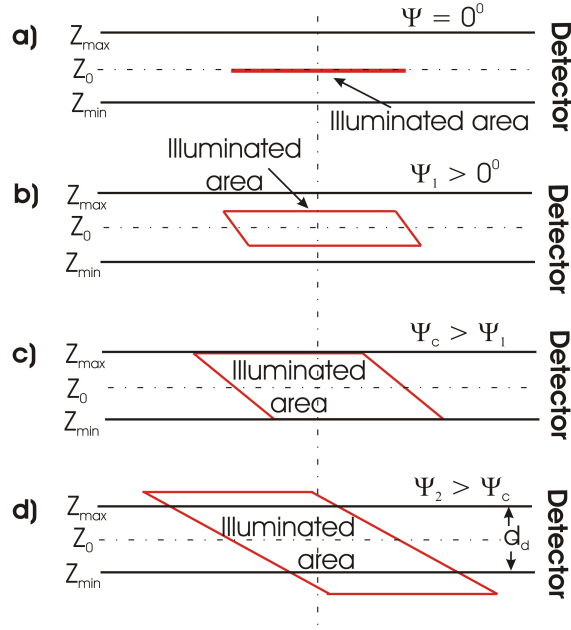$$X = \frac{d_d - d_\theta}{4sin\theta} \tag{4.35}$$

Figure 4.11: schematic representation showing the detector width and the illuminated area (red color) which increases with increasing the ψ angle

The vertical distance Z_c beyond which detector can not detect the diffracted intensity is

$$tan\theta = \frac{Z_c}{X}$$

from the equation 4.35, we can write

$$Z_c = Xtan\theta = \frac{d_d - h}{4sin\theta}tan\theta$$
$$Z_c = \frac{d_d - h}{4cos\theta}$$

$$(4.36)$$

where, Z_c gives the vertical limit of the detector, further solving the equation 4.36 for detector opening, we have

$$d_d = 4Z_ccos\theta + h \qquad (4.37)$$

We can calculate the detector opening from equation 4.37 if we know the critical height Z_c. To calculate Z_c, the sample was moved along the
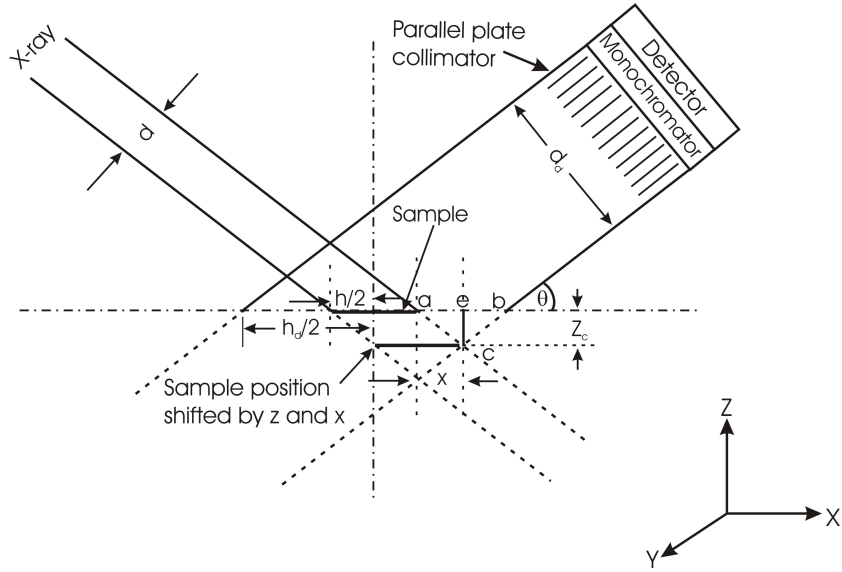
Figure 4.12: Incoming x-ray beam area and the detector area on the sample plane. The sample position is changed in X and Z direction so that the sample remains in the x-ray beam.

negative Z-axis with 0.2 mm step with simultaneous movement along the X-axis by $X = Z/tan\theta$. At each step of Z XRD pattern for Co_2O_3 sample was measured for 2θ angles between $35°$ to $38°$. The 2θ measurements on Co_2O_3 isotropic sample is shown in figure 4.13 a, for clarity, the 2θ patterns are only shown for change in Z by a step of 0.4 mm. The peak 2θ intensity is plotted against Z in figure 4.13 b. There is a linear decrease in intensity from $Z = 2$, this is the critical value Z_c which shows the detector limit. Putting the values of Z_c, $h = 3.25$ and $2\theta = 36.8°$ in equation 4.37, we have the detector opening, $d_d = 10.83$ mm. Also, we can see in the XRD patterns in figure 4.13 a that the peak 2θ position is changing with vertical shift in sample position, Z. This is what actually happen in ψ-scan, a non-planar geometry, as the angle ψ increases the sample sides are shifted from its mean position in both positive and negative Z direction, which causes the increase in the peak width.

To validate that above calculations are correct another method was used to calculate the detector opening based on the specifications of the instruments in the XRD manual [57]. The specifications are shown in figure 4.14. The scattered x-rays from the sample goes to the detector through a parallel plate collimator and a graphite monochromator. The monochromator is aligned at 2θ angle of $26.6°$ with the detector and the parallel plate collima-
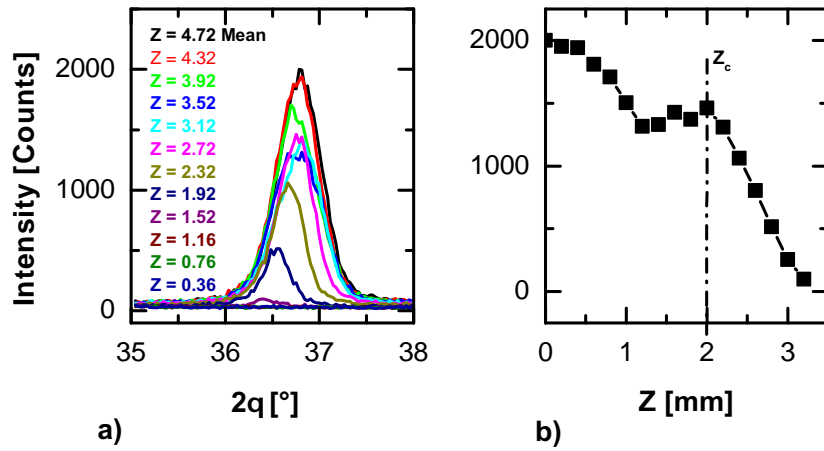
Figure 4.13: a) $\theta - 2\theta$ measurements of the cobalt oxide sample, for each 2θ pattern the sample position was changed in Z direction and b) the peak for each 2θ scan is plotted against Z

tor. Considering the detector opening and the parallel plate collimator opening, it is the monochromator which limits the size of the incoming diffracted beam from the parallel plate collimator. In the figure 4.14, d_p is opening of the parallel plate collimator from which the monochromator can accept the diffracted rays. Considering the height of the monochromator, m_h, of 50 mm and angle of $\theta = 13.3°$, opening of the parallel plate collimator from which
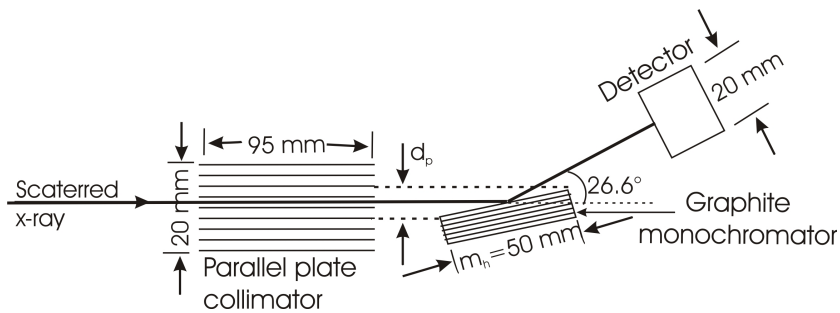

Figure 4.14: X-ray diffractometer optics. Path of x-rays from sample surface to the detector

43

the monochromator can receive the diffracted x-rays is

$$
\begin{aligned}
d_p &= m_h \cdot sin\theta \\
&= 50 \cdot sin13.3 \\
d_p &= 11.50\,mm
\end{aligned}
\tag{4.38}
$$

We have the detector opening values from two different methods:

- Detector opening from changing the sample position = 10.83 mm

- Detector opening from the specifications of the instrument = 11.50 mm

Both the values are very close and we can take a suitable value of 11 mm for detector opening. We further need to know the change in illuminated area with ψ in order to calculate ψ_c.

At critical angle ψ_c, the vertical displacement of the sample during the ψ-scan given by equation 4.16 which will be equal to critical height Z_c. Then we have

$$
\begin{aligned}
Z_v &= Z_c \\
\frac{wtan\psi_c}{2} &= \frac{d_d - d}{4cos\theta} \\
\psi_c &= tan^{-1}(\frac{d_d - d}{2wcos\theta})
\end{aligned}
\tag{4.39}
$$

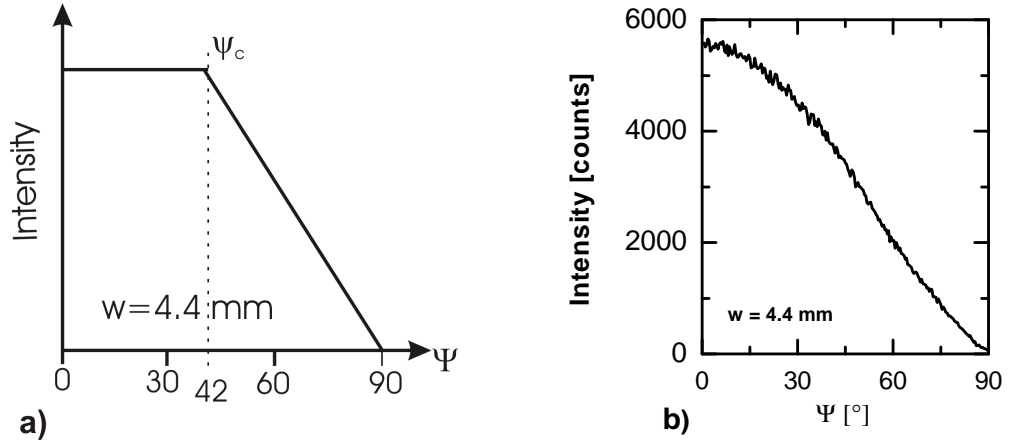Figure 4.15: Critical angle ψ_c from which drop in intensity starts during the ψ-scan for $w = 4.4\,mm$, a) calculated from the detector limit and b) actual ψ-scan on isotropic Co_3O_4 sample

44

With the parameters $2\theta = 36.4°$ with detector opening, $d_d = 11\,mm$, illuminated height, $h = 3.25\,mm$ and width of illumination, $w = 4.4\,mm$, the ψ_c can be calculated by equation 4.39 is 43°. As shown in figure 4.15, we can see that the intensity in the actual ψ-scan decreases much earlier than the calculated value of 43°. Therefore it is clear that the detector limit does not play a major role in limiting the ψ_c.

4.3   Summary

It is shown that the most important effect causing the decrease in intensity due to defocusing effect at an angle ψ_c, in the ψ-scans, was due to finite sample size. During the ψ-scan, the increasing illuminated area spread beyond the sample area and the x-ray flux spills over the sample surface. This causes the reduction in the diffracted intensity. The increase in the diffraction volume during the ψ-scan is exactly balanced by the absorption of the x-rays for the samples we have used. Limited detector viewing area only plays a role, limiting the critical angle ψ_c, when the sample size is large enough that the illuminated spot does not spill over it.

From the ψ-scan analysis of the isotropic sample we have to consider the following points to increase the ψ_c

- Reduce the illuminated width so that there is a optimum balance between the ψ_c and intensity: the slit width of the incoming x-rays was reduced from 2 mm to 0.5 mm to increase the ψ_c. The reduced width was used for all the ψ-scan measurements shown in chapter 7.

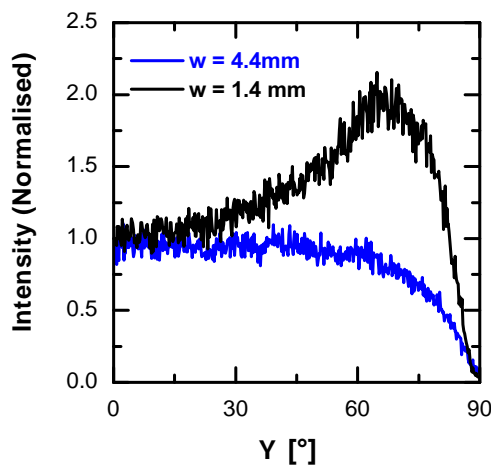- Use larger sample size: for all the measurements the sample size was

Figure 4.16: ψ-scans of 60 nm P(VDF-TrFE) nanostructures at $2\theta = 40.8°$ with illuminated width,w, of 4.4 mm and 1.4 mm

increased from $1\,cm \times 1\,cm$ to $1.5\,cm \times 1.5\,cm$ to reduce the effect of limited sample size

Objective of studying the limitation of ψ-scans were to determine the causes of the limitations, to make the necessary corrections and to apply the knowledge for texture measurements of P(VDF-TrFE) nanostructures. Figure 4.16 shows the ψ-scans of P(VDF-TrFE) 60 nm nanostructures measured at $2\theta = 40.8°$ with illuminated width, w, of 4.4 mm and 1.4 mm. The intensity for both the scans are normalized to 1 at $\psi = 0°$. For the larger w, the ψ-scan does not show any peak but reducing the slit width, the peak at $60°$ is clearly visible, for the same sample. This example shows that the increase in the ψ_c in the ψ-scan is essential for texture determination of the P(VDF-TrFE) nanostructures and therefore understanding the limitations and making corresponding changes in the set-up was important. The ψ-scans for P(VDF-TrFE) are discussed in chapter 7 to determine the orientation of the P(VDF-TrFE) crystallites in the nanostructures.

Chapter 5

P(VDF-TrFE) Nanostructures Templated in Nanoporous Alumina

5.1 Wetting of Ordered Nanoporous Alumina

The first step towards preparation of polymer nanostructures using anodic aluminium oxide (AAO) template is *wetting* of the template by polymer. The wetting mechanism determines the morphology of the nanostructures prepared by the AAO template. There are some studies of wetting of the AAO template by polymers [58–60]. But due to complex nature of the subject, wetting of porous alumina by polymers is not yet fully understood [21]. To understand the morphology of the P(VDF-TrFE) nanostructures we need to understand the wetting mechanism of porous alumina by P(VDF-TrFE). We start with a simple case of wetting of flat surfaces by liquids in order to gain understanding of the wetting mechanism in simple liquids and then this knowledge could be applied to the wetting of the AAO template by P(VDF-TrFE).

5.1.1 Wetting on Flat Substrates

Wetting refers to the study of how a liquid deposited on a solid (or liquid) substrate spreads out [62]. A liquid drop on a solid surface is shown in figure 5.1. Three different surface tensions are present in the system. The relationship between the interfacial surface tensions of solid-liquid (γ_{sl}), solid-vapor (γ_{sv}), liquid-vapor (γ_{lv}) and the equilibrium contact angle, θ_e, is given
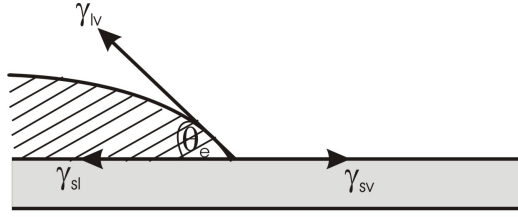
Figure 5.1: Force balance in three-phase contact line [61]

by Young's equation

$$\gamma_{sv} = \gamma_{sl} + \gamma_{lv}cos\theta_e \qquad (5.1)$$

The easily measurable quantities in Young's equation are γ_{lv} and θ. The γ_{sv} and γ_{sl} are difficult to measure directly and additional relations are required to calculate them. Apart from other approaches one of the approach close to the experimental values is based on Berthelot's rule, which states that the potential energy parameter of unlike pair interactions (ε_{ij}) can be expressed in terms of the geometric mean of the potential energy parameters of like pair interactions (ε_{ii} and ε_{jj}) [63, 64].

$$\varepsilon_{ij} = \sqrt{\varepsilon_{ii}\varepsilon_{jj}} \qquad (5.2)$$

Good et al. showed that the solid liquid interfacial surface tension can be given by

$$\gamma_{sl} = \gamma_{lv} + \gamma_{sv} - 2\phi\sqrt{\gamma_{lv}\gamma_{sv}} \qquad (5.3)$$

where ϕ is Good's interaction parameter given by,

$$\phi = \frac{4(V_sV_l)^{1/3}}{(V_s^{1/3} + V_l^{1/3})^2} \qquad (5.4)$$

where, V_s and V_l are molar volume of solid and liquid, respectively [63]. Equation 5.3 was used for the calculation to determine the solid-liquid interfacial energy for the alumina-P(VDF-TrFE) system. The typical value for the Good's interaction parameter is unity, it might deviate when the predominant forces within the separate phases are of unlike type. For metal and organic compound pair, ϕ is expected to be less than unity [63].

Spreading Parameter

There exists two regimes of wetting i.e. partial wetting and complete wetting as shown in figure 5.2. The parameter that distinguishes the two wetting regimes is called the *spreading parameter* S. Which is given by the equation:

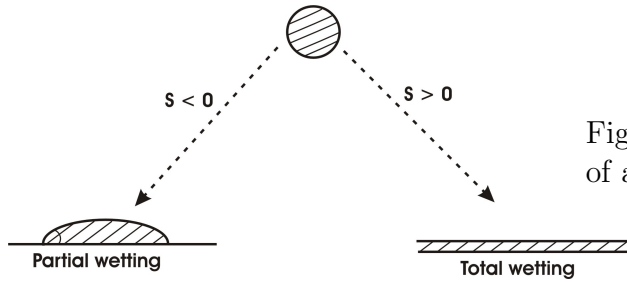$$S = \gamma_{sv} - (\gamma_{sl} + \gamma_{lv}) \qquad (5.5)$$

48

Figure 5.2: The two wetting regimes of a drop [62]

If the parameter S is positive, the liquid spreads completely in order to lower the surface energy of the substrate ($\theta_e = 0$), which is a *complete wetting* regime. In *partial wetting* state $S < 0$, the drop does not spread but forms at equilibrium a spherical cap resting on the substrate with a contact angle $\theta_e \leq 90°$. And when $\theta_e \geq 90°$, the liquid is in non-wetting state called as *complete drying* [62, 65].

High melting point solids such as diamond, sapphire, silica and most metals have free surface energies in the range of several thousands to several hundred mJ/m^2. Low melting solids such as organic polymers, waxes and covalent compounds in general have free surface energies ranging from 100 to 25 mJ/m^2. The former group is called high surface energy and the latter as low surface energy materials. Nearly all liquids other than liquid metals have free surface energy (γ_{lv}) less than 75 mJ/m^2. Each such liquid would be expected to spread spontaneously on any clean high energy surface because there would thereby be expected to result a decrease in the free surface energy of the system [66].

Wetting can be viewed as a direct consequence of Young's equation. If we change some thermodynamic variable, like temperature, the three surface tensions will change and, consequently, the contact angle will change. Therefore it is possible to go from complete wetting state ($\theta_e = 0$) through partial wetting state ($\theta_e \geq 90°$) to complete drying state ($\theta_e = 180°$), by changing the temperature. The *wetting transition* is a transition between a partial and a complete wetting state. If the system is studied as a function of temperature, the transition temperature is called the wetting temperature T_w [61].

Precursor film

It was observed for a complete wetting regime ($S > 0$), there exists a *precursor film* ahead of droplet which wets the substrate quickly, as shown in figure 5.3. In the precursor thin films there are long range interactions (van der Waals, electrostatics) between the film and the substrate. If we consider a
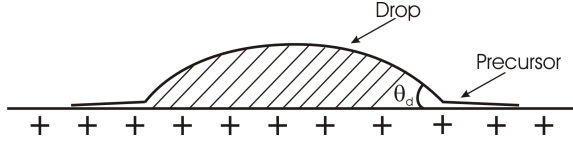
49

Figure 5.3: Spreading of a drop on a solid surface in total wetting regime [62]

film of thickness e on a substrate, the energy of the two interfaces is $\gamma_{sl} + \gamma_{lv}$. When the film becomes thin ($e \to 0$), the bare substrate energy γ_{sv} could be recovered. In between the two cases the energy dependence can by given by

$$Energy/m^2 = \gamma_{sl} + \gamma_{lv} + P(e) \tag{5.6}$$

Where $P(\infty) = 0$ and $P(0) = S = \gamma_{sv} - \gamma_{sl} - \gamma_{lv}$. The contribution to P(e) comes from long range van der Waals forces or electrostatic interactions. The stability condition in different regimes for a thin film can be determined by P(e) dependence. The interaction between two interfaces is given by the *disjoining pressure*,

$$\Pi(e) = -\frac{dP}{de} \tag{5.7}$$

when P(e) is a decreasing function of e, $\Pi(e)$ is positive. The long range van der Waals energy in the film (for a solid-liquid system) can given by

$$P(e) = \frac{A}{12\pi e^2} \tag{5.8}$$

where A has the dimension of an energy and called Hamaker constant, given by

$$A = \pi^2 k \alpha_l (\alpha_s - \alpha_l) \tag{5.9}$$

where the quantities α_l and α_s are the polarizabilities per unit volume of the liquid and solid, respectively, and k is the constant. The sign of the Hamaker constant determines the wetting or non-wetting behavior of the film. The Hamaker constant A is positive in complete wetting, the energy P(e) is then positive, the energy of a film increases as the thickness decreases and the van der Waals interaction has a thickening effect [62].

Dynamics of Triple Line

In case of partial wetting, the wetted portion is delimited by a certain *contact line l*. Three phases are in contact at the line: the solid S, the liquid L and the corresponding equilibrium vapor V. The contact angle θ_e results from a equilibrium between several forces near the contact line. If the liquid wedge is set in motion, the dynamic contact angle θ_d is different from equilibrium
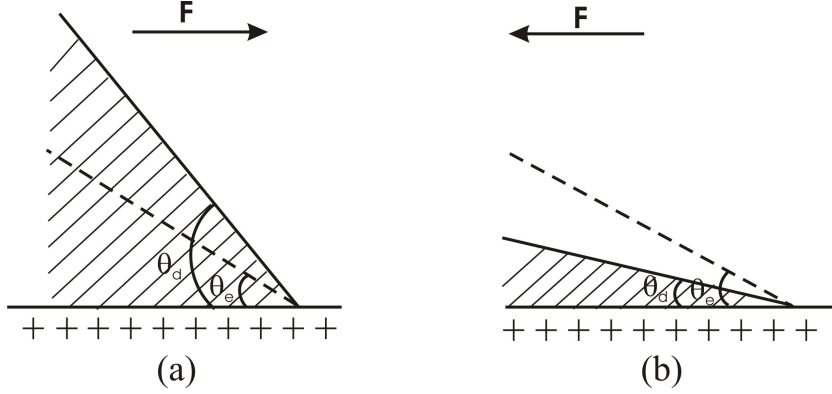
50

Figure 5.4: Non-equilibrium force exerted on the triple line: (a) F > 0; (b) F < 0 [62]

contact angle, θ_e, as shown in figure 5.4. The force traction pulling the liquid toward the dry region is given by,

$$F(\theta_d) = \gamma_{sv} - \gamma_{sl} - \gamma_{lv}cos\theta_d \qquad (5.10)$$

At equilibrium, $F(\theta_e) = 0$. If the force F is not zero then the triple line moves with velocity V [62]. Using equation 5.1, we can write,

$$F(\theta_d) = \gamma(cos\theta_e - cos\theta_d) \qquad (5.11)$$

In the limit of small angles, we have

$$F(\theta_d) \approx \frac{1}{2}\gamma(\theta_d^2 - \theta_e^2) \qquad (5.12)$$

The opposing force F_v to the $F(\theta_d)$ can be analyzed, by showing that the frictional force is proportional to both the viscosity, η, and the speed, U, and inversely proportional to the dynamical angle:

$$F_v \approx \eta\frac{U}{\theta_d} \qquad (5.13)$$

Equating the driving force and the frictional force, we obtain a equation for the motion of the liquid wedge,

$$U \approx \frac{\gamma_{lv}}{6\eta l}\theta_d(\theta_d^2 - \theta_e^2) \qquad (5.14)$$

where l is the dimensionless coefficient with range from 15 to 20 [62]. The above equation shows that the velocity of the liquid wedge is inversely proportional to the viscosity (η) of the wetting liquid. The velocity will also decrease as the dynamic contact angle, θ_d, is close to the equilibrium contact angle, θ_e, which is zero for the complete wetting regime.

5.1.2 Capillary rise

When a narrow tube is brought in contact with a complete or partial wetting liquid, some of the liquid rises inside the tube which is called capillary rise, as shown in figure 5.5. The liquid rises if the dry tube has a surface energy γ_{sv} greater than the surface energy γ_{sl} of the same tube when wet. Similar to wetting parameter S, for capillary rise the imbibition parameter, I, can be given as,

$$I = \gamma_{sv} - \gamma_{sl} = \gamma_{lv}cos\theta_e \tag{5.15}$$

For positive I the liquid rises in the capillary, when I is negative the liquid level drops in the tube [62]. Impregnation criteria ($I > 0$) can equivalently be written as $\theta_e < 90°$. The energy E of a liquid column can be written in terms of its height h and the radius R of the capillary:

$$E = -2\pi RhI + \frac{1}{2}\pi R^2 h^2 \rho g \tag{5.16}$$

where the first term is the gain in surface energy and the second is the cost in terms of gravitational potential energy. Minimizing E yields a height H of the capillary rise:

$$
\begin{aligned}
H &= \frac{2I}{\rho g R} \\
&= \frac{2\gamma_{lv}cos\theta_e}{\rho g R}
\end{aligned} \tag{5.17}
$$

where ρ is density and g is the acceleration due to gravity. The equation is derived under the condition that $R \ll H$ [62]. Equation 5.17 can also be
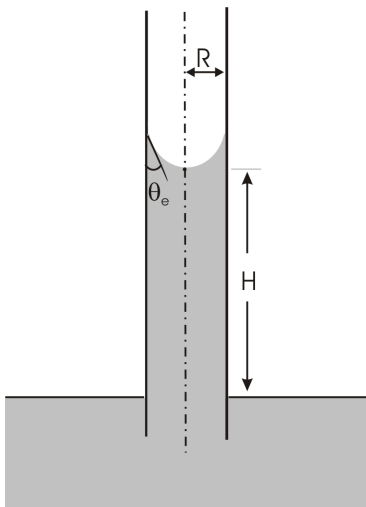

Figure 5.5: Capillary rise in a tube

written as,

$$H \approx 2k^{-2}\frac{1}{R} \tag{5.18}$$

where $k^{-1} = \sqrt{\gamma_{lv}/\rho g}$ is the *capillary length*, $cos\theta_e$ is neglected. When $R < k^{-1}$, gravity is negligible and capillary effects dominate [62, 65].

In case of partial wetting ($S < 0$) the liquid will rise in the capillary to reduce the solid-vapor interfacial energy by replacing the interface by the rising liquid. For the complete wetting ($S > 0$), the capillary rise is essentially a two step process. In a first step a precursor film wets the surface of the tube and in second step the capillary rise can occur. Initial formation of precursor film is unavoidable in complete wetting because the spreading of the precursor film is much faster than the capillary rise. The formation of liquid-vapor interface by the precursor film will lead to decrease in the driving force for the capillary rise in the second step. Therefore, the capillary rise will be very slow process in the complete wetting regime. Which in turn might cause other mechanisms to fill the capillary like with the formation of the instabilities, which is discussed in next section. The final minimum energy state will be complete filling of the capillary.

5.1.3 Wetting of Ordered Porous Alumina by Polymers: Thermodynamics

Wetting of porous alumina is the first step towards the formation of nanostructures. Alumina has high surface energy and polymer melt has low surface energy. Therefore, the P(VDF-TrFE) should completely wet the AAO nanopores. In order to study the wetting behavior of P(VDF-TrFE), first the thermodynamic parameter S is calculated and it is also shown that the gravity does not play a role for the capillary rise of P(VDF-TrFE) in the AAO nanopores. The calculations are done by considering the surface energy of PVDF which has a similar repeating unit to P(VDF-TrFE) because the surface energy data for P(VDF-TrFE) is not available.

Spreading parameter for PVDF

Spreading parameter, S, was calculated for PVDF melt on alumina substrate to know the wetting regime. The solid-liquid interfacial tension between alumina and PVDF was calculated by Good's equation 5.3 and 5.4. We have for PVDF $\gamma_{sv} \approx \gamma_{lv} = 32.7 \times 10^{-3}\,J/m^2$ [67] and for alumina $\gamma_{sv} = 1.59\,J/m^2$ [68]. The molar volume of PVDF, $V_l = 32\,cm^3/mol$ and for alumina $V_l = 12.84\,cm^3/mol$. Which gives us the Good's parameter,

$\phi = 0.98$. Putting these values in equation 5.3, gives us $\gamma_{sl} = 1.17\,J/m^2$. Then the spreading parameter S can be given by equation 5.5,

$$
\begin{aligned}
S &= \gamma_{sv} - (\gamma_{sl} + \gamma_{lv}) \\
&= 1.59 - (1.17 + 32.7 \times 10^{-3}) \\
S &= 0.387\,J/m^2
\end{aligned}
\tag{5.19}
$$

PVDF shows positive spreading parameter. Given that the surface tension difference for melt and solid polymers is 20-30 %, therefore in any case S will remain always positive and wetting of alumina by PVDF will be always in complete wetting regime. It is expected that the spreading parameter, S, will be positive and larger for P(VDF-TrFE) than PVDF because with higher fluorine content in P(VDF-TrFE) the γ_{lv} will be smaller than PVDF.

Capillary rise of PVDF in Porous Alumina

For special case of PVDF we can calculate the capillary length and capillary rise.

surface tension of PVDF, $\gamma_{sv} \approx \gamma_{lv} = 32.7 \times 10^{-3}\,J/m^2$ [67]
density of PVDF, $\rho = 1.78 g/cm^3 = 1.78 \times 10^3\,kg/m^3$ [67]
acceleration due to gravity, g = 9.8 m/s^2

$$
\kappa^{-1} = \sqrt{\frac{32.7 \times 10^{-3}}{1.78 \times 10^3 \times 9.8}} = 1.37 \times 10^{-3} m = 1.37\,mm
\tag{5.20}
$$

The capillary length κ^{-1} suggest that for PVDF there are no gravitational effects up to about 1.37 mm. The capillary rise for PVDF inside a porous alumina template of 400 nm diameter can be calculated by equation 5.17.

radius of the capillary, R = 200 nm = 200 $\times 10^{-9}$ m
equilibrium contact angle, $\theta_e = 0°$

$$
H = \frac{2 \times 32.7 \times 10^{-3} cos 0}{1.78 \times 10^3 \times 9.8 \times 200 \times 10^{-9}} = 18.74\,m
\tag{5.21}
$$

The above calculation show that the PVDF melt can rise up to 19 m in a 400 nm AAO nanopore ($R \ll \kappa^{-1}$). The AAO nanopores are 100 μm long therefore comparing the capillary length of 19 m, gravity will have no effect on the wetting of the nanopores. Also, the positive wetting parameter shows that the P(VDF-TrFE) will completely wet the AAO nanopores and the final equilibrium state will be the complete filling of the nanopores. How the complete filling is achieve is decided by the kinetics of the wetting process.

5.1.4 Wetting of Ordered Porous Alumina by Polymers: Kinetics

For wetting of AAO nanopores by polymer melt, two dominant wetting mechanisms have been reported [21,60]. They are, precursor wetting and capillary wetting mechanisms. In precursor wetting, a thin liquid precursor film wets the alumina surface, forming tubes. Freezing the melt at this stage will result in formation of nanotubes [19,59]. Nanorods will be formed if the radius of the pores is smaller than precursor film thickness [21].

The second spreading mechanism, capillary wetting was observed for block copolymers and highly viscous polymer melts. In capillary wetting, the polymer melt fills the nanopores by capillary rise. The capillary wetting results into formation of nanorods as the whole liquid front is sucked into the nanopores [5,69]. Russell et al. have found transition from nanotubes to nanorods when the wetting temperature is reduced or when the molecular weight is increased [60]. That is the wetting mechanism is changed from precursor wetting to the capillary wetting. They have attributed this change to the spreading parameter, S, which changes from positive for precursor wetting to negative for capillary wetting mechanism. However, this view is contradictory to our view of filling of the AAO nanopores. The change in surface energy between liquid and solid polymer is only 10-20% therefore it is difficult to change the S only by changing temperature. It is possible that high viscosity of the melt is responsible for the capillary wetting. However, the role of viscosity is not yet clear to us and it is still a open question.

The thickness of the precursor film is an important parameter determining the wall thickness of the nanotubes inside the nanopores. So far, there are no studies showing the thickness of the polymer precursor film wetting the nanopores. Direct comparison with the wetting of polymer on flat surfaces will yield different results. There are differences between wetting of the flat surface and wetting of the nanopores. For the wetting of the flat surface by a liquid drop, the final thickness of the film is e_c, which is larger than the molecular size of the liquid. For the polymer wetting the AAO nanopores the criteria for the final thickness will be different as there is effectively an infinite reservoir of liquid wetting a finite surface area. This could result in the thickness differences for the precursor film on a flat surface and in the nanopores. Studies of PDMS wetting a flat surface showed the precursor film thickness in few angstrom range [70,71]. The thickness of the film determined by ellipsometry is measured farther from the drop at a distance in millimeter range. For the polymer wetting the AAO nanopores, the farthest distance is 100 μm. Which means the precursor film is much closer to the droplet or the film is at the foot of the droplet. Which could result in much thicker precursor

films in the nanopores than on the flat surfaces for the same polymer.

Irrespective of the wetting mechanism, the equilibrium state is the completely filled pores. The kinetics of the wetting mechanism inside the AAO nanopores decides the morphology of the nanostructures. In case of precursor wetting, after the polymer covers the pore surface by a precursor film, a new polymer-air interface is created which should be replaced by polymer to reduce the interfacial energy. How the polymer-air interface is replaced by polymer and the pore is completely filled is still an unsolved problem. Here we present some routes by which the complete filling could be achieved. All these processes, given below, are interrelated and can occur at different time scale.

1. **Pore filling by thickening of precursor film and meniscus movement:** The precursor wetting leads to tube formation in the AAO nanopores. As shown in figure 5.6, the nanopores has a radius r and the inner tube radius r_i, with this we have a inner surface area of the tube $2\pi r_i L$, where L is the depth of the pores. The equilibrium will reach when the tube is completely filled and the inner surface area becomes zero or $r_i \to 0$. To achieve the equilibrium state it is possible that the r_i is decreased by increasing the thickness of the tube. The thickening could take place at the entrance of the tube accompanied by the meniscus. The thickness of the tube wall will have some gradient with maximum thickness at the top of the tube and decreasing towards the bottom. The pore filling will take place with simultaneous thickening of the tube walls and movement of the meniscus towards bottom of the tube. It is unclear on what timescale the complete filling can take place but for polymer it could be on the order of several days.

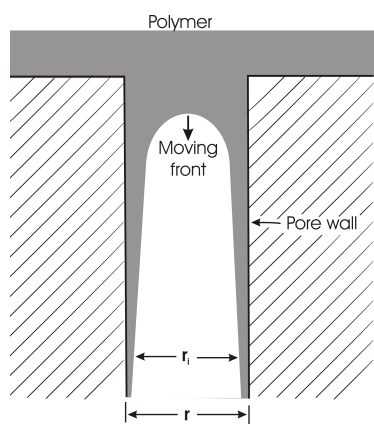2. **Instabilities and snap-off:** In case of low molecular weight liquid,

Figure 5.6: A nanopore in contact with polymer melt, the tube wall is thickening by the melt on the template surface

like water, it was observed that initially water form a precursor film on the pore walls, creating an air-water interface. The thickness of the film increases as more water flows into the pores and at an instability a neck is formed. Finally, increasing thickness leads to snap off of the neck and water fills the entire cross section of the capillary [72]. Infiltration by snap-off mechanism is shown in figure 5.7. Similar mechanism may be responsible for filling of the AAO nanopores with polymer.
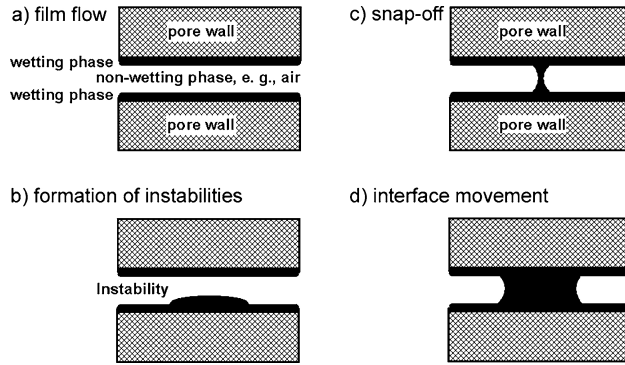

Figure 5.7: Infiltration of low molecular liquid in cylindrical channel, describing the snap-off mechanism [21]

3. **Rayleigh instabilities:** When a cylinder is covered with a liquid film, the film surface undulates with a wavelength λ to reduce the surface area and hence the surface energy of the liquid film as shown in figure 5.8. The modulation in the film thickness results into $e^\star < e_0$ with e_0 as initial film thickness, this results into reduction of surface area of the liquid. The wavelength of the perturbations is given by,

$$\lambda = 2\pi\sqrt{2}r \qquad (5.22)$$

where r is the radius of the cylinder. And the equation is valid for $e \ll r$ and the long range interactions are neglected $[P(e) \to 0]$. As the amplitude of the perturbations grows, crest are formed on the film which are eventually merge to form bridges. And a regular structure with bridges and holes is formed [62,73]. In case of nanopores in contact with the polymer melt the holes could be eventually filled to form rods.

Any of the above mechanisms could be responsible for complete filling of the pores.
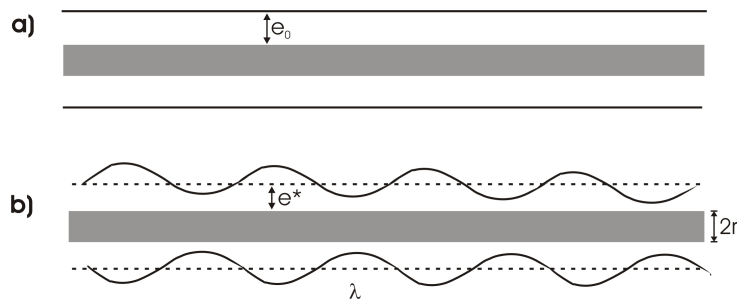
57

Figure 5.8: Rayleigh instability, a) liquid film on a fiber and b) destabilized film

5.2 Morphology of the P(VDF-TrFE) Nanostructures: Expectations and Conclusions

TEM and SEM was used to study the morphology of the P(VDF-TrFE) nanostructures. The aim of the study was not only to determine the morphology of the nanostructures but also to know how the wetting of AAO nanopores was achieved. As we have seen in the previous section the wetting mechanism determines the tube or rod formation inside the nanopores. Depending on the tube or rod morphology, the confinement experienced by the polymer will change. That is, for tubes the confinement will be determined by the wall thickness of the tube while in the rods, the confinement will be determined by the diameter of the rod. Tube morphology will have stronger confinement than rods for the same diameter of the nanostructures. Therefore it is important to differentiate between tube and rod morphology.

Also, in the previous section, we looked at the spreading parameter, S, and it suggested that the P(VDF-TrFE) should wet the template by precursor wetting mechanism. Is it the case? And what is the timescale and temperature dependence of the precursor wetting? As described in section 5.1.4 different mechanisms can be responsible for filling of the pores. All these processes can happen at different timescale, therefore samples wetted with short (10 minutes) and long time (12 hours) were prepared to study the morphology.

5.2.1 P(VDF-TrFE) 400 nm Nanostructures

Filling time of AAO nanopores

Polymers are highly viscous, even well above the melting temperature, therefore to completely wet the 100 μm deep AAO nanopores takes long time. Figure 5.9 shows the SEM images of the samples prepared at 200°C and 250°C for wetting time of 10 minutes and cooled with 1 K/min to 30°C. The length of the tubes is 16 μm and 31 μm for sample prepared at 200°C and 250°C, respectively. This result shows the relationship of viscosity and wetting speed of polymer melt as shown by the equation 5.14. With rise in temperature (at 250 °C) the viscosity is decreased and the wetting becomes faster resulting in longer tubes for the same wetting time. The result also shows that 10 minutes wetting time is not enough to fill the pores completely. Therefore, samples were prepared with different wetting time but the same wetting temperature of 250 °C and the evolution of the morphology was observed with TEM and SEM. Samples with different wetting time were prepared in order to a) evaluate the time required to completely fill the 100 μm pores, b) check if there are instabilities during the long wetting time and c) determine if there is a transition from tube to rod morphology. The experiments to determine the filling time of the nanopores by P(VDF-TrFE) were only carried out on 400 nm nanopores as it was expected that the filling time will not change for the different diameter pores.

Figure 5.10 a, shows upper part of a template, wetted by P(VDF-TrFE) at 250°C for 2 hours, showing the surface film and pore walls wetted by the polymer. The AAO nanopores containing P(VDF-TrFE) was mechanically broken after the removal of the aluminium base. Side view of the fractured
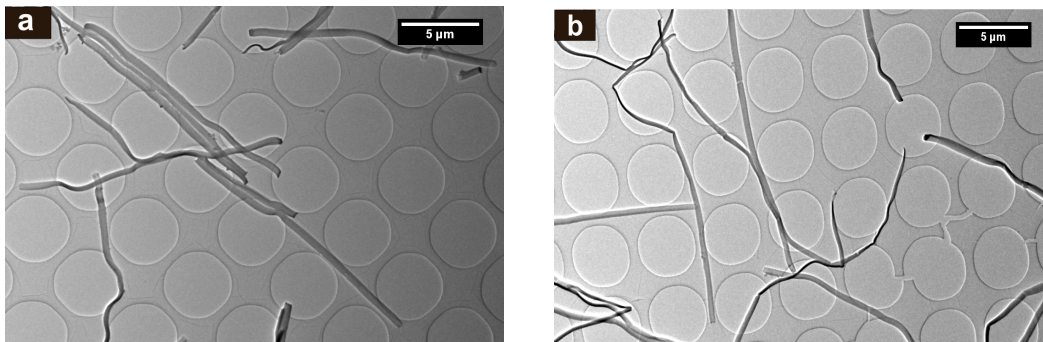

Figure 5.9: TEM images of 400 nm nanotubes, a) sample wetting at 200°C and b) sample wetting at 250°C; both the samples wetted for 10 minutes and cooled with 1 K/min
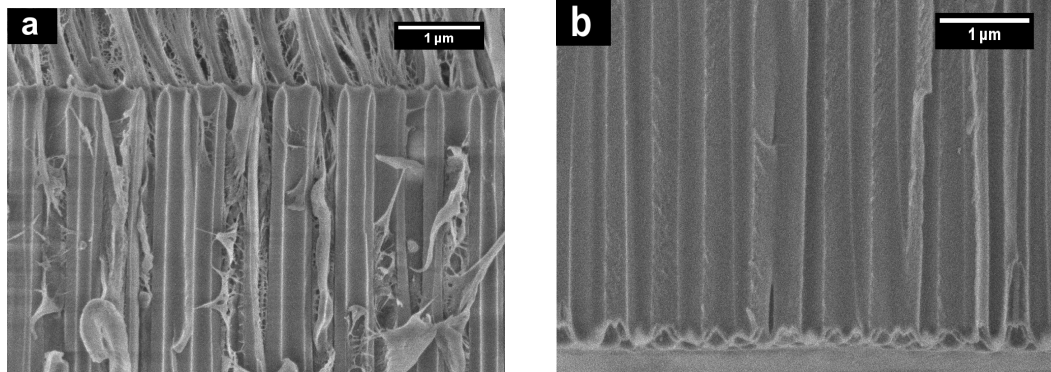
Figure 5.10: SEM image showing side view of 400 nm diameter alumina template filled with PVDF-TrFE, wetting temperature 250°C for 2 hours, a) shows the upper part of the template and b) the bottom part of the template
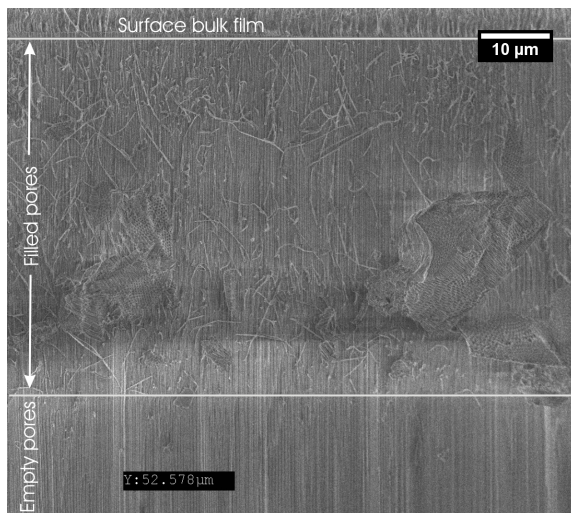

Figure 5.11: SEM image showing side view of 400 nm diameter alumina template, it shows the extent of filling of P(VDF-TrFE) inside the nanoporous alumina

sample is viewed under the SEM. The film morphology on the pore walls shows that the pores are wetted by precursor film. The surface film on the template shows some stretched nanostructures coming out which could be due the mechanical force applied during the removal of surface film by a scalpel. The bottom part of the same template is shown in figure 5.10 b, it shows the empty bottom where the polymer has not reached. The complete view of the template is show in figure 5.11, where we can see sections in the template, the uppermost part is the surface film, the middle part is the pores filled with P(VDF-TrFE) and the third part is the empty bottom. The length of the filled part is 53 μm after 2 hours. We have seen that for 10 minutes of wetting time the nanostructures are 31 μm long at 250°C. Therefore it appears that the wetting becomes slower towards the bottom
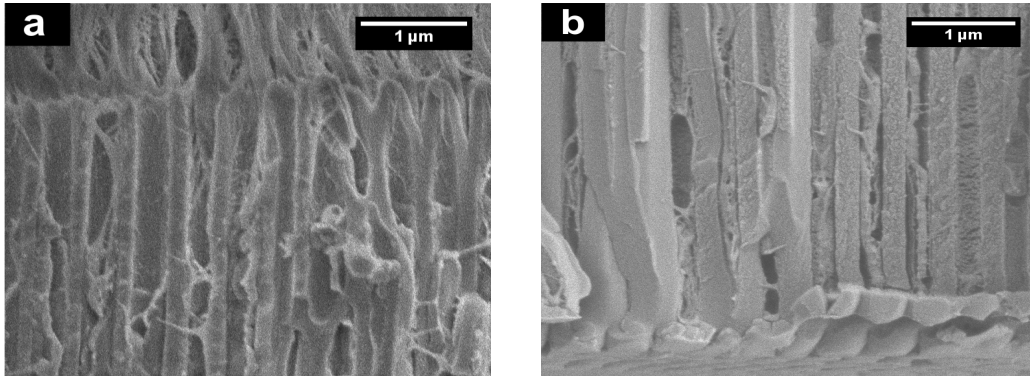
Figure 5.12: SEM images showing side view of 400 nm diameter alumina template filled with P(VDF-TrFE), wetting temperature of 250 °C for 12 hours, a) shows the upper part of the template and b) the bottom part of the template

of the AAO nanopores. That is, close to the melt reservoir near the surface of the template the wetting is much faster. The initial fast wetting of the AAO template could be attributed to the small force applied by the spatula on the polymer melt during the spreading of the polymer melt on the AAO template surface.

It was observed that the template is completely filled, i.e. 100 μm depth, after wetting the template at 250°C for 12 hours. The figure 5.12 shows the SEM images of the top and bottom part of the template which are filled to the bottom after 12 hours wetting time. The 400 nm samples did not showed any instabilities during this long wetting time.

Morphology of the 400 nm Nanostructures

The P(VDF-TrFE) nanostructures were prepared at wetting temperature of 200°C and 250°C, the sample details are given in table 5.1, all the samples were cooled to 30°C. The figure 5.13 shows the cP_{400}-200-12h sample, which show tube morphology. The TEM image in figure 5.13 a we can see the dark borders with brighter middle part of P(VDF-TrFE) 400 nm tubes. The contrast between the edges and in the middle part of the TEM image gives us clear indication of tube morphology of the nanostructures. The SEM image (figure 5.13 b) shows the walls of the porous alumina are wetted by P(VDF-TrFE) film which confirms the tube morphology of the sample.

Figure 5.14 shows the TEM and SEM image of sample cP_{400}-200-10m. The TEM image (figure 5.14 a) does not give us clear indication of tube morphology. But in the SEM image (figure 5.14 b), we can clearly see the
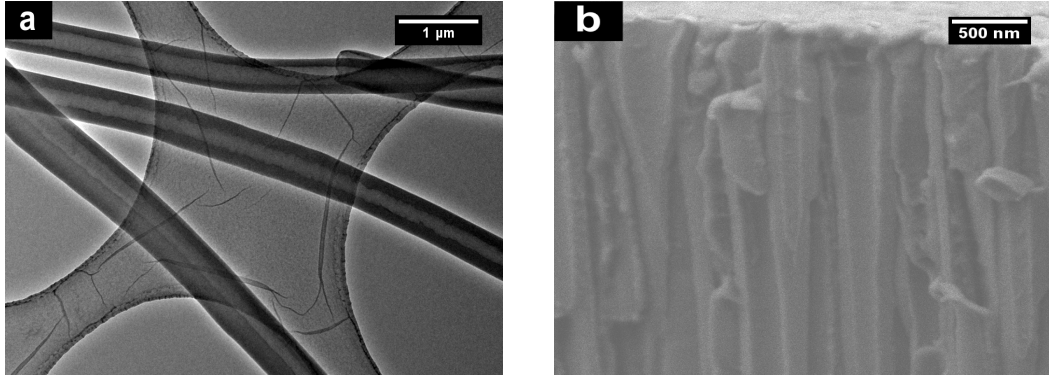
Figure 5.13: Sample cP_{400}-200-12h (a) TEM image and (b) SEM image showing the tube morphology of the nanostructures

P(VDF-TrFE) tubes coming out of the porous alumina template.

The TEM and SEM image of sample cP_{400}-250-12h is shown in figure 5.15. Again, the TEM (figure 5.15 a) image does not give clear information about the tube morphology. However, the SEM image (figure 5.15 b) shows the bulk polymer on the surface of the template and the pores inner surface is covered with the polymer film. Which indicate the tube morphology of the nanostructures. It appears that the tube walls become thicker after 12 hours of wetting time. Breaking the template having thick tubes results into large amount of polymer on the template walls figure 5.15 b.

Figure 5.16 a and figure 5.16 b shows TEM and SEM image of a P(VDF-TrFE) nanostructures sample cP_{400}-250-10m. The TEM image (Figure 5.16 a) shows the tube morphology of the P(VDF-TrFE) nanostructures. In the SEM image we can see the openings of the P(VDF-TrFE) tubes (Figure 5.16 b) and the wall thickness of the tube is approximately 60 nm.

Sample name	Wetting temperature	Wetting time	Cooling history
cP_{400}-200-12h	200 °C	12 hours	1 K/min
cP_{400}-200-10m	200 °C	10 minutes	1 K/min
cP_{400}-250-12h	250 °C	12 hours	1 K/min
cP_{400}-250-10m	250 °C	10 minutes	1 K/min
qP_{400}-200-10m	200 °C	10 minutes	quenched
qP_{400}-250-10m	250 °C	10 minutes	quenched

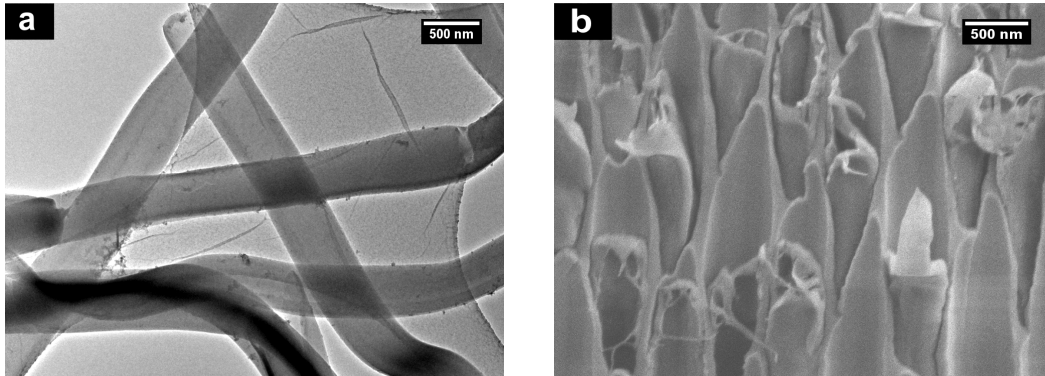Table 5.1: P(VDF-TrFE) 400 nm nanostructures sample details

Figure 5.14: Sample cP_{400}-200-10m: (a) TEM image and (b) SEM image with nanotubes embedded in alumina. Tube morphology is observed.
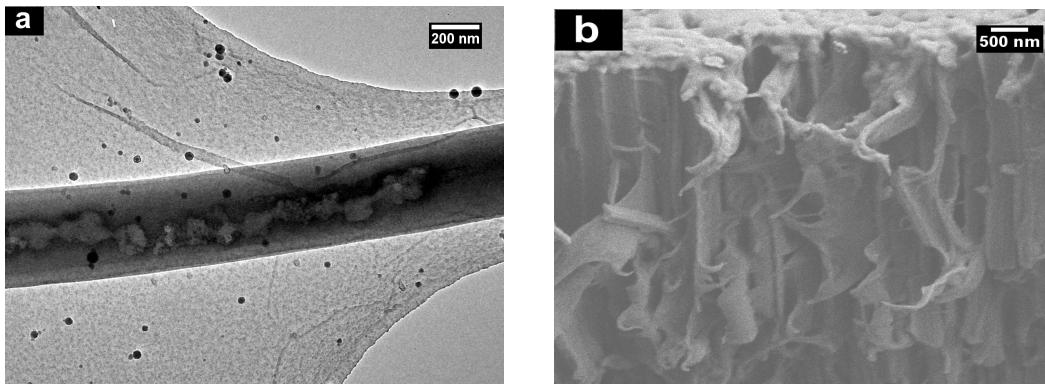

Figure 5.15: Sample cP_{400}-250-12h (a) TEM image and (b) SEM image
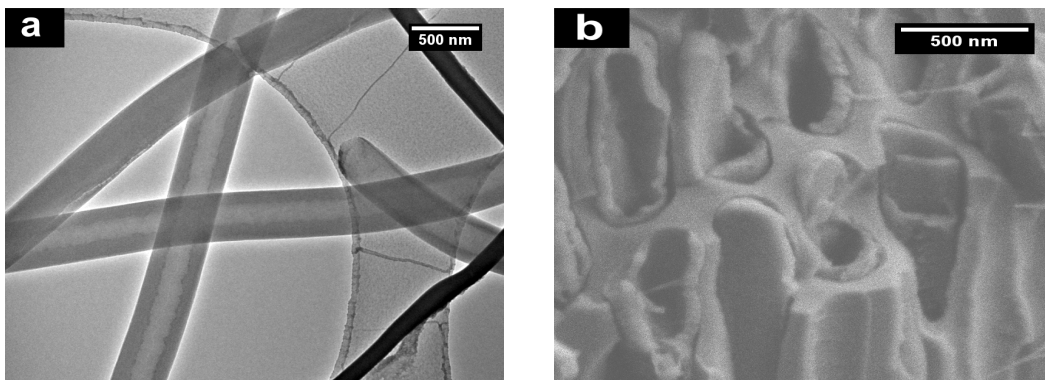

Figure 5.16: Sample cP_{400}-250-10m, (a) TEM image and (b) SEM image showing the tube morphology of the nanostructures
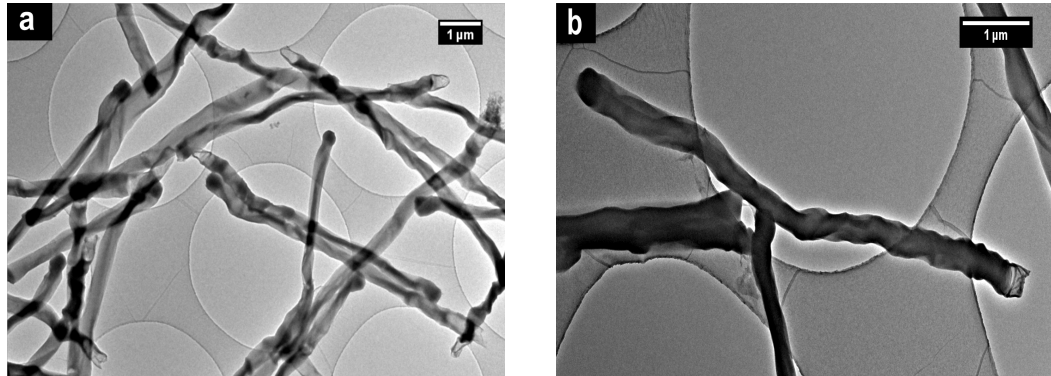
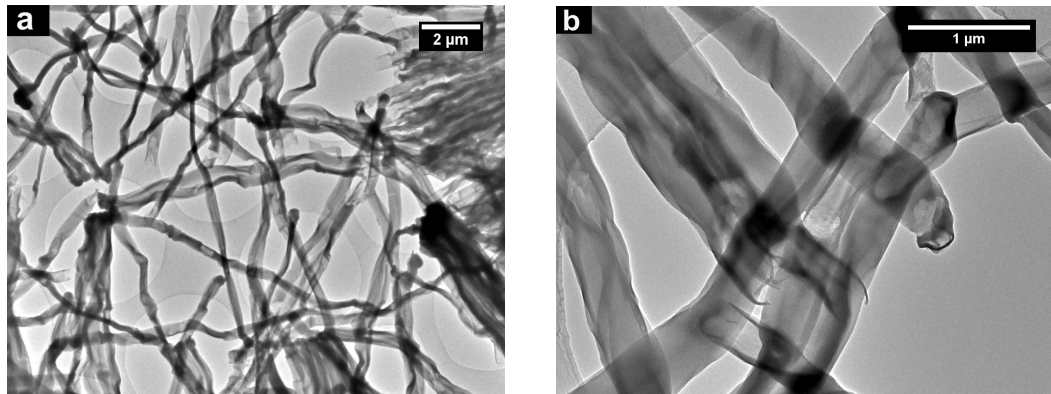Figure 5.17: TEM images of 400 nm quenched sample qP_{400}-200-10m

Figure 5.18: TEM images of 400 nm quenched sample qP_{400}-250-10m

Figure 5.17 and figure 5.18 shows the TEM images of samples qP_{400}-200-10m and qP_{400}-250-10m, respectively. Both the samples were rapidly cooled by removing them from the furnace to the room temperature. They show similar morphology. The samples seems to be mechanically unstable and unlike the smooth surface of slowly cooled samples, the quenched samples shows wrinkles. The wrinkles might result from the difference in cooling between the alumina wall and polymer.

The tube morphology in all the 400 nm samples suggest that the wetting take place with precursor wetting mechanism. Which was also suggested by the positive spreading parameter, S, which was calculated in section 5.1.3. The tube morphology observed for the samples prepared at 200°C and 250°C suggest that there is no wetting transition from precursor wetting to capillary wetting. None of the samples showed instabilities which means the wetting time of 12 hours was not enough to set in the instabilities in the 400 nm nanostructures.

5.2.2 Morphology of 60 nm and 35 nm Nanostructures

The sample details of the 60 nm nanostructures are shown in table 5.2. Figures 5.19 and 5.20 show some TEM images of the 60 nm nanostructures samples. The images are inconclusive either for tubes or rods. As was seen in the 400 nm nanotubes, some of the TEM images showed no contrast for tubes and the problem was solved by analyzing the cross section of the sample with SEM. In case of 60 nm and 35 nm nanostructures the SEM images were also inconclusive due to the resolution limit.

Sample name	Wetting temperature	Wetting time	Cooling history
cP_{60}-200-12h	200 $°C$	12 hours	1 K/min
cP_{60}-200-10m	200 $°C$	10 minutes	1 K/min
cP_{60}-250-12h	250 $°C$	12 hours	1 K/min
cP_{60}-250-10m	250 $°C$	10 minutes	1 K/min

Table 5.2: P(VDF-TrFE) 60 nm nanostructures sample details
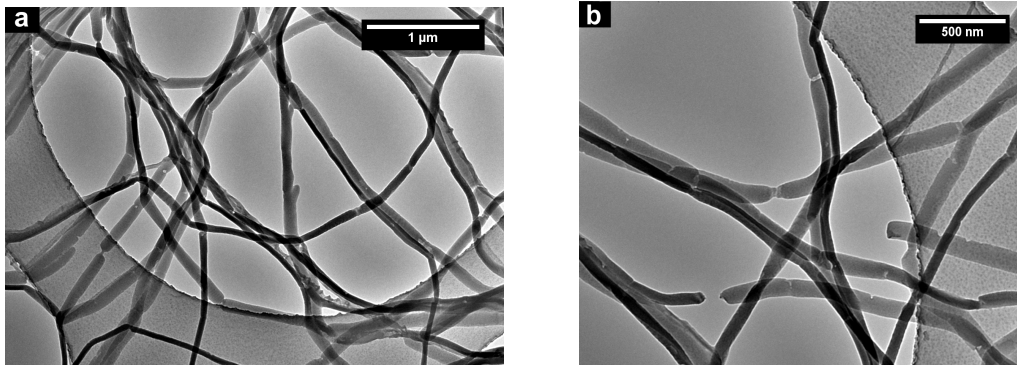
Figure 5.19: TEM images of P(VDF-TrFE) 60 nm sample cP_{60}-200-12h

Figure 5.21 shows the TEM images of 35 nm and 60 nm nanostructures prepared at $250°C$ for 12 hours and cooled with 1 K/min, the images show the regular voids in the nanostructures, which is a sign of Rayleigh instabilities. The voids in the Rayleigh instability occur at a specific wavelength, λ, given by equation 5.22. The equation shows that the wavelength to radius ratio, λ/r, is a constant which is equal to 8.88 [62]. For the 60 nm P(VDF-TrFE) nanostructures λ/r was found to be 4.66, for $\lambda = 140$ nm and $r = 30$ nm. And for the 35 nm nanorods the λ/r ratio is 5.1. Chen et al. has found the ratio, λ/r, to be between 6.5 to 4.5 for PMMA filled in capillary of radius

65

Figure 5.20: TEM images a) cP_{60}-200-10m and b) cP_{60}-250-10m
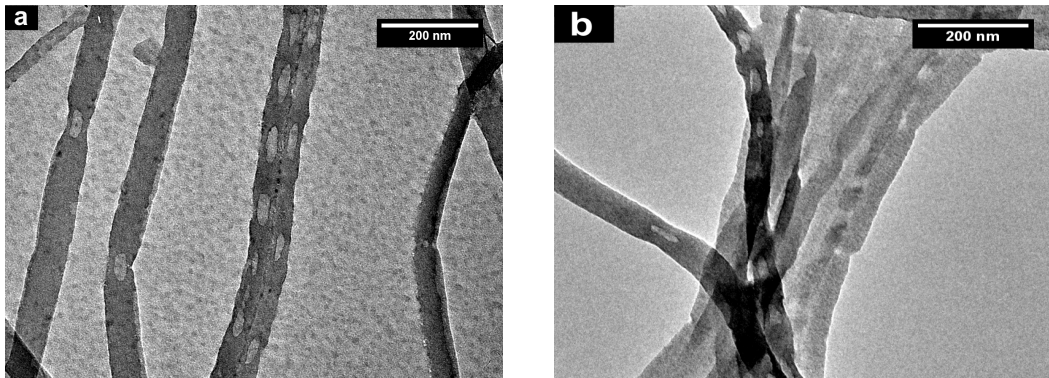
Figure 5.21: TEM images samples wetted at 250°C for 12 hours and cooled with 1 K/min, a) 60 nm nanostructures and b) 35 nm nanostructures
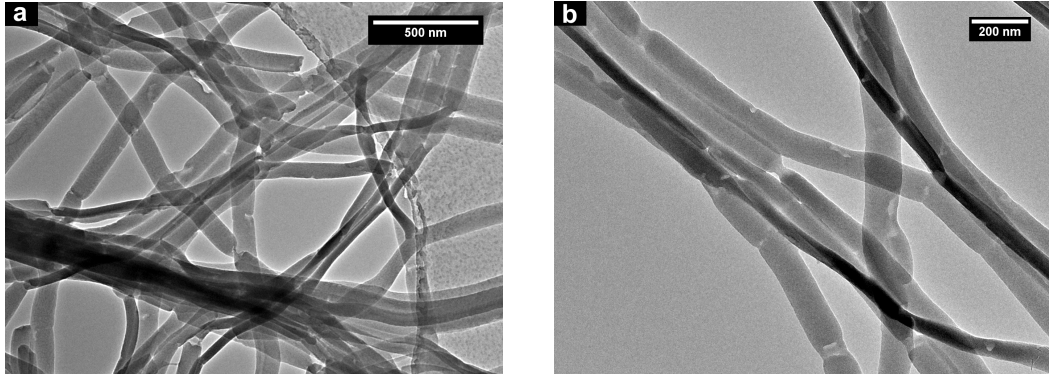
120 nm to 270 nm, respectively [74]. The difference between the theoretical value and experimental value could arise due to small film thickness (e) where the long range forces are active, in equation 5.22 long range forces are not considered.

The Rayleigh instabilities show that at the initial stage the pores are wetted by precursor film forming tubes which are latter completely filled with the polymer with intermediate state of Rayleigh instabilities. Capillary wetting of AAO template can not explain the Rayleigh instability, therefore capillary wetting mechanism for alumina-P(VDF-TrFE) system can be excluded. Not all the nanostructures showed the Rayleigh instabilities. In 60 nm nanostructures only 20-30% and in 35 nm nanostructures less than 10% nanorods showed these instabilities. Which could mean that close to the surface film the morphology is already rods and at the bottom of the template filling of P(VDF-TrFE) is still taking place which show the Rayleigh instabilities.

Therefore it is possible that in the small pores (60 nm and 35 nm) there is a coexistence of the tube and rod morphology. It is likely that for a short wetting time of 10 minutes the morphology in 35 nm and 60 nm nanopores is tubes, as no voids are seen for 10 minutes wetting time, which after 12 hours of wetting time at $250°C$ becomes rods.

5.3   Summary

We have shown that the P(VDF-TrFE) wets the AAO nanopores in complete wetting regime resulting in precursor wetting mechanism. The precursor wetting mechanism was evident from the tube morphology of the 400 nm nanostructures. There is a continuous evolution of the morphology inside the nanopores for a long wetting time (12 hours). That is, thickening of the tube walls is possible in large pores (400 nm) or Rayleigh instabilities are observed for the smaller pores (35 nm and 60 nm). The morphology of the small nanostructures (35 nm and 60 nm), for 10 minute wetting time, was difficult to determine and presumed that they show tube morphology.

Chapter 6

Phase Transitions in P(VDF-TrFE) Nanostructures

By increasing the temperature of P(VDF-TrFE) a solid-solid transition is observed at Curie temperature (T_C), the transition is related to the transformation of the ferroelectric phase into the paraelectric phase, as described in chapter 2. At the Curie temperature the ferro- to para- phase transition is accompanied by loss of remnant polarization (P_r), increase in dielectric constant (ε), increase in thermal expansion, decrease in bulk modulus and increase in specific heat (C_p) [36, 75]. The ferro- to para- transition was intensively studied by various group for the relationship between T_C and VDF content, annealing temperature and polarization [29, 30, 32, 34, 40, 76]. In this chapter, we describe the DSC results for bulk P(VDF-TrFE) as well on the nanostructures having different diameters. The DSC measurements were carried out to study the effect of confinement on T_C, melting and crystallization temperatures. The DSC measurements were carried out on Perkin-Elmer DSC-7. All the nanostructure samples were prepared by wetting at $200°C$ for 10 minutes and cooling the sample to $30°C$ with a cooling rate of 1 K/minutes. Afterwards the bulk surface film was removed from the sample surface. The P(VDF-TrFE) nanostructures were embedded in the nanoporous alumina during the DSC measurements. More detailed sample preparation for DSC is described in chapter 2. For the short wetting time of 10 minutes the 400 nm, 180 nm, 60 nm and 35 nm nanostructures tube morphology was observed, as discussed in the chapter 5.2. Further, the sample names, preparation details and morphology is give in appendix-I.

6.1 Effect of Confinement on Phase Transitions

The lamellae thickness in the bulk P(VDF-TrFE) is more than 50-60 nm thick, as discussed in chapter 2 from the SAXS measurements. Confining the polymer should decrease the melting temperature because the confinement will restrict the lamellae thickness depending on the extent of confinement. Therefore, relationship between different crystal thicknesses, by varying the confinement, and the ferro- to para phase transition can be studied. Also, the crystallization mechanism is expected to change from heterogenous nucleation in bulk to homogeneous nucleation in the nanopores. The individual entity in each nanopores has to crystallize separately and the decrease in volume of the polymer forces the polymer to crystallize with homogeneous nucleation [10, 77, 78]. All these effects were studied for the nanostructures and for the bulk P(VDF-TrFE) for comparison.

Figure 6.1 shows the heating and cooling scans of bulk P(VDF-TrFE) and nanostructures of 400 nm, 180 nm, 60 nm and 35 nm diameters. The DSC measurements were carried out with a scan rate of 20 K/min. The DSC scan of the bulk shows two phase transitions, each, during heating and cooling. During the heating scan, the first peak at $125°C$ corresponds to the ferro- to para- phase transition at the *Curie temperature*, T_C. The second peak, during heating, at $150°C$ corresponds to the melting, T_m, of P(VDF-TrFE). During cooling the crystallization is observed at $135°C$, T_{cry}. After the crystallization the polymer is in the paraelectric hexagonal phase which is transformed into the ferroelectric phase at $76°C$, T_{p-f}. The DSC scans show that the ferro- to para- transition during heating and para- to ferro-transition during cooling show a large temperature difference. This is a sign of first order phase transition. During cooling the transition to the ferroelectric phase takes place with the nucleation and growth of the ferroelectric domains in the paraelectric phase. Therefore high supercooling is necessary.

The peak transition temperatures for bulk P(VDF-TrFE) and the nanostructures is shown in table 6.1, taken from DSC heating and cooling scans. During cooling of the nanostructures, the para- to ferro- transition, T_{p-f}, shows a broad transition without a peak therefore T_{p-f} for the nanostructures is not indicated in the table 6.1. However, the width of the T_{p-f} transition is similar for the bulk and the nanostructures. Comparison between the Curie temperature, T_C, of bulk P(VDF-TrFE) and the nanostructures samples reveals that the T_C does not change with increasing confinement. The peak melting temperature, T_m, is similar for the 400 nm and 180 nm nanostructures and the bulk. However, a closer look at the onset melting
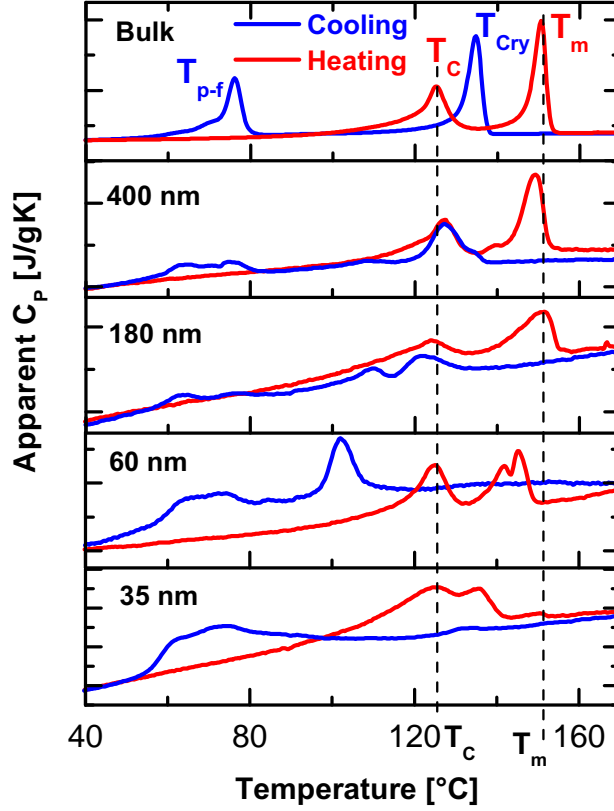
Figure 6.1: DSC heating and cooling scans with scan rate of 20 K/min, for bulk P(VDF-TrFE) and the nanostructures. The peak temperatures for the bulk P(VDF-TrFE) are shown: T_{p-f} - para- to ferro- transition, T_c - Curie temperature, T_{cry} - crystallization temperature and T_m - melting temperature.

temperature suggests the melting temperature is indeed decreased in the 400 nm and 180 nm nanotubes. The bulk melting temperature is further reduced when the confinement is increased to 60 nm and 35 nm. The decrease in the melting point is related to the increase in the Gibbs free energy as the surface area to the volume ratio increases with the confinement. This melting point depression in the nanopores is given by the Gibbs-Thomson equation,

$$\Delta T_m = T_m - T_m(d) = 4\gamma_{sl}T_m/(d\Delta H_f \rho_s) \qquad (6.1)$$

where, ΔT_m is the melting point depression, d is the crystal size, T_m is the melting temperature of bulk, $T_m(d)$ is melting point of crystal of size d, γ_{sl} is the surface energy of solid-liquid interface, ΔH_f is the enthalpy of fusion and ρ_s is the density of the solid [77,78]. Therefore, the DSC results suggest

71

Pore diameters	T_C (°C)	T_m (°C)	T_{cry} (°C)	T_{p-f} (°C)
Bulk	125	151	135	76
400 nm	125	150	127	-
180 nm	125	151	122	-
60 nm	125	145	101	-
35 nm	125	135	-	-

Table 6.1: Peak transition temperatures for bulk P(VDF-TrFE) and the nanostructures from the DSC scans shown in figure 6.1

that with increasing confinement the crystal size is decreasing resulting in decreasing T_m.

The DSC scans show that the Curie temperature, T_C, remains constant for the bulk and also in the confinement for the nanostructures. This is surprising as the decrease in the melting temperature show that the crystal thickness is decreasing with increase in confinement but there is no effect on the T_C. The reason for increase in T_m and no change in T_C by increasing confinement is related to the increase in the Gibbs free energy in the confinement. By increasing the confinement the surface area to volume ratio of the nanostructures is increased resulting in the increase of the Gibbs free energy for the paraelectric as well as for the ferroelectric phase. Figure 6.2 shows the Gibbs free energy for ferroelectric phase, paraelectric phase and the melt. The intersection of the paraelectric line with melt line represent the first order ferro- to para- phase transition, T_C. And the intersection of the paraelectric line with the melt line represent the first order solid to melt transition, T_m. The increase in the confinement leads to increase in the Gibbs free energy and the ferroelectric and paraelectric lines are shifted upwards, dashed lines in figure 6.2. Due to the upward shift of both the ferroelectric and paraelectric lines, in confinement, they intersect at the same temperature as before and therefore there is no change in the T_C. It is a different case for the melt line, it intersect the paraelectric line in confinement (dashed line) at lower temperature. Therefore the T_m is decreased.

Comparison of the bulk crystallization temperature, T_{cry}, with the nanostructures shows that with increasing confinement the crystallization temperature is decreasing, from table 6.1. In case of 35 nm nanostructures, which show tube morphology in chapter 5, there is a very high supercooling for crystallization resulting in merging of the crystallization peak with the para- to ferro- phase transition peak, leading to a broader peak. The decrease in the crystallization temperature with increasing confinement shows that the
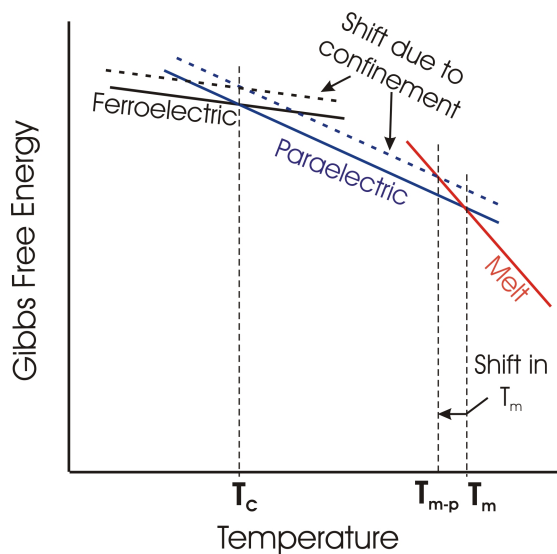
Figure 6.2: The Gibbs free energy increases due to the increasing confinement (dashed lines) for paraelectric phase and the ferroelectric phase which leads to decrease in the melting temperature (T_m) but the Curie temperature (T_C) remains the same

nucleation mechanism is changed from heterogeneous in bulk to homogeneous nucleation in the nanostructures. Normally in the bulk samples the heterogeneous nucleation is dominant where the nucleation starts at a defect point or at an impurity. The homogeneous nucleation is observed at larger supercooling than the heterogenous nucleation. The large supercooling is necessary in homogeneous nucleation because the intrinsic barrier to form a nuclei in the homogeneous nucleation is larger than in the heterogeneous nucleation. Homogeneous nucleation was studied by Massa et al. in PEO droplets, where they found that decreasing the size of the droplet the crystallization is observed at higher supercooling or at low crystallization temperatures [79, 80]. The decreasing crystallization temperature, compared to the bulk T_{cry}, with increasing confinement for the P(VDF-TrFE) nanostructures show that the nucleation mechanism is homogeneous. The homogeneous nucleation mechanism inside the alumina nanopores also show that the alumina substrate does not act as a heterogeneous nucleation site.

6.2 Cooling Rate Dependence of the Phase Transitions

Effects of annealing at various temperatures on the T_C and T_m have been extensively studied. It was observed that the T_C and T_m changes depending on whether the annealing is done in ferroelectric phase, in the paraelectric phase or near the melting temperature [29–32]. We have studied the effect of cooling rate on the T_C and T_m of the bulk P(VDF-TrFE) and the nanos-

tructures. By decreasing the cooling rate the sample is effectively annealed longer in the paraelectric phase. Cooling rate of 1 K/min to 40 K/min was used and afterwards the sample was heated with a heating rate of 20 K/min to study the dependence of cooling on the T_C and T_m.

Figure 6.3 shows the DSC heating scans of bulk P(VDF-TrFE), heating rate 20 K/min, after cooling with different rates. The peak Curie temperature and the peak melting temperature from the heating scans is plotted in figure 6.4. The plot clearly shows that as the cooling rate is increased, which means reduction in effective annealing time in the paraelectric phase, the melting temperature is decreased while the Curie temperature increases.

The effect of annealing on the Curie temperature and melting temperature can be again explained by Gibbs free energy, shown in figure 6.5. The figure shows free energy versus temperature for ferroelectric, paraelectric and melt phases. Slow cooling leads to effective annealing in the paraelectric phase which lowers the Gibbs free energy and the paraelectric line goes down resulting in lower Curie temperature (T_C) and increase in melting temperature (T_m). Similarly annealing in the ferroelectric phase can lower the free energy of the ferroelectric phase thereby increasing the Curie temperature [29, 30].
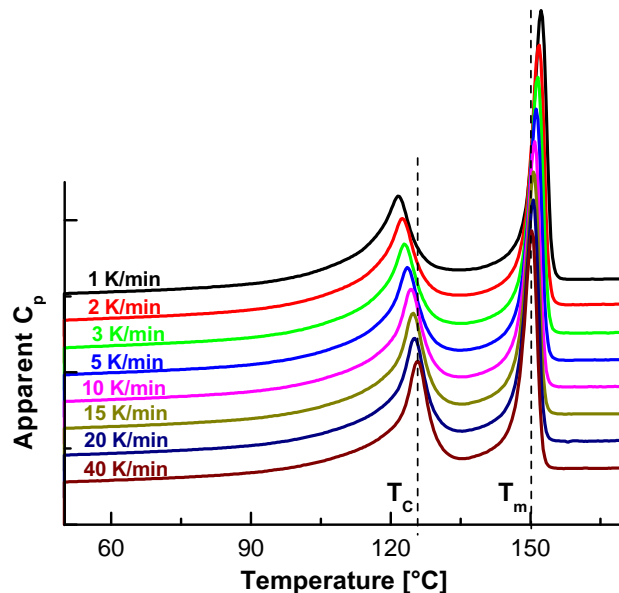

Figure 6.3: DSC heating scans (20 K/min)after cooling with different rates for bulk P(VDF-TrFE). The cooling rate is shown on the corresponding heating scan.
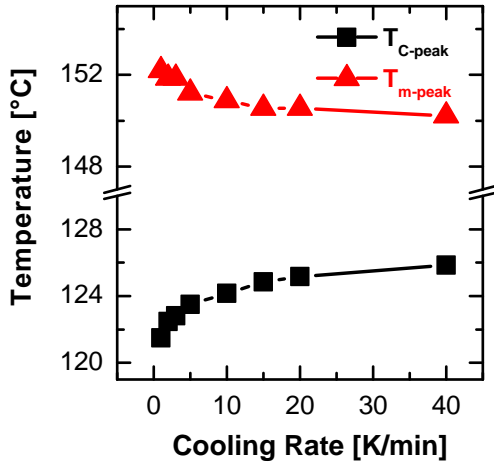
Figure 6.4: Curie temperature and melting temperature dependence on cooling rate for bulk P(VDF-TrFE).

Faster cooling rate results into shorter time for crystallization and annealing in the paraelectric phase, resulting into lower melting temperature and increase in the Curie temperature. Figure 6.6 and 6.7 shows heating scans for 400 nm and 180 nm samples, respectively. Figures 6.8 a-b shows the peak T_C and peak T_m versus temperature for 400 nm and 180 nm nanostructures. The Curie temperature and melting temperature show similar cooling rate dependence for bulk P(VDF-TrFE), 400 nm and 180 nm nanostructure samples. In all the DSC measurements the peak temperatures were measured instead of the onset temperatures because for the nanostructures samples it was difficult to distinguish the onset temperature reliably.

The 60 nm and 35 nm nanotubes shows different behavior after the heat treatment. We presume that both the nanostructures show tube morphology, cf. chapter 5. Figure 6.9 shows the DSC heating scans of the 60 nm
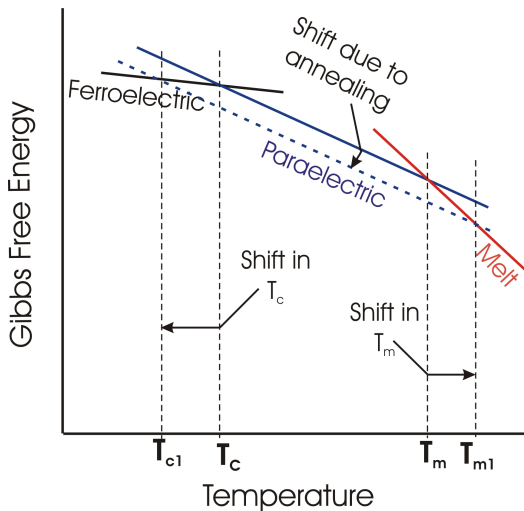
Figure 6.5: Free energy diagram of the ferroelectric, paraelectric and melt phases of P(VDF-TrFE), the dashed line show the shift due to annealing in the paraelectric phase

Figure 6.6: DSC heating scans (20 K/min) after cooling with different rates for P(VDF-TrFE) 400 nm nanotubes, sample: cP_{400}-200-10m. The cooling rate is shown on the corresponding heating scan.
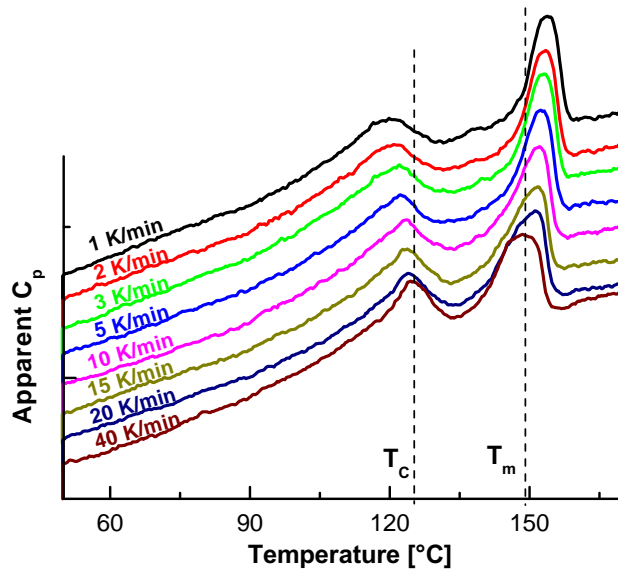
Figure 6.7: DSC heating scans (20 K/min)after cooling with different rates for P(VDF-TrFE) 180 nm nanotubes, sample: cP_{180}-200-10m. The cooling rate is shown on the corresponding heating scan.
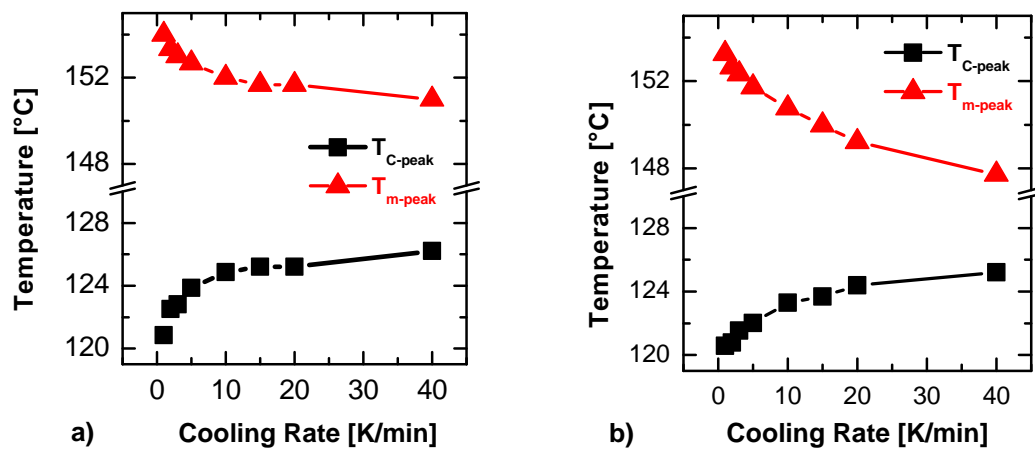
Figure 6.8: Curie temperature and melting temperature versus scan rate for a) 400 nm nanostructures, sample: cP_{400}-200-10m and b) 180 nm nanostructures, sample: cP_{180}-200-10m
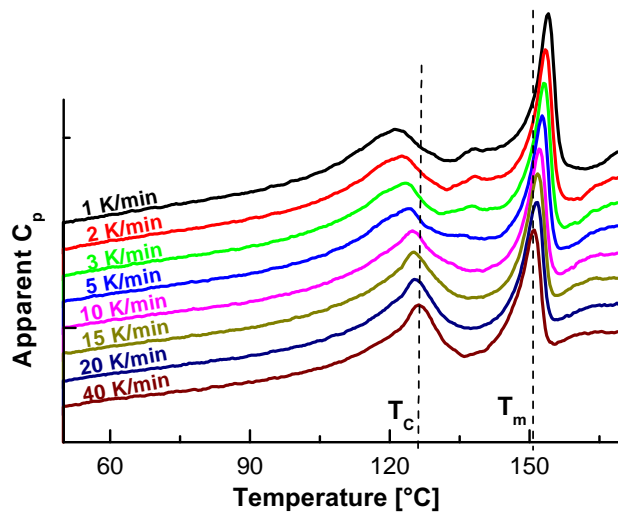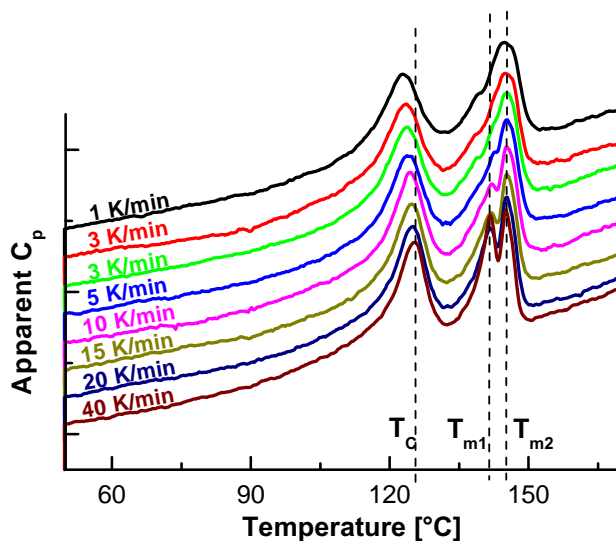

Figure 6.9: DSC heating scans (20 K/min)after cooling with different rates for P(VDF-TrFE) 60 nm nanotubes, sample: cP_{60}-200-10m. The cooling rate is shown on the corresponding heating scan.

nanostructures. The Curie temperature decreases with decreasing the scan rate but the decrease is very low compared to bulk P(VDF-TrFE) or the 400 nm and 180 nm nanostructures. The melting temperature shows a quite different behavior. At high scan rate there are two melting peaks and as

77

Figure 6.10: DSC heating scans (20 K/min)after cooling with different rates for PVDF-TrFE 35 nm nanotubes, sample: cP_{35}-200-10m. The cooling rate is shown on the corresponding heating scan.

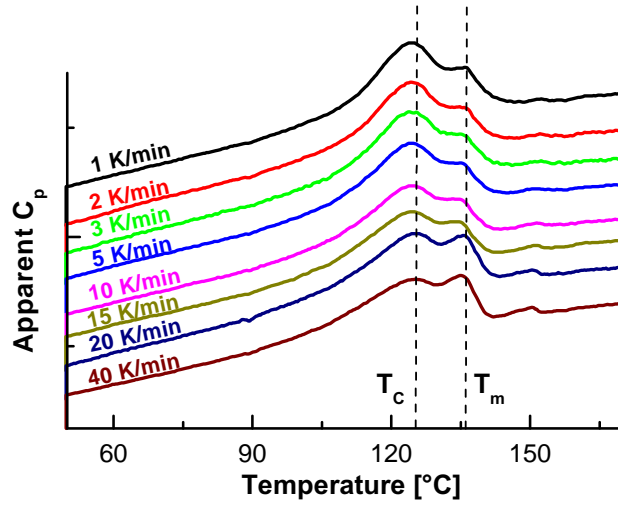the scan rate is decreased the peak on the lower temperature side reduces in intensity and finally disappears, leaving a small shoulder on the melting peak at high temperature. The two melting peaks in the 60 nm nanostructures could have resulted from crystallization kinetics inside the nanopores. Under the conditions where the crystallization is dominated by nucleation, in case of high cooling rate, some of the crystallites might have unfavorable orientation and impinge on the pore walls, these small crystallites show the low T_m. Other crystallites might have grown with crystal faces oriented normal to the pore axis, it will have high lamellae thickness and larger T_m. When the cooling rate is decreased the nucleation events are decreased and the crystallization is dominated by crystal growth having the c-axis preferentially oriented perpendicular to the pore axis. This results into only one melting temperature. The T_m (from the second peak at hight temperature) and T_C of 60 nm nanostructures is plotted in figure 6.11 a. Where it is evident that the T_m is constant and also there is only slight change in T_C.

For the 35 nm nanotubes, the T_m and T_C does not show any change for different cooling rates, figure 6.10. The T_m is not increasing because the strong confinement in the 35 nm nanotubes does not allow any further thickening of the crystallites. Figure 6.11 b shows the scan rate versus peak Curie temperature and peak melting temperature. Due to small intensity of the melting peak it is difficult to measure the exact peak position (the peak
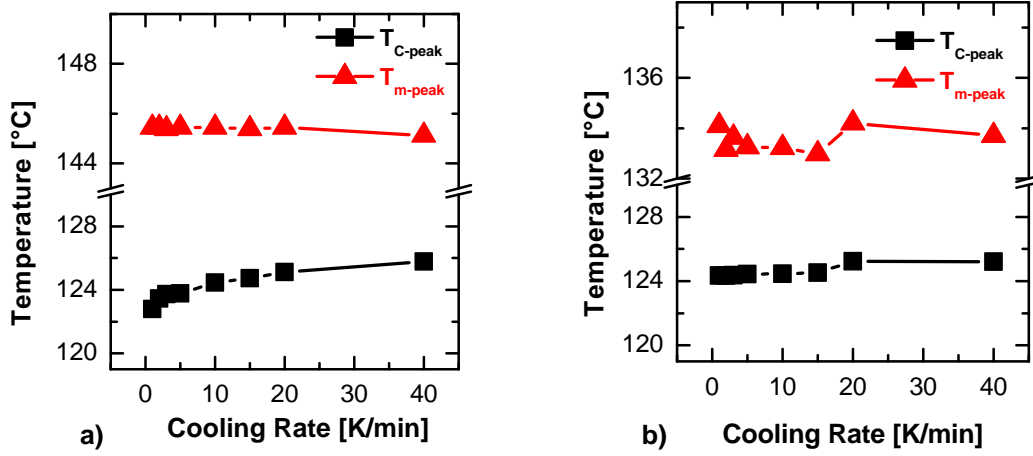
78

Figure 6.11: Curie temperature and melting temperature versus scan rate for a) 60 nm nanostructures, sample: cP_{60}-200-10m, the T_m at the larger temperature is shown and b) 35 nm nanostructures, sample: cP_{35}-200-10m

positions were determined by Gauss fit) which results into scattering of the data points in the figure 6.11 b. Therefore the DSC scans in figure 6.10 is better way to represent the data from 35 nm nanostructures. Where the T_m does not show any change as well the T_C is almost constant with decrease in cooling rate. Due to the high confinement the lamellae thickness is restricted and the restriction in the lamellae thickness also affect the T_C. This shows that the Curie temperature is dependent on the lamellae thickness. Increase in the T_m, that is increase in the lamellae thickness, results into lowering of the T_C. It is possible for the lamellae thickness to increase in case of bulk P(VDF-TrFE), 400 nm and 180 nm nanostructures and therefore the T_C is also able to change. In case of the 35 nm nanostructures the lamellae thickness is restricted therefore the T_C is also not able to change.

6.3   Summary

The DSC results show that with increasing the confinement the melting temperature decreases which means that the crystal size decreases with increase in the confinement. The Curie temperature does not show any change by increase in the confinement which could be explained by shift in Gibb's free energy in the ferroelectric and paraelectric phase in the confined nanostructures. The decrease in the crystallization temperature in the confinement shows that the crystallization starts with homogeneous nucleation and the alumina template wall does not act as heterogeneous nucleation sites.

79

The decrease in the cooling rate, that is effective annealing in the para-electric phase, leads to increase in T_m and decrease in the T_C. This is related to decrease in the Gibbs free energy due to effective annealing in the paraelectric phase by slow cooling. The change in T_C and T_m, with change in cooling rate, was observed for bulk P(VDF-TrFE), 400 nm and 180 nm nanostructures. The 60 nm and 35 nm nanostructures showed different behavior. The 60 nm nanostructures showed two melting temperatures and slight change in T_C. For the 35 nm nanostructures T_C and T_m remains constant for different cooling rates. The melting temperature does not change for 35 nm nanostructures because the high confinement provided by the 35 nm nanopores does not allow the lamella to thicken. The constant T_C then suggest that the Curie temperature is intrinsically linked to the lamellae thickness.

Chapter 7

Crystal Texture in P(VDF-TrFE) Nanostructures

As discussed in chapter 2, the ferroelectric properties of P(VDF-TrFE) are the result of dipole moment between the fluorine and carbon atoms. Prerequisite for practical applications of the ferroelectric polymers is that the dipoles should have preferred orientation. Therefore the functionality of the ferroelectric nanostructures is dependent on the crystal orientation. In this chapter, we will see how the crystal orientation of P(VDF-TrFE) is dependent on the morphology and crystallization conditions. The crystal orientation of the P(VDF-TrFE) nanostructures was studied by x-ray diffraction. All the x-ray diffraction measurements, except the temperature dependent XRD, were carried out on a Phillips X'Pert diffractometer in reflection mode. $CuK\alpha$ radiation with wavelength of 1.5405 $\mathring{A}$ was used. For $\theta - 2\theta$ measurements step size of 0.02° with integration time, at each step, of 5 to 10 seconds was used. For the ψ-scans, step size of 0.2° with integration time of 25 seconds was used. The $\theta - 2\theta$ pattern was measured by opening the incoming beam slit width, d, by 2 mm and for ψ-scans the slit width was reduced to 0.5 mm. The importance of the reduction of the slit width for ψ-scans is discussed in chapter 4.

The nanostructure samples were prepared under different crystallization conditions and also different diameters of AAO nanopores were used. In this chapter the sample names are used for which the detail preparation conditions and morphology, as inferred from SEM and TEM analysis, is given in the appendix-I.

The $\theta - 2\theta$ pattern for bulk P(VDF-TrFE), measured at room temperature, is shown in figure 7.1. The $\theta - 2\theta$ pattern show six Bragg's peaks. The peaks are indexed by considering an orthorhombic unit cell with lattice parameters of $a = 9\,\mathring{A}$, $b = 5.16\,\mathring{A}$ and $c = 2.55\,\mathring{A}$, for 70/30 mol% P(VDF-

81
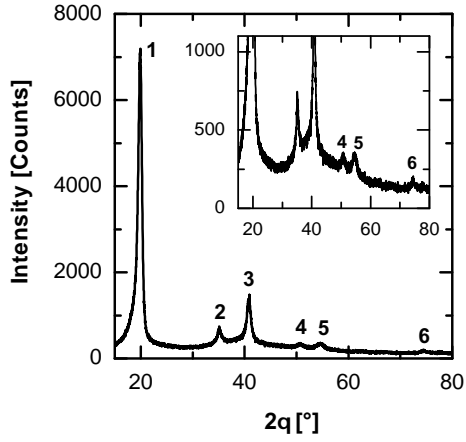
Figure 7.1: Bulk P(VDF-TrFE) XRD pattern

	Angle (2θ)	Index
Peak - 1	19.9°	(110/200)
Peak - 2	35.1°	(310/020)(001)
Peak - 3	40.8°	(400/220)(111/201)
Peak - 4	50.5°	(311/021)
Peak - 5	54.5°	(510/420/130)(401/221)
Peak - 6	74.4°	(140)(331/521/002)

Table 7.1: Index of peaks in $\theta - 2\theta$ pattern (figure 7.1) for bulk P(VDF-TrFE)

TrFE) [34]. Table 7.1 shows the lattice indices for the peaks in $\theta - 2\theta$ pattern of P(VDF-TrFE).

As discussed in the chapter 2, at room temperature P(VDF-TrFE) is in ferroelectric phase having pseudo-hexagonal crystal symmetry therefore two or more Bragg's reflections are observed at the same 2θ angle.

7.1 Phase Transition in Bulk and in the 400 nm Nanotubes

P(VDF-TrFE) shows two phase transitions each during cooling and heating as seen by the DSC measurements in chapter 6. The structural changes taking place during these transitions can be followed by temperature dependent x-ray diffraction (XRD) measurements. For the bulk P(VDF-TrFE) of various VDF and TrFE contents, the phase transitions followed by XRD is already reported by various authors [31, 34, 36, 40]. The crystal lattice of P(VDF-TrFE) in paraelectric phase and ferroelectric phase is shown in
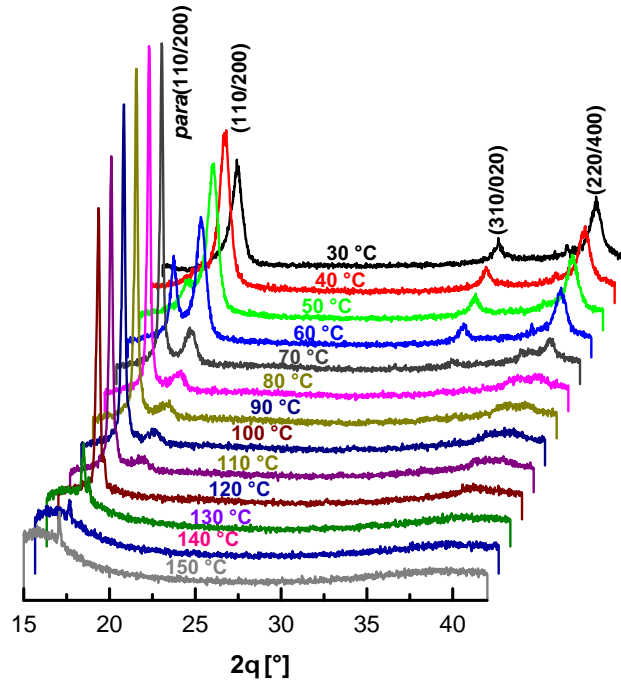
Figure 7.2: $\theta - 2\theta$ patterns during cooling for bulk P(VDF-TrFE)

chapter 2. An orthorhombic unit cell was considered for both in paraelectric as well as in the ferroelectric phase. To distinguish (110/200) peak in the paraelectric phase and in the ferroelectric phase, the peak is designated as $para$(110/200) in the paraelectric phase and (110/200) in the ferroelectric phase. Temperature dependent XRD measurements were performed during heating and cooling to follow the structural changes in the bulk P(VDF-TrFE) and in the 400 nm nanostructures. The temperature dependent WAXS measurements were carried out on a Siemens D5000 with a Germanium monochromator with $CuK\alpha$ radiation of 1.5405 Å. Measurements were done in reflection mode with 0.02° step size and integration time of 10 seconds. Only the cooling measurements are shown here because they are important for the understanding of crystallization and paraelectric to ferroelectric phase transition (para- to ferro- transition) in the nanostructures.

Figure 7.2 shows the temperature dependent $\theta - 2\theta$ patterns of the bulk P(VDF-TrFE). At a temperature of 150°C the 2θ pattern shows a small peak corresponding to $para$(110/200) at $2\theta = 17.1°$ in the hexagonal phase. It is possible that at 150°C all the crystallites are not melted. The peak melting temperature measured by the DSC for P(VDF-TrFE) was 151°C. In the XRD pattern at 150°C the P(VDF-TrFE) crystallites are not entirely melted

83

and the peak corresponding to the hexagonal phase is observed, which is also the onset of crystallization during the cooling. From the DSC measurements, in chapter 6, the onset of crystallization was observed at $137°C$. The difference in the transition temperatures observed by DSC and XRD could have resulted from the poor thermal contact between the sample and the heater in the XRD compared to DSC where the sample is very thin. Also, the sample in the DSC is cooled with a cooling rate of 20 K/min while in the XRD the temperature was decreased step-wise, by atmospheric cooling. This could result into temperature difference measured by DSC and XRD.

As the temperature decreases to $100°C$, another peak starts to appear at $2\theta = 19.9°$ corresponding to (110/200) in the ferroelectric phase. The paraelectric to ferroelectric phase transition in the DSC, in chapter 6, was observed at $80°C$. With decreasing temperature, intensity of (110/200) peak continues to increase with simultaneous decrease in the intensity of the $para$(110/200) peak, also the (310/020) and (220/400) peaks starts to appear. The paraelectric to ferroelectric phase transition is completed at $40°C$. In the paraelectric phase the $para$(110/200) show sharp peaks compared to the (110/200) peak in the ferroelectric phase. This reflects the large crystal domain size in the paraelectric phase. During the phase transition from paraelectric to ferroelectric phase the larger paraelectric domains are divided into smaller ferroelectric domains [31]. Also, in the ferroelectric phase, the hexagonal symmetry is lost and there is a slight difference in the interplanar spacing between the (110) and (200) planes. Therefore, the (110) and (200) reflections are observed at slightly different 2θ angles which increases the width of (110/200) reflection.

The XRD data also shows higher onset temperature than the DSC for the para- to ferro- transition. It is possible that there is a large difference of temperature for the sample surface in contact with the heater and the sample surface in contact with the air. The bulk sample was 2 mm thick and it is possible that when the heater temperature is showing $100°C$, the actual temperature in contact with the air is lower. Therefore the phase transition occurred at the sample surface is registered at a higher temperature.

The scattering data for bulk P(VDF-TrFE), shown in figure 7.2, does not show any higher order peaks in the high temperature paraelectric phase. It could be related to the decrease in the peak intensity at high temperature which is given by the *Debye-Waller* factor. In order to take into account the thermal effects, the theoretical intensity of a given peak is multiplied by the Debye-Waller factor, D, which is less than unity. The Debye-Waller factor is related to the thermal vibrations in the atoms which increase in amplitude by increasing the temperature. The thermal agitations leads to general background scattering and intensity of selective reflections is decreased [81]. The
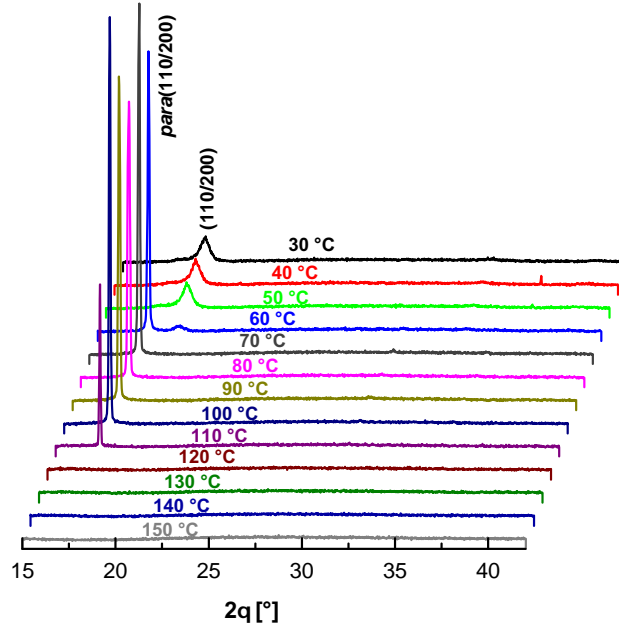
Figure 7.3: $\theta - 2\theta$ patterns during cooling for PVDF-TrFE 400 nanotubes, sample $cP_{400} - 200 - 10m$

Deby-Waller factor is given by the equation,

$$D = exp\left(-\frac{16\pi^2 sin^2\theta}{\lambda^2}\frac{\Delta X^2}{3}\right) \tag{7.1}$$

where, θ is the scattering angle, λ is the wavelength of x-ray and ΔX is the average displacement of atoms from its node. The Debye-Waller factor show that by increasing the temperature and increasing the scattering angle, θ, could lead to decrease in D, and therefore decrease in the scattering intensity [81]. In case of P(VDF-TrFE) in the paraelectric phase the chains are highly mobile and are in constant motion, therefore the higher order peaks are not observed.

Figure 7.3 shows the temperature dependent WAXS measurements of the 400 nm P(VDF-TrFE) nanostructures, sample $cP_{400} - 200 - 10m$. The morphology of these 400 nm nanostructures was found to be tubes as discussed in the chapter 5. Cooling from $150°C$ the first peak corresponding to the $para(110/200)$ can be observed at $110°C$ which corresponds to the crystallization of P(VDF-TrFE) inside the nanopores. For the bulk the crystallization onset was observed at $150°C$ while for the 400 nm nanotubes it is observed at $110°C$. The decrease in the crystallization temperature in the
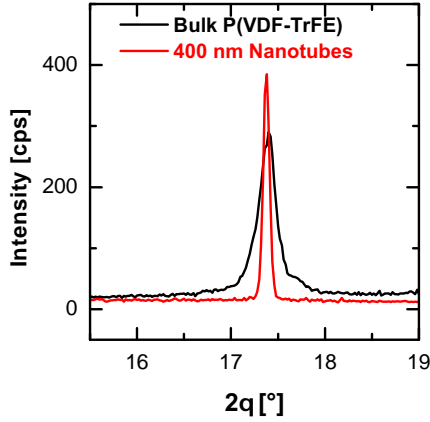
Figure 7.4: The *para*(110/200) XRD peak in the paraelectric phase for bulk and 400 nm nanotubes at 110 °C

400 nm sample shows that the crystallization takes place by homogeneous nucleation mechanism. Also, the thermal contact between the heater and the sample is better for the nanotubes than in the bulk P(VDF-TrFE) sample therefore some temperature difference is expected between the two samples. Cooling further to $60°C$, a small peak corresponding to (110/200) related to ferroelectric phase is observed. It is the onset of paraelectric to ferroelectric phase transition. At $50°C$ only the peak corresponding to the ferroelectric phase is observed. In stark contrast to the bulk, in the ferroelectric phase, the (310/020) and (220/400) reflections are disappeared in the nanostructures.

For the 400 nm sample, the DSC showed the crystallization onset temperature at $136°C$ and the para- to ferro- phase transition at $110°C$. From the XRD, the onset of crystallization is observed at $110°C$ and para- to ferro-transition at $60°C$. The difference between the temperature by the DSC and XRD is $26°C$ and $20°C$ for the crystallization and para- to ferro- phase transition, respectively. The 400 nm sample is only 100 μm thick embedded in alumina with a aluminium base, therefore the thermal contact in this sample will be better than in the bulk sample. Still the better thermal contact as well as better temperature calibration in DSC as compared to the XRD temperature controller will lead to some difference in the measured temperature.

Comparison between the temperature dependent cooling measurements for bulk and 400 nm nanotubes reveal some important differences. The major difference being the absence of the (310/020) and (220/400) peaks in the ferroelectric phase for the 400 nm nanotubes sample. The reason for the absence of the two peaks will be discussed in next section. The second difference is that the para- to ferro- phase transition is observed on wide temperature range for the bulk sample than in the 400 nm nanotubes. This wide temperature range for the transition in the bulk could be the result of large number of crystals having different crystal sizes in the bulk P(VDF-
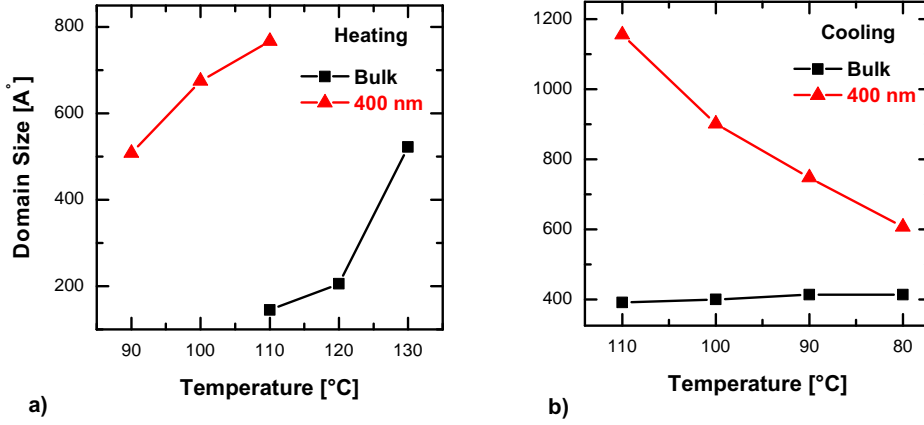
86

Figure 7.5: Size of *para*(110/200) domain for bulk P(VDF-TrFE) and 400 nm nanotubes in paraelectric phase, a) during heating and b) during cooling

TrFE) than in the 400 nm nanotubes. It is possible that the growth of lamellae in the 400 nm nanotubes is more uniform than in the bulk sample which leads to sharp ferro- to para- transition in the 400 nm nanotubes. The ferro- to para- transition temperature, T_C, depend on the crystal sizes which was shown by DSC measurements in chapter 6. Another big difference in the bulk and 400 nm nanotubes sample is the width of the *para*(110/200) peak in the paraelectric phase. Figure 7.4 show the *para*(110/200) peaks measured at 110°C for the bulk and 400 nm nanotubes sample. It can be seen that the 400 nm nanotubes sample show very narrow peak compared to the bulk sample. It shows that in the nanotubes the *para*(110/200) crystal domains are considerably larger than in the bulk P(VDF-TrFE). The size of the crystal domains can be calculated by the Scherrer equation, given as

$$\Delta 2\theta = \frac{\lambda}{L cos\theta} \tag{7.2}$$

where, $\Delta 2\theta$ is the full width of half maximum of the diffraction peak, L is the crystal size, λ is the wavelength of the x-rays and θ is the diffraction angle [81].

The crystal domain size is calculated both during heating and cooling. The temperature dependence of the *para*(110/200) crystal domains for bulk and 400 nm nanotubes is shown in figure 7.5. The result show that, after crystallization, in the paraelectric phase the crystal domains in 400 nm nanotubes are considerably larger than in the bulk P(VDF-TrFE). Which means that there are large number of (110/200) planes that are parallel to the template surface in the paraelectric phase and it gives an indication that the

c-axis is perpendicular to the long axis of the nanopores. It is also supported by the $\theta - 2\theta$ pattern and ψ-scan measurements which does not show any contribution from the (hkl) planes having non-zero l-index in the nanotubes. In previous studies it was already shown that in two-dimensional (2D) confinement the c-axis is preferentially oriented parallel to the template surface. It was argued that in case of non parallel orientation of the c-axis with the template surface, the crystals will impinge on the nanopore wall and the crystal growth will stop. Crystals only with c-axis parallel to the template surface can grow in the 2D confinement, therefore the growth kinetics of the crystals are responsible for the preferred orientation of the c-axis parallel to the template surface [10]. This was confirmed by many other studies in the 2D confinement [11, 25, 26, 82].

7.2   Orientation in Confinement

To study the orientation of the nanostructures in the ferroelectric phase, $\theta - 2\theta$ patterns as well as the ψ-scans were performed in the Phillips X'Pert x-ray diffractometer. All the x-ray diffraction measurements were carried out at room temperature. To study the crystal orientation and the effects of crystallization kinetics on the orientation, slowly cooled and quenched samples were analyzed.

7.2.1   Slowly cooled nanostructures

Figure 7.6 shows the $\theta - 2\theta$ pattern of 400 nm nanotubes sample. The sample, $cP_{400} - 200 - 10m$, was wetted at $200°C$ for 10 minutes and cooled to $30°C$ with a cooling rate of 1 K/min. This sample showed tube morphology from the TEM and SEM analysis, cf. chapter 5.2. The $\theta - 2\theta$ pattern shows only (110/200) peak, and compared to bulk pattern in figure 7.1, the other two peaks corresponding to (310/020) and (220/400) planes are missing. The missing (310/020) reflection suggest orientation in the $cP_{400} - 200 - 10m$ sample because the x-ray geometry is sensitive to the planes oriented parallel to the template surface. The absence of the (220/400) reflection is also an indication of orientation described, in more detail, in section 7.4.

To study the orientation of P(VDF-TrFE) crystallites inside the nanopores, ψ-scans were performed. Figure 7.7 shows the ψ-scans for the isotropic bulk P(VDF-TrFE) and 400 nm nanotubes, $cP_{400} - 200 - 10m$, sample. In the bulk sample the ψ-scan corresponding to (110/200) planes, in figure 7.7 a, shows constant intensity until $\psi = 30°$ and then the intensity starts to fall down due to the defocusing effects as described in chapter 4. For the nan-

otube sample, $cP_{400} - 200 - 10m$, the ψ-scan of (110/200) shows a rapid fall in intensity from $\psi = 0°$. This clearly shows that the (110/200) planes are preferentially oriented parallel to the template surface. The width of the ψ-scan is quite large, this is due to the fact that the ψ-scan is composed of two reflections, (110) and (200), which are oriented 60° to each other. Therefore two peaks at $\psi = 0°$ and at $\psi = 60°$ are expected in the ψ-scan. In the (110/200) ψ-scan of the nanotubes, figure 7.7 b, there is a peak at $\psi = 0°$ and a small bump at $\psi = 60°$. The peak at 60° is not distinctive for the reason, as discussed in chapter 4, is that due to the defocusing effects the
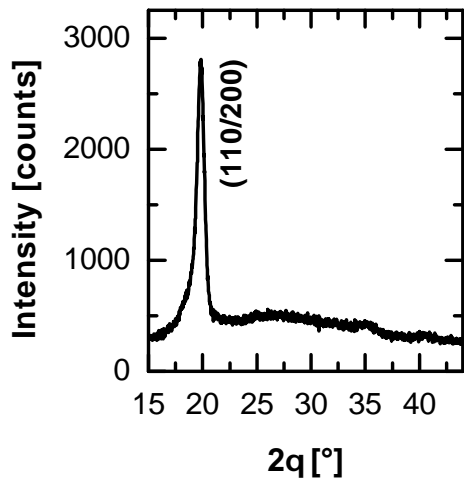

Figure 7.6: XRD $\theta - 2\theta$ pattern of P(VDF-TrFE) 400 nm nanotubes, wetting at 200 °C for 10 minutes and cooled with 1 K/min, sample: $cP_{400} - 200 - 10m$
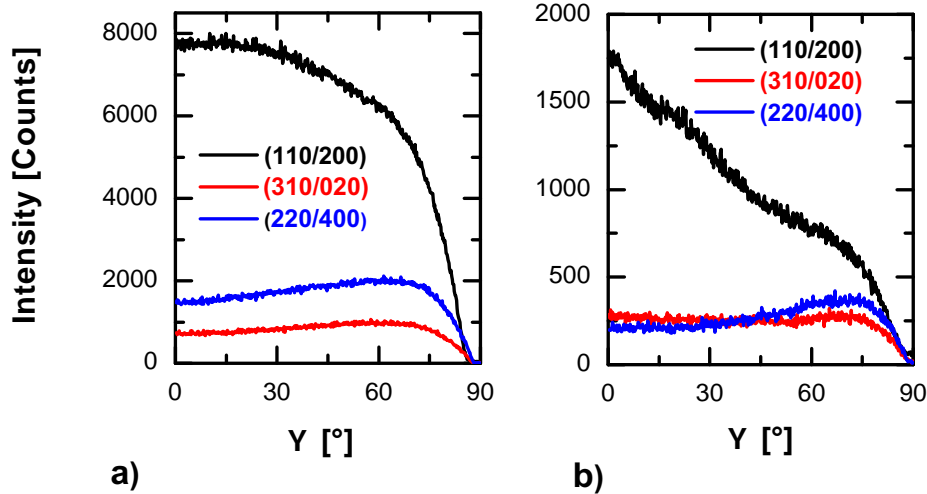

a)

b)

Figure 7.7: ψ-scans of a) bulk P(VDF-TrFE) and b) 400 nm nanotubes sample $cP_{400} - 200 - 10m$

intensity of ψ-scan goes down above $\psi = 47°$ even for an isotropic sample. Those two peaks lead to large width in the ψ-scan of (110/200) planes which appears as a broad distribution.

The ψ-scan of (220/400) of $cP_{400} - 200 - 10m$ sample show minimum intensity at $\psi = 0°$ and has a maximum intensity at $\psi = 60°$, while in the bulk sample the ψ-scan of (220/400) remains almost constant. The increase in intensity at $\psi = 60°$ in the 400 nm nanotubes sample is related to the preferred orientation of the (110) planes parallel to the template surface which will be discussed in section 7.4. The ψ-scan of (310/020) for the nanotubes show constant intensity, which suggest no preferred orientation for (310/020) planes inside the nanostructures. For the bulk P(VDF-TrFE), the ψ-scan of (310/020) show increasing intensity from $\psi = 0°$, the reason for the increase is not clear.

Comparison of the ψ-scans for the bulk and $cP_{400} - 200 - 10m$ show that in the 400 nm nanotubes there is a preferred orientation of the (110/200) planes parallel to the template surface. The preferred orientation could be the result of kinetic selection of the crystal growth. Crystals will grow such that there growth direction coincides with minimum curvature in the nanopores [83]. It could be possible that restricting the crystal growth by quenching the sample, could lead to destruction of the orientation as the crystallization becomes more nucleation dominated than the crystal growth. To check this hypothesis, sample were quenched instead of cooling after the wetting of P(VDF-TrFE).

7.2.2   Quenched nanostructures

The quench sample, $qP_{400} - 200 - 10m$, was prepared by wetting the 400 nm nanopores at $200°C$ for 10 minutes and then removing it from the furnace to the room temperature (around 25°C). The free standing nanostructures from this sample showed tube morphology, cf. chapter 5.2. Figure 7.8 shows the $\theta - 2\theta$ pattern and ψ-scans of the quench sample, $qP_{400} - 200 - 10m$. The $\theta - 2\theta$ is similar to the slowly cooled sample apart from a small peak at $2\theta = 35.1°$ corresponding to (310/020). The ψ-scans in figure 7.8 b shows almost constant intensity for the (110/200) planes, like the isotropic bulk sample, until $\psi = 30°$ and then it starts reducing with a slight bump at 60°. This shows that the quenched sample does not show orientation. The ψ-scan of (310/020) is constant while the (220/400) scan show slight increase in intensity at around 60°.

The difference between the slowly cooled and quenched sample show that the preferential orientation of (110/200) planes, inside the slowly cooled sample is the result of kinetic selection of growth rate rather than the epitaxial
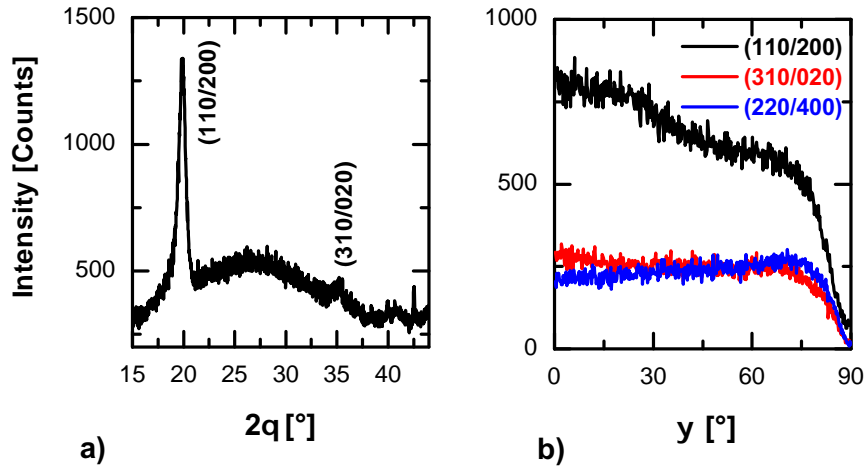
Figure 7.8: PVDF-TrFE 400 nm nanotubes, wetting temperature 200 °C for 10 minutes and quenched in open atmosphere, sample $qP_{400} - 200 - 10m$. a) $\theta - 2\theta$ scan and b) ψ-scans

growth on high energy surface of alumina. By quenching the sample, the crystallization is dominated by nucleation rather than crystal growth. The large number of nuclei lead to formation of many crystallites with random orientation.

7.2.3 Effect of Surface Film on Orientation

In case of PVDF in 2D confinement it was found that the crystal orientation changes depending on the presence or absence of the bulk surface film on the template surface [10]. It was argued that in presence of the surface film, the crystallization in the 2D confinement takes place with heterogeneous nucleation in the surface film and crystals orients with preferred (020) planes parallel to the template surface. In the absence of the surface film, the crystallization takes place with homogeneous nucleation mechanism and the preferred orientation is lost. To study the effect of surface film on orientation of P(VDF-TrFE) crystallites in the nanopores, samples were prepared that were crystallized with surface film (interconnected nanostructures) and without surface film (separated nanostructures). The 60 nm nanostructures, $cP_{60} - 200 - 10m$, were prepared at a wetting temperature of $200°C$ for 10 minutes and cooled to $30°C$ with a cooling rate of 1 K/min. One of the sample was crystallized with the bulk surface film and another sample was crystallized without the surface film, the XRD results are shown in figures 7.9
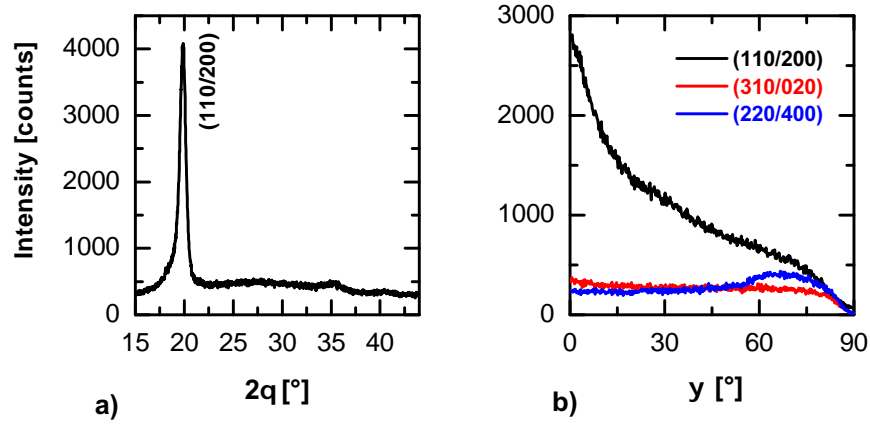
Figure 7.9: P(VDF-TrFE) 60 nm nanostructures prepared by wetting at 200°C for 10 minutes, sample $cP_{60}-200-10m$, crystallized *with surface film* with a cooling rate of 1 K/min, a) $\theta-2\theta$ pattern and b) ψ-scans)
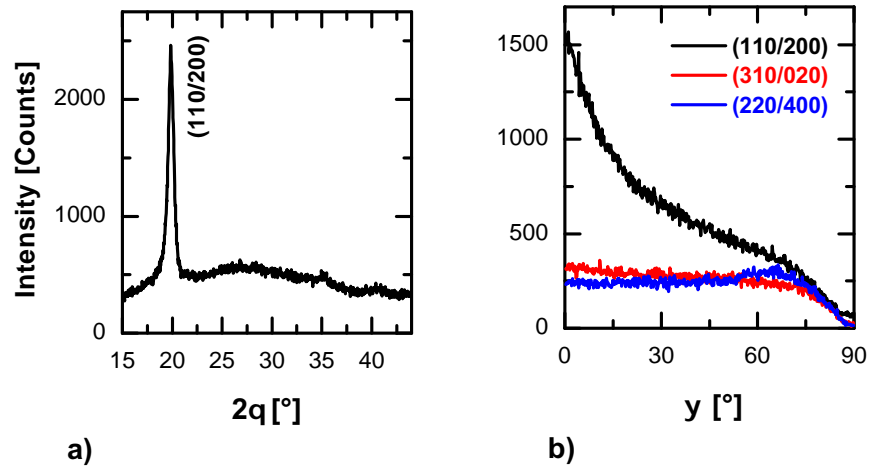
Figure 7.10: P(VDF-TrFE) 60 nm nanostructures prepared by wetting at 200°C for 10 minutes, sample $cP_{60}-200-10m$, crystallized *without surface film* with a cooling rate of 1 K/min, a) $\theta-2\theta$ pattern and b) ψ-scans

and 7.10, respectively. Both the samples show the same $\theta-2\theta$ pattern as well the ψ-scans are also identical. Therefore the results show that there is no change in the crystal orientation of the P(VDF-TrFE) nanostructures in the presence or absence of the surface film.

Unlike PVDF the P(VDF-TrFE) nanostructures show no change in orien-

tation in the presence or absence of the surface film. It is because crystallization in P(VDF-TrFE) takes place in the hexagonal phase and the crystal can grow in six equivalent directions. While as in the PVDF it was observed that the highest growth rate occur in the [020] direction which results in (020) planes parallel to the template surface, no such preferred growth direction exists in P(VDF-TrFE) during the crystallization in paraelectric phase. For this reason only samples crystallized with surface film were analyzed.

7.2.4 Background contribution of alumina to the diffraction peaks

We have seen that in $\theta - 2\theta$ pattern of nanostructures the peaks at $2\theta = 35.1°$ and at $2\theta = 40.8°$ are missing. Before analyzing further results it should be clear that the peaks are missing due to orientation and not due to the background contribution from the amorphous alumina. As the nanostructures sample is consist of P(VDF-TrFE) and alumina. To rule out the possibility that the two absent peaks in the nanostructure sample is not due to the background contribution of alumina, here, the peak intensities in $\theta - 2\theta$ pattern of bulk P(VDF-TrFE) and 400 nm nanotubes is considered. Figure 7.11 shows the $\theta - 2\theta$ pattern of bulk P(VDF-TrFE), 400 nm nanotubes $(cP_{400} - 200 - 10m)$ and amorphous halo from porous alumina of 25 nm diameter. The background is subtracted from all the samples. The expected diffraction peaks of P(VDF-TrFE) are represented by red dashed line in the $\theta - 2\theta$ pattern of porous alumina, figure 7.11 c. From the amorphous halo of the alumina it is clear that the maximum contribution for background scat-
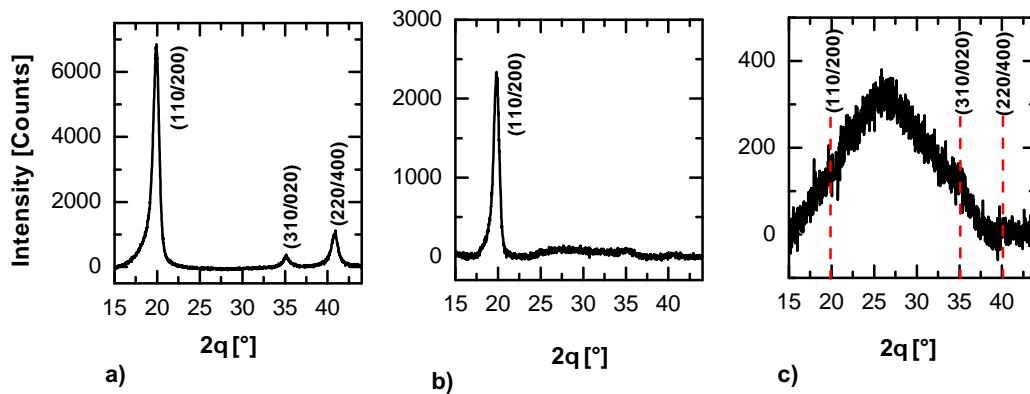

Figure 7.11: $\theta - 2\theta$ pattern of a) bulk P(VDF-TrFE), b) 400 nm nanotubes, $cP_{60} - 200 - 10m$ and c) 25 nm AAO template

93

	Intensity Ratio (110/200)/(310/020)	Intensity Ratio (110/200)/(220/400)
bulk P(VDF-TrFE)	18	6
400 nm nanotubes	31	90

Table 7.2: The ratio of (110/200) peak intensity to the peak intensity of (310/020) and (220/400) for bulk P(VDF-TrFE) and 400 nm nanotubes samples

tering will be at $2\theta = 19.8°$ and at $2\theta = 35.1°$ corresponding to (110/200) and (310/020), respectively. The (220/400) reflection at $2\theta = 40.8°$ have the minimum background contribution from the porous alumina.

In order to see that the (310/020) and (220/400) peaks are not suppressed by the amorphous halo of the porous alumina in the nanotubes sample, the intensity ratios in the $\theta-2\theta$ pattern of bulk P(VDF-TrFE) and the nanotubes can be compared. The ratio of the (110/200) peak to the other two peaks, that is to (310/020) and (220/400), is shown in table 7.11 for both the bulk P(VDF-TrFE) and the 400 nm nanotubes, $cP_{400} - 200 - 10m$. The ratio was calculated by measuring the peak intensities in the $\theta - 2\theta$ pattern of the samples after subtracting the background. For the absent peaks in the 400 nm nanotubes the intensities at their respective 2θ position was measured. The ratio of (110/200) peak to the other two peaks is very high in the 400 nm nanotube sample which indicate that the peaks are absent due to the orientation and not due the background contribution of alumina. In case the alumina background contribution was high then the ration would have been less than in the bulk P(VDF-TrFE) sample.

7.3 Factors Affecting the Orientation

7.3.1 Orientation dependence on wetting time and temperature

As discussed in the chapter 5.1.4, morphology, during the wetting process, over a length of time, simultaneous thickening of the tube walls as well as wetting of the pore wall take place. Further wetting the AAO nanopores for a long period of time instabilities may evolve. Increasing the wetting temperature simply accelerates the various wetting processes. Therefore, there is a continuous evolution of the morphology during the wetting of the nanopores by P(VDF-TrFE), which may reflect in the orientation of the crystallites.

To study the effect of wetting time and temperature on the orientation of the crystallites in the nanostructures, samples were prepared at $200°C$ and $250°C$ with wetting time of 10 minutes and 12 hours, at each temperature. In this section the orientation dependence on the wetting time and temperature is discussed for 400 nm nanotubes. For all the wetting conditions, short and long, the 400 nm nanostructures show the tube morphology, cf. chapter 5.2.

Figure 7.12 shows the $\theta - 2\theta$ pattern and ψ-scan of 400 nm nanotubes, $cP_{400} - 250 - 12h$, prepared at $250°C$ for a wetting time of 12 hours and cooled with 1 K/min to $30°C$. The $\theta - 2\theta$ pattern, figure 7.12 a, shows not only (110/200) peak but also (310/020) and (220/400) peaks. The relative intensity of the (220/400) is still small compared to the (110/200) and (310/020) peaks. Therefore it appears that along with (110/200) parallel to the template surface the (310/020) planes are also oriented parallel to the template surface. It is also clear from the ψ-scans, figure 7.12 b, where the (110/200) as well as the (310/020) show a peak at $\psi = 0°$. With the longer wetting time the wall thickness of the tubes may increase which results in decrease in confinement. Which might be responsible for the appearance of (310/020) planes parallel to the template surface. In the confined geometry of AAO nanopores it is equally possible for (110/200) and (310/020) planes to be parallel with template surface. However, only in the 400 nm samples after 12 hours wetting time shows the presence of the (310/020) peak.

The ψ-scans of (110/200) and slope of the ψ-scan at different wetting conditions for 400 nm nanotubes is shown in figure 7.13. The slopes of the
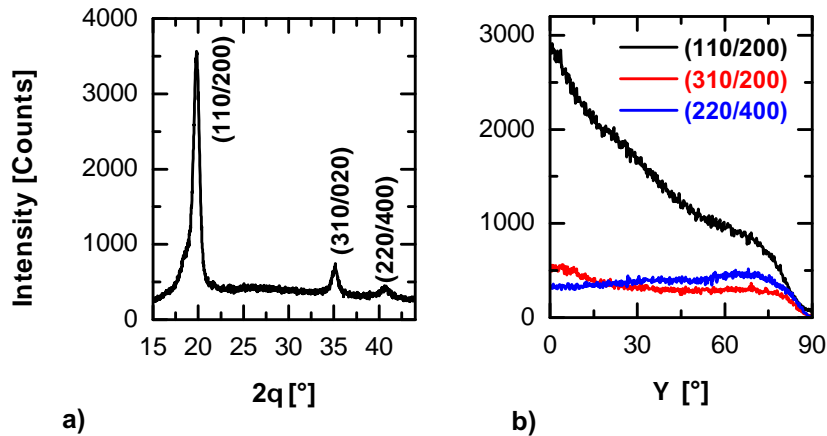

Figure 7.12: XRD results for 400 nm nanotubes wetted at 250 °C for 12 hours and then cooled with 1 K/min to 30 °C, sample $cP_{400} - 250 - 12h$, a) $\theta - 2\theta$ scan and b) ψ-scans
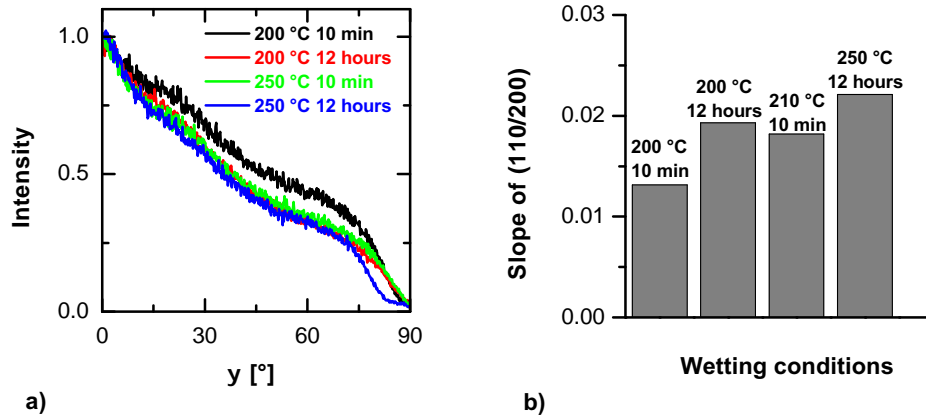
Figure 7.13: Wetting time and temperature dependence for 400 nm nanotubes a) ψ-scans of the (110/200) planes and b) slopes of the (110/200) ψ-scans

ψ-scans were measured between $\psi = 0°$ to $\psi = 15°$. Increasing slope means narrow width of the ψ-scan which signifies better orientation. The slopes of the ψ-scans are negative, for better representation in figure 7.13 b, the slopes are shown with positive values. The slopes of the ψ-scans, shown in the figure 7.13 b, show a minor improvement as the wetting time or temperature is increased. Thickening of the tube wall, due to long wetting time or higher temperature, could lead to better orientation for the (110/200) planes parallel to the template. But the effect on the slope is negligibly small to exclude the experimental variations.

For 60 nm nanostructures, the effect of wetting conditions on orientation of (110/200) planes is shown in figure 7.14 by means of ψ-scans and slopes of (110/200) scans. All the ψ-scan show similar slopes except for one, the 60 nm nanostructures prepared at $250°C$ for 12 hours and cooled with 1 K/min to $30°C$, $cP_{60} - 250 - 12h$. The drastic increase in the slope, that is the broadness of ψ-scan, for $cP_{60} - 250 - 12h$, is unclear. From the TEM analysis in the chapter 5.2 it appears that the $cP_{60} - 250 - 12h$ sample has rod morphology and the other three samples show tube morphology. Therefore, it appears that the sample $cP_{60} - 250 - 12h$ show the transition from tube to rod morphology. The transition from tube to rod morphology is leading to the drastic change in the orientation. How the change in tube to rod is leading to the change in the orientation is unclear. Although, we know that the transition from tubes to rods lead to decreasing the surface area of the nanostructures.
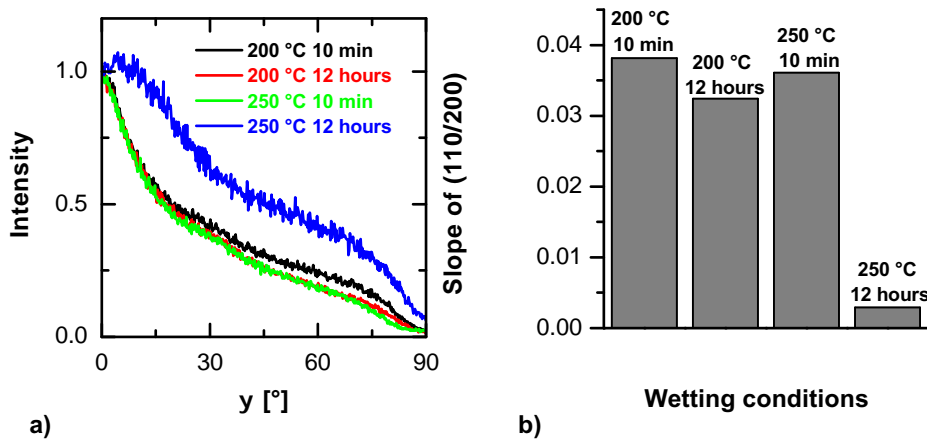
Figure 7.14: Effects of wetting conditions on orientation of (110/200) planes for 60 nm nanostructures a) ψ-scans and b) slope of (110/200)
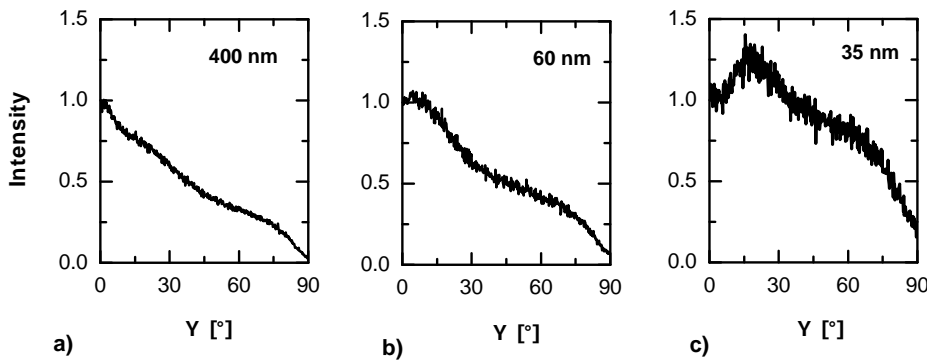

Figure 7.15: ψ-scans of (110/200) planes for a) 400 nm nanotubes,$cP_{400} - 250 - 12h$, b) 60 nm nanorods, $cP_{60} - 250 - 12h$ and c) 35 nm nanorods, $cP_{35} - 250 - 12h$, all the samples were wetted at 250 °C for 12 hours and cooled with 1 K/ min

The change in orientation as it goes from tube to rod morphology could also be observed in figure 7.15. It shows ψ-scans for 400 nm, 60 nm and 35 nm nanostructures, which were prepared by wetting the AAO template for 12 hours and then cooling to room temperature with cooling rate of 1 K/min. The 400 nm nanostructures showed tube morphology and the 35 nm and 60 nm nanostructures showed rod morphology, as discussed in chapter 5. The ψ-scans show that with decreasing pore diameter or increasing confinement the orientation becomes broader when the wetting time is long. The peak in

97

the ψ-scan of (110/200) planes is shifting to the larger angles by increasing the confinement. The 35 nm nanorods show the peak in the ψ-scan at 15°. Which means maximum number of the (110/200) planes are oriented 15° to the long axis of the pores. Therefore it appears that the morphology of the nanostructures play an important role in crystal orientation with the change from tube to rod morphology leading to the broadening of the orientation.

7.3.2 Orientation dependence on extent of confinement

It is expected that increasing the confinement, or reducing the pore diameter, should increase the degree of crystal orientation. In case of PVDF, it was observed that increasing the confinement from 400 nm to 35 nm, the degree of crystal orientation increases [10]. It was also found for PE that the full width of half maximum (FWHM), of azimuthal intensity corresponding to the (110) reflection, decreases linearly with decrease in the pore diameter [25]. It shows that there is a clear correlation between extent of confinement and degree of orientation. To determine the effect of confinement on the orientation distribution of the P(VDF-TrFE) crystallites, pore sizes of 35 nm, 60 nm, 180 nm and 400 nm diameters were used.

Figure 7.16 shows the ψ scans for 35 nm, 60 nm and 180 nm nanostructures. The ψ-scans for 400 nm nanotubes are shown in figure 7.6 b, it shows ψ-scans similar to the 180 nm nanotubes. Also the $\theta - 2\theta$ pattern is not shown here because the pattern looks identical to the 400 nm nanotubes
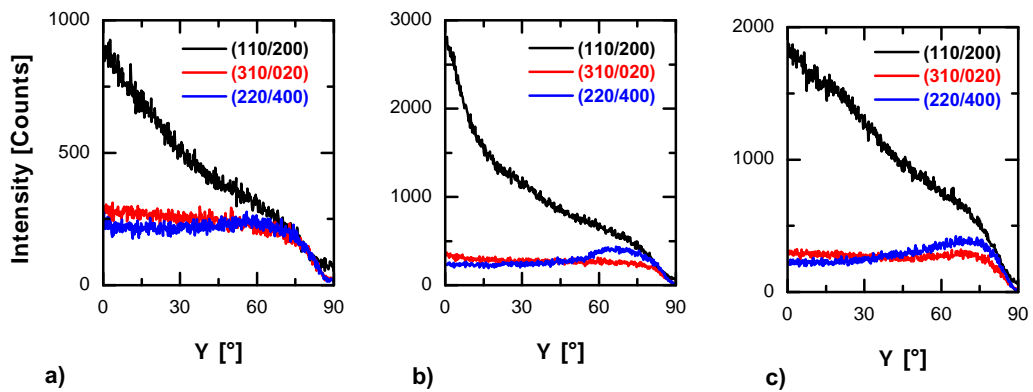

Figure 7.16: ψ-scans of PVDF-TrFE nanostructures prepared at wetting temperature of $250°C$ for 10 minutes and cooling with 1 K/min to $30°C$, a) 35 nm nanotubes, $cP_{35} - 250 - 10m$ b) 60 nm nanotubes, $cP_{60} - 250 - 10m$ and c) 180 nm nanotubes, $cP_{180} - 250 - 10m$

sample shown in figure 7.6 *a*, for all the samples. The samples were prepared at the wetting temperature of $200°C$ for 10 minutes and cooled with 1 K/min to $30°C$, all the samples show tube morphology. Although the morphology of the 35 nm and 60 nm nanostructures could not be confirmed as tubes or rods, we presume that for 10 minutes wetting time they show tube morphology, as discussed in chapter 5. The DSC results showed larger melting point depression for 35 nm nanorods than for 60 nm nanotubes, which means confinement is strongest in 35 nm nanotubes. For 180 nm and 400 nm there was no difference in the melting point which means both the nanostructures have similar crystal sizes or they are experiencing similar confinement. For the (110/200) ψ-scan the 60 nm nanostructures show narrow orientation compared to the 35 nm, 180 nm and 400 nm nanostructures. The ψ-scan for (220/400) planes show a peak at $60°$ angle for 60 nm and 180 nm nanostructures but not for 35 nm nanotubes. The peak at $\psi = 60°$ also show the indication of better orientation. Therefore, the ψ-scans show that the increase in confinement does not directly result into the better orientation. The orientation becomes narrow with increase in the confinement up to 60 nm diameter, further increase in the confinement leads to again broader orientation.

To analyze the results further, the ψ-scans corresponding to the (110/200) planes for 35 nm, 60 nm, 180 nm and 400 nm nanostructures are plotted together in figure 7.17. The slope of the ψ-scans are shown in the figure 7.17 *b*, measured close to $\psi = 0°$. The slopes of 35 nm, 180 nm and 400 nm have similar value but the 60 nm nanotubes show four time larger slope. That
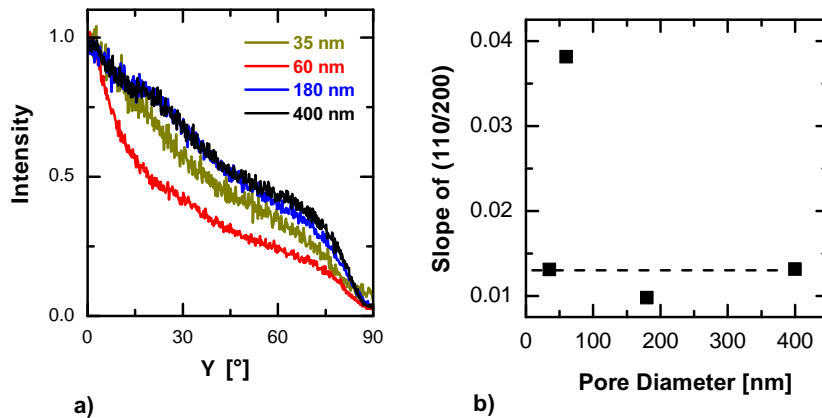

Figure 7.17: a) ψ-scans of (110/200) lattice planes for 35 nm, 60 nm, 180 nm and 400 nm nanostructures and b) slope of (110/200) ψ-scan plotted against pore diameter (the dashed line is guide for the eye)

is, the best orientation is shown by the 60 nm nanotubes. It was expected that the best orientation should be in the 35 nm nanotubes and it is clearly not the case, which is surprising. Increasing the confinement from 400 nm to 60 nm leads to better orientation of the (110/200) lattice planes because the increased confinement leads to uniform growth of the lamellae with less branching. The broad orientation in 35 nm nanotubes for (110/200) and no peak at $60°$ for the ψ-scan of second order lattice planes show that the orientation is deteriorate as the confinement is increased beyond 60 nm. The deterioration of orientation in 35 nm nanostructures could be due to the inability of the lamellae to fit into the strong confinement. The lamellae thickness being high in P(VDF-TrFE), the thick lamellaes are difficult to fit into the 35 nm pores therefore the c-axis is tilted with respect to the template surface leading to small crystallites with broader orientation. These results show that unlike the PVDF or PE, for the P(VDF-TrFE) nanostructures the increase in the confinement, beyond a certain limit, does not results into better orientation.

7.4 Preferred Orientation of (110) Planes Parallel to the Template Surface

Based on the $\theta-2\theta$ pattern and ψ-scan we concluded, in section 7.2, that the (110/200) planes are preferentially oriented parallel to the template surface. There are three possibilities about how the (110/200) planes could orient parallel to the template surface:

1. it is possible that both the (110) and (200) planes are equally oriented parallel to the template surface

2. only (200) planes are oriented parallel to the template surface

3. only (110) planes are oriented parallel to the template surface

Figure 7.18 shows the $\theta-2\theta$ pattern and ψ-scans for 60 nm nanostructures prepared at the wetting temperature of $200°C$ for 10 minutes and cooled with a cooling rate of 1 K/min to $30°C$, sample $cP_{60}-200-10m$. The 60 nm nanostructures is considered for the analysis because it shows the best orientation. Analysis of the $\theta-2\theta$ pattern and ψ-scan of the P(VDF-TrFE) nanostructures, figure 7.18, showed that the *case-1* and *case-2* can be excluded and only orientation with (110) planes parallel to the template surface is possible. The conclusion is reached from the $\theta-2\theta$ pattern which does not show the second order (220/400) reflection and also the ψ-scan of the
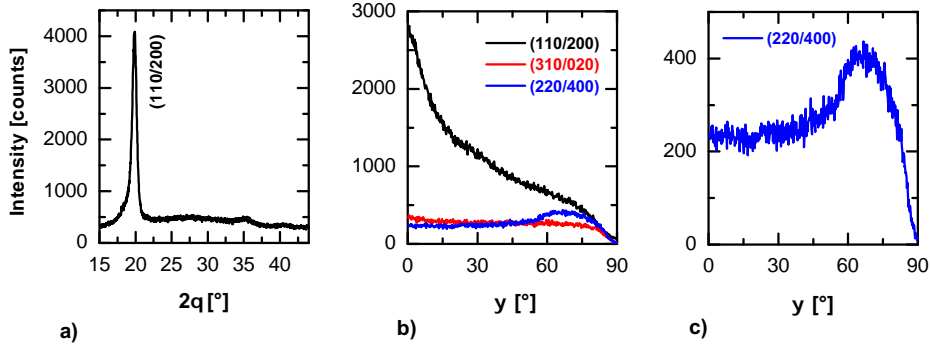
100

Figure 7.18: XRD of P(VDF-TrFE) 60 nm nanostructures prepared at wetting temperature of $200°C$ for 10 minutes and cooled to $30°C$ with a cooling rate of 1 K/min, sample $cP_{60} - 200 - 10m$, a) $\theta - 2\theta$ pattern, b) ψ-scans and c) ψ-scan of $(220/400)$

$(220/400)$ which show a peak at $\psi = 60°$, figure 7.18 *a, c*, indicate preferred (110) planes parallel to the template surface. The preferred orientation could be explained by the structure factors and intensity of certain *(hkl)* reflection.

Table 7.3 shows the structure factor and intensity for the corresponding lattice planes in P(VDF-TrFE). The structure factors are obtained from reference [84] which were calculated for 70:30 mol% VDF-TrFE. A planer zigzag model was considered with unit cell parameters of $a = 8.87\,\mathring{A}$, $b = 5.17\,\mathring{A}$, and $c = 2.55\,\mathring{A}$. We have also used 70:30 mol% VDF-TrFE, therefore the structure factors should be the same for our VDF-TrFE. Comparing the first

Reflection	Structure factor	Intensity
(hkl)	F(hkl)	I(hkl)
(200)	20.31	412.5
(110)	25.34	642.1
(310)	14.88	221.4
(020)	20.79	432.2
(400)	13.27	176.1
(220)	4.01	16.1
(001)	17.63	310.8
(111)	21.75	473.1
(201)	0.31	0.1

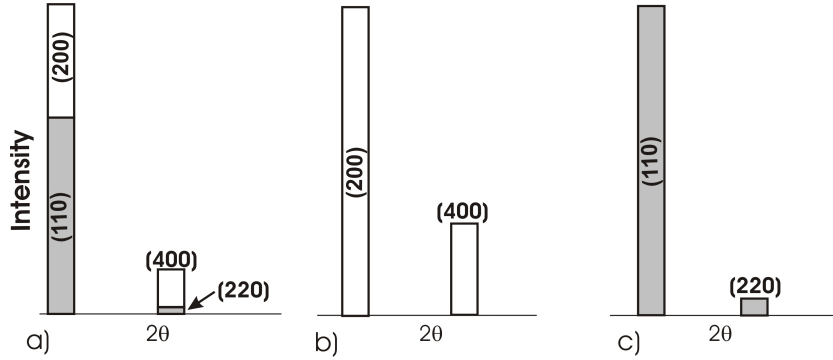Table 7.3: Structure factor and intensity [84]

101

Figure 7.19: Schematic representation of intensity composition for first order (100/200) and second order (220/400) peaks in $\theta - 2\theta$ pattern, a) if there is equal orientation of (110) and (220) b) only (200) is oriented parallel to the template surface and c) only (110) is oriented parallel to the template surface

order (110/200) and second order (220/400) lattice planes and their structure factors and intensity, figure 7.19 shows the different scenarios when there is 50/50 mixture of (110) and (200) or only (110) is present or only (200) is parallel to the template surface. The first order peak (110/200) is shown with the same intensity and relative intensity for second order peak (220/400) is compared, which depend on how much contribution to the intensity is from (220) or (400). From the analysis it is clear that the second order peak (220/400) will have minimum intensity when there is preferred orientation for (110) planes. The absence of (220/400) in the $\theta - 2\theta$ pattern of P(VDF-TrFE) 60 nm nanotubes (figure 7.18 a) shows that there is preferred orientation of (110) parallel to the template surface.

If the (110) planes are preferentially oriented parallel to the template surface then the (200) planes must be oriented at 60° to the substrate normal, as discussed in chapter 2 for the P(VDF-TrFE) lattice in the ferroelectric phase. The reflection corresponding to these two planes, (110) and (200), can be observed by rotating the sample in the ψ-scan at 0° and 60°, similarly the (220) and (400) planes will be at 0° and 60° in the ψ-scan. So, for preferred (110) planes parallel to the substrate, the peak for (110) at $\psi = 0°$ will have higher intensity than the (200) peak at $\psi = 60°$ due to larger structure factor of (110) planes. The peak intensities will be reverse for the second order planes (220/400), at $\psi = 0°$ the (220) will have lower intensity than the peak at $\psi = 60°$ corresponding (400) planes. Figure 7.20 shows the schematic representation of intensities at $\psi = 0°$ and $\psi = 60°$ if there is
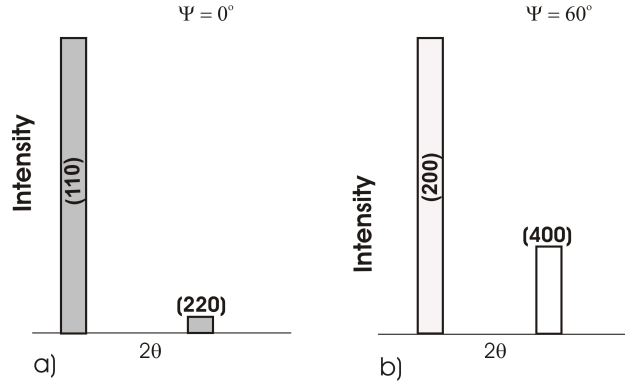
Figure 7.20: Schematic representation of intensity composition if the (110) planes are preferably oriented parallel to the template surface. a) intensity at $\psi = 0^0$ and b) intensity at $\psi = 60^0$

preferred (110) orientation parallel to the template. Figure 7.18 *b, c* shows the $\psi - scans$ of bulk P(VDF-TrFE) and $cP_{60} - 200 - 10min$ nanotubes. The $\psi - scan$ corresponding to the second order peak (220/400) (figure 7.18 b, c) shows a peak at 60^0 which confirms the preferred (110) orientation parallel to the template surface.

The temperature dependent $\theta - 2\theta$ pattern, in section 7.1, suggest that the P(VDF-TrFE) in the AAO nanopores have c-axis oriented parallel to the template surface. In the paraelectric phase the crystals have hexagonal symmetry and each molecular chain is in local conformational motion [85]. Due to the hexagonal symmetry there are many equally preferred growth faces in the paraelectric phase of P(VDF-TrFE). If we consider an orthorhombic unit cell, cf. figure 2.3 in chapter 2, we have two sets of equivalent planes in the hexagonal phase. One set is (020)(0-20)(310)(3-10)(-310)(-3-10) = {020} are all equivalent planes and the other set of equivalent planes are (200)(-200)(110)(1-10)(-110)(-1-10)={110}. In the ferroelectric phase the hexagonal symmetry is broken and the equivalence in each set of planes is lost. In the ferroelectric phase we found that only (110/200) planes are parallel to the template surface, corresponding to the growth of {110} face in the hexagonal phase, it is apparent from the $\theta - 2\theta$ pattern and ψ-scans of the 60 nm nanostructures in figure 7.18. The (310/020) planes parallel to the template surface is not observed which correspond to the {020} growth face in the hexagonal phase. It is an indication that the {110} growth face has higher rate of growth than the {020} growth face in the hexagonal phase in the P(VDF-TrFE) nanostructures which explain the absence of (310/020) peak in the nanostructures sample.
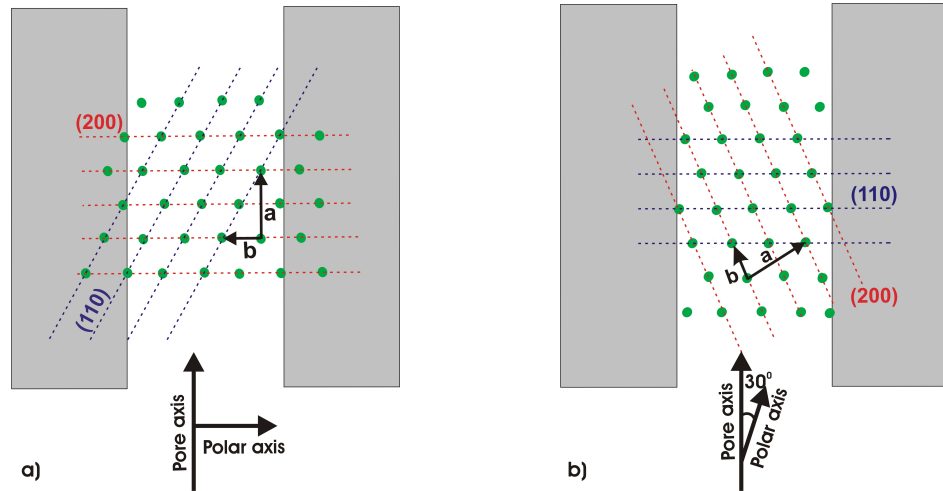
Figure 7.21: Two possible orientation of (200) and (110) lattice planes inside the nanopores a) (200) planes parallel to the template surface, the polar axis is perpendicular to the pore axis and b) (110) planes parallel to the template surface, the polar axis is oriented 30° to the pore axis

Further, structure factor analysis showed that only the (110) planes are parallel to the template surface at the room temperature ferroelectric phase. This selection of the (110) orientation parallel to the template surface must take place at the paraelectric to the ferroelectric phase transition because the (110) and (200) planes are equivalent in the hexagonal paraelectric phase. This indicates that the preferred orientation of the (110) planes parallel to the template surface must take place in two steps. In the first step the c-axis is oriented parallel to the template surface during the crystallization in the paraelectric phase and in the second step (110) orientation is preferred during the paraelectric to ferroelectric phase transition.

Although, it is possible for the crystallites to have both the (110) and (200) orientation when the nanostructures goes through the paraelectric to the ferroelectric transition. But only (110) planes parallel to the template surface is selected as a preferred orientation during the solid-solid phase transition. In order to understand why only the (110) orientation is preferred, we have to look for the differences between the (110) and (200) orientation parallel to the template surface. Figure 7.21 shows the two possible orientations within the nanopore walls. The orientation with (200) planes parallel to the template surface causes the b-axis to orient perpendicular to the long axis of the pores, figure 7.21 a. Such a orientation of b-axis creates surface charges on the nanostructures wall because the b-axis is a polar axis along which the dipoles are oriented. The surface charges are responsible for the creation of

104

depolarizing field which is energetically unfavorable. In case of (110) planes parallel to the template surface, the b-axis is oriented 30° to the long axis of the pores, as shown in figure 7.21 b. This result presented here confirm tentative results reported previously [86]. The orientation of b-axis at 30° angle to the long axis of the pores can avoid the formation of the surface charges. Therefore, it appears, that the preferred orientation of the (110) planes parallel to the template surface is favorable in order to minimize the surface charges on the nanostructures. The role of surface charges preferring the in-plane orientation can be explained by looking at the polarization in the ferroelectric thin films.

Polarization in ferroelectric thin films

The macroscopic bulk polarization is produced by displacement of positive and negative charges which creates net charge density of opposite sign at the opposite sides of the crystal, as shown in figure 7.22. Any inhomogeneity in the polarization acts like a charge density and the discontinuity in the polarization at an interface acts like a surface charge, as shown below.

The potential $V(r)$ induced by a dipole $\mathbf{P}$ at the origin is,

$$V(\mathbf{r}) = -\frac{1}{4\pi\epsilon_\circ}\mathbf{P} \cdot \nabla(\frac{1}{r}) \tag{7.3}$$

The potential due to a distributed polarization P(r) in a volume τ bounded by a surface $\mathbf{S}$ is,

$$
\begin{aligned}
V(\mathbf{r}) &= \frac{1}{4\pi\epsilon_\circ}\int_\tau d\mathbf{r}'\, \mathbf{P}(\mathbf{r}') \cdot \nabla_{\mathbf{r}'}\left(\frac{1}{|\,\mathbf{r}-\mathbf{r}'\,|}\right) \\
&= \frac{1}{4\pi\epsilon_\circ}\int_\tau d\mathbf{r}'\left[-\frac{\nabla \cdot \mathbf{P}(\mathbf{r}')}{|\,\mathbf{r}-\mathbf{r}'\,|} + \nabla \cdot \left(\frac{\mathbf{P}(\mathbf{r}')}{|\,\mathbf{r}-\mathbf{r}'\,|}\right)\right] \\
&= \frac{1}{4\pi\epsilon_\circ}\left[-\int_\tau d\mathbf{r}'\frac{\nabla \cdot \mathbf{P}(\mathbf{r}')}{|\,\mathbf{r}-\mathbf{r}'\,|} + \int_S \frac{d\mathbf{S} \cdot \mathbf{P}(\mathbf{r}')}{|\,\mathbf{r}-\mathbf{r}'\,|}\right]
\end{aligned} \tag{7.4}
$$

The potential is generated by bulk charge density $\rho(\mathbf{r}) = -\nabla \cdot \mathbf{P}(\mathbf{r})$ and surface charge density $\sigma = \mathbf{P} \cdot \mathbf{n}$ where $\mathbf{n}$ is the vector normal to the surface S [87].

If the polarization $\mathbf{P}$ is assumed to be homogeneous within a ferroelectric domain and changing abruptly at surfaces and interfaces, only the surface term survives. The surface charges are responsible for the creation of depolarization field, the system tries to minimize the depolarization field by eliminating the surface charges. Therefore, in thin films, the preferred orientation of the polarization will be in the plane of the film rather than perpendicular
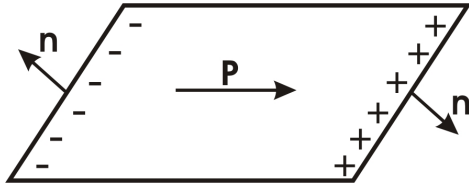
Figure 7.22: Surface charge density generated by a bulk polarization at an interface

to the film to minimize the surface charges [87]. It is clear that polarization will change in a way to minimize the depolarization field. In case of P(VDF-TrFE) nanostructures, during the para- to ferro- transition, the b-axis rotate around the chain axis and orient at 30° to the long axis of the pores in order to avoid the formation of surface charges. This orientation corresponds to the preferred (110) planes parallel to the template surface. The P(VDF-TrFE) nanostructures have in-plane orientation of the polar axis rather than the out of plane orientation. If we consider a P(VDF-TrFE) nanotube and cut it along the long axis, it will form a thin film. The thin film, shown in figure 7.23 with (110) orientation will have the polar axis oriented 30° to the long axis of the plane. Therefore the polarization will have the major in-plane component and an out of plane component. This orientation does not create surface charges and minimize the depolarization field.

Schilling et al. has shown that the polarization direction, in the ferroelectric domains of $BaTiO_3$ single crystal column, changes when the morphology of the column is changed. The change in polarization direction is such that the polarization always points perpendicular to the smallest lateral dimension of the column [88]. Schilling et al. have attributed the change in polarization to the minimization of the depolarization field in the columns.
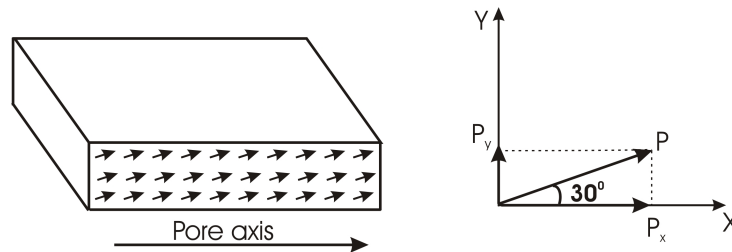

Figure 7.23: Shows the polarization in a thin film made by cutting a nanotube along the long axis (left) and components of the polarization (right)

106

7.5 Quenched Nanostructures: Preferred (200) Orientation

The nanostructures prepared by long wetting time and quenching showed completely different orientation. Figure 7.24 shows the $\theta - 2\theta$ pattern as well the ψ-scans for the 400 nm nanotubes sample, $qP_{400} - 250 - 12h$, prepared at $250°C$ for 12 hours and quenched. The $\theta - 2\theta$ pattern in figure 7.24 a shows the higher intensity for (310/020) and (220/400) peaks than the (110/200) peak which was not observed even in the isotropic bulk sample, figure 7.1. In the $\theta - 2\theta$ pattern of the quenched sample, figure 7.24, the second order peak at $2\theta = 40.8°$ corresponding to (220/400) is more intense than the first order peak at $2\theta = 19.8°$ for the (110/200) planes. The structure factors of only (220/400) planes alone could not be responsible for the larger intensity of the peak at $2\theta = 40.8°$. This suggest that there is contribution from (hkl) planes with non-zero l-index. This means, there are some crystallites having the c-axis orientation parallel to the long axis of the pores. This is also true for the peak at $2\theta = 35.1°$, where there is also contribution of (hkl) planes having non-zero l-index.

In the ψ-scans, figure 7.24 b, the (110/200) scan shows a peak at $60°$. It is possible that now the (200) planes are parallel to the template surface and then the (110) should orient $60°$ to the (200) planes and hence to the template surface. As we have seen in the last section with larger structure factor for
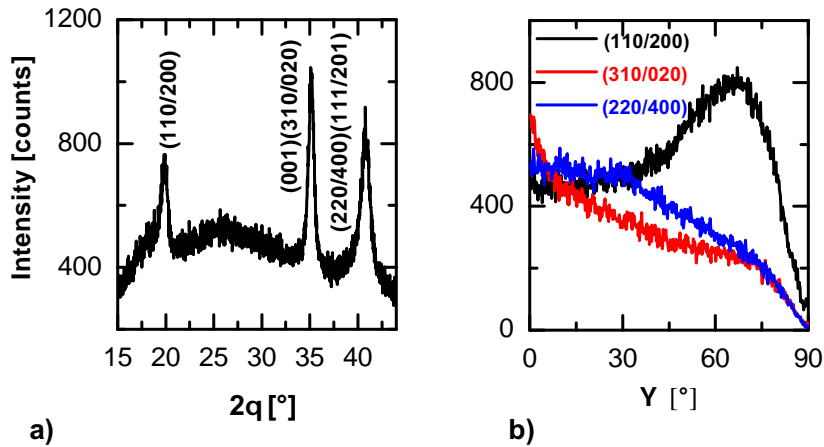

Figure 7.24: XRD results for P(VDF-TrFE) 400 nm nanotubes wetted at $250°C$ for 12 hours and quenched, sample $cP_{400} - 250 - 12h$; a) $\theta - 2\theta$ scan and b) ψ scans

the (110) planes the, maximum intensity should occur at $\psi = 60°$ which is also observed in the ψ-scan of (110/200), figure 7.24 *b*. With preferred orientation (200) planes parallel to the template surface it is expected that the ψ-scan for second order planes, (220/400), show more intensity at $\psi = 0°$ than at $\psi = 60°$ which is evident in the ψ-scan, figure 7.24 *b*. Which is also an indication of preferred orientation of (200) planes parallel to the template surface.

The above results show that the samples quenched after long wetting time have c-axis parallel to the pore axis and (200) planes are oriented parallel to the template surface. By quenching the sample, the crystallization is nucleation dominated while in the slowly cooled samples crystallization is dominated by crystal growth. The nucleation dominated crystallization, by quenching, can lead to formation of small crystallites with c-axis perpendicular to the template surface. In the slowly cooled samples the kinetics of the crystal growth plays a role, resulting in the preferred orientation of the c-axis parallel to the template surface. Finally, the slow cooling also gives enough time for the para- to ferro- transition during which the polar b-axis rotate around the chains (c-axis), resulting in preferred (110) planes parallel to the template surface. By quenching the sample, there is not enough time for the selection of the preferred orientation during the para- to ferro- transition, resulting in the freezing a orientation that is not energetically favorable.

7.6   Summary

In the P(VDF-TrFE) ferroelectric nanostructures, it was observed that the (110) planes are preferentially oriented parallel to the template surface, when cooled from the melt with a cooling rate of 1 K/min. The polar b-axis was found to be oriented 30° to the long axis of the pores. There are indications that the preferred orientation takes place in two steps. In the first step, during the crystallization the growth kinetics leads to preferred orientation of the c-axis parallel to the template surface. In the second step, during the paraelectric to ferroelectric phase transition, (110) planes are oriented parallel to the template surface. This orientation is favored in order to minimize the depolarizing field created by the surface charges. The quenched samples showed similar orientation to that of the bulk isotropic sample indicating that the crystallization is dominated by nucleation which lead to a broad orientation. This suggests that slow cooling is necessary for preferred orientation where crystal growth kinetics is responsible for the orientation of the c-axis parallel to the template surface.

The preferred orientation was found to be the function of wetting time

and temperature which ultimately is responsible for the change in morphology. Tube morphology showed better orientation than the rod morphology. Increase in the confinement lead to better orientation only until 60 nm diameter of the nanopores, further increase in confinement to 35 nm diameter of the nanopores lead to broader orientation.

Chapter 8

Conclusions

We studied the morphology, crystal orientation and phase transitions in the ferroelectric P(VDF-TrFE) nanostructures. It is known that wetting of AAO nanopores by polymers takes place either with precursor wetting or by capillary wetting mechanism. Our analysis by SEM and TEM showed that the P(VDF-TrFE) wets the AAO nanopores by precursor wetting mechanism. This was evident from the tube morphology of the 400 nm nanostructures. The P(VDF-TrFE) nanostructures with 35 nm and 60 nm diameters showed tube or rod morphology depending on the wetting time. The rod morphology in the 35 nm and 60 nm is reached via the initial formation of tubes and then through an intermediate step of Rayleigh instabilities to the complete filling of the AAO nanopores.

We have analyzed the phase transitions in the P(VDF-TrFE) nanostructures of different diameters having the tube morphology with DSC. The DSC results show that confinement of P(VDF-TrFE) in the AAO nanopores lead to melting point depression because the lamellae thickness in the P(VDF-TrFE) nanostructures is restricted by the confinement. It was also shown that the crystallization in the AAO nanopores proceeds with homogeneous nucleation and the walls of the AAO nanopores does not act as nucleating sites. The effective annealing of the ferroelectric nanostructures in the para-electric phase lead to increase in the melting temperature and decrease in the Curie temperature. This could be explained by the shift in the Gibbs free energy due to annealing in the paraelectric phase. It was also shown that the Curie temperature is intrinsically linked with the lamellae thickness of the P(VDF-TrFE).

The x-ray scattering results showed that the (110) planes, in the P(VDF-TrFE) nanostructures, are preferentially oriented parallel to the template surface, depending on the crystallization conditions and morphology. There are indications that the preferred orientation takes place in two steps. In

the first step, during the crystallization the c-axis is preferentially oriented parallel to the template surface; it is the result of the crystallization kinetics which allows the crystal to grow along the pore axis. In the second step, during the paraelectric to ferroelectric phase transition, preferred orientation of (110) planes parallel to the template surface is chosen. The selection of the preferred orientation takes place in two steps because after crystallization the polymer is in hexagonal phase with six equivalent directions of growth therefore no preferred growth front exists. During the para- to ferro- transition the hexagonal symmetry is broken and the (110) planes are preferentially oriented parallel to the template surface. In the preferred orientation of (110) planes parallel to the template surface the b-axis, also the polar axis, makes an angle 30° to the long axis of the pores. The (200) orientation parallel to the template surface is not preferred because it is associated with formation of the surface charges. The surface charges are responsible for creation of the depolarization field which is energetically unfavorable. It was also found that the preferred orientation in the nanostructures depend on the morphology and extent of confinement.

In the ferroelectric materials, crystal orientation in certain direction is the first basic step of having the ferroelectric properties. Unlike the bulk P(VDF-TrFE) where the orientation can be imparted by mechanical means, in the nanostructure the orientation of the polymer crystallites could only be possible by self organization. We have shown that the self organization of P(VDF-TrFE) in the confinement of AAO nanopores leads to preferred orientation. The P(VDF-TrFE) nanostructures have the preferred orientation of the c-axis parallel to the template surface. This could allow the switching of the polarization direction under the electric field, as it is known that in the P(VDF-TrFE), the ferroelectric dipole can rotate around the c-axis. This work provides the ground work for fully functional ferroelectric P(VDF-TrFE) nanostructures.

Bibliography

[1] B. Yoon, M. Y. Sung, S. Yeon, H. S. Oh, Y. Kwon, C. Kim, and K. H. Kim, "Metal-ferroelectric-metal capacitor based persistent memory for electronic product code class-1 generation-2 uhf passive radio-frequency identification tag," *Journal of Applied Physics*, vol. 105, p. 061628, Mar. 2009.

[2] J. F. Scott, "Applications of modern ferroelectrics," *Science*, vol. 315, pp. 954–959, Feb. 2007.

[3] A. Chung, J. Deen, J. S. Lee, and M. Meyyappan, "Nanoscale memory devices," *Nanotechnology*, vol. 21, p. 412001, Oct. 2010.

[4] S. B. Lang and S. Muensit, "Review of some lesser-known applications of piezoelectric and pyroelectric polymers," *Applied Physics A-materials Science & Processing*, vol. 85, pp. 125–134, Nov. 2006.

[5] K. Shin, H. Xiang, S. Moon, T. Kim, T. McCarthy, and T. Russell, "Curving and frustrating flatland," *Science*, vol. 306, p. 76, OCT 1 2004.

[6] H. Q. Xiang, K. Shin, T. Kim, S. I. Moon, T. J. McCarthy, and T. P. Russell, "Block copolymers under cylindrical confinement," *Macromolecules*, vol. 37, pp. 5660–5664, July 2004.

[7] Z. H. Yang, Y. Fujii, F. K. Lee, C. H. Lam, and O. K. C. Tsui, "Glass transition dynamics and surface layer mobility in unentangled polystyrene films," *Science*, vol. 328, pp. 1676–1679, June 2010.

[8] M. Alcoutlabi and G. B. McKenna, "Effects of confinement on material behaviour at the nanometre size scale," *Journal of Physics-condensed Matter*, vol. 17, pp. R461–R524, Apr. 2005.

[9] M. K. Mundra, S. K. Donthu, V. P. Dravid, and J. M. Torkelson, "Effect of spatial confinement on the glass-transition temperature of patterned polymer nanostructures," *Nano Letters*, vol. 7, pp. 713–718, Mar. 2007.

[10] M. Steinhart, P. Goering, H. Dernaika, M. Prabhukaran, U. Goesele, E. Hempel, and T. Thurn-Albrecht, "Coherent Kinetic Control Over Crystal Orientation in Macroscopic Ensembles of Polymer Nanorods and Nanotubes," *Physical Review Letters*, vol. 97, JUL 14 2006.

[11] M.-C. Garcia-Gutierrez, A. Linares, J. J. Hernandez, D. R. Rueda, T. A. Ezquerra, P. Poza, and R. J. Davies, "Confinement-Induced One-Dimensional Ferroelectric Polymer Arrays," *Nano Letters*, vol. 10, pp. 1472–1476, APR 2010.

[12] H. P. Wang, J. K. Keum, A. Hiltner, E. Baer, B. Freeman, A. Rozanski, and A. Galeski, "Confined crystallization of polyethylene oxide in nanolayer assemblies," *Science*, vol. 323, pp. 757–760, Feb. 2009.

[13] L. Zhu, S. Z. D. Cheng, B. H. Calhoun, Q. Ge, R. P. Quirk, E. L. Thomas, B. S. Hsiao, F. J. Yeh, and B. Lotz, "Crystallization temperature-dependent crystal orientations within nanoscale confined lamellae of a self-assembled crystalline-amorphous diblock copolymer," *Journal of the American Chemical Society*, vol. 122, pp. 5957–5967, June 2000.

[14] Y. L. Loo, R. A. Register, A. J. Ryan, and G. T. Dee, "Polymer crystallization confined in one, two, or three dimensions," *Macromolecules*, vol. 34, pp. 8968–8977, Dec. 2001.

[15] D. J. Quiram, R. A. Register, and G. R. Marchand, "Crystallization of asymmetric diblock copolymers from microphase-separated melts," *Macromolecules*, vol. 30, pp. 4551–4558, Aug. 1997.

[16] J. Kraus, P. Muller-Buschbaum, T. Kuhlmann, D. W. Schubert, and M. Stamm, "Confinement effects on the chain conformation in thin polymer films," *Europhysics Letters*, vol. 49, pp. 210–216, Jan. 2000.

[17] Y. J. Park, S. J. Kang, C. Park, B. Lotz, A. Thierry, K. J. Kim, and J. Huh, "Molecular and crystalline microstructure of ferroelectric poly(vinylidene fluoride-co-trifluoroethylene) ultrathin films on bare and self-assembled monolayer-modified au substrates," *Macromolecules*, vol. 41, pp. 109–119, Jan. 2008.

[18] Y. J. Park, S. J. Kang, C. Park, K. J. Kim, H. S. Lee, M. S. Lee, U. I. Chung, and I. J. Park, "Irreversible extinction of ferroelectric polarization in p(vdf-trfe) thin films upon melting and recrystallization," *Applied Physics Letters*, vol. 88, p. 242908, June 2006.

114

[19] M. Steinhart, J. Wendorff, A. Greiner, R. Wehrspohn, K. Nielsch, J. Schilling, J. Choi, and U. Gosele, "Polymer nanotubes by wetting of ordered porous templates," *Science*, vol. 296, p. 1997, JUN 14 2002.

[20] C. R. Martin, "Nanomaterials - a membrane-based synthetic approach," *Science*, vol. 266, pp. 1961–1966, Dec. 1994.

[21] M. Steinhart, "Supramolecular Organization of Polymeric Materials in Nanoporous Hard Templates," in *Self-Assembled Nanomaterials ii: Nanotubes*, vol. 220 of *Advances In Polymer Science*, pp. 123–187, Springer-Verlag Berlin, 2008.

[22] A. Sato, Y. Pennec, N. Shingne, T. Thum-Albrecht, W. Knoll, M. Steinhart, B. Djafari-Rouhani, and G. Fytas, "Tuning and switching the hypersonic phononic properties of elastic impedance contrast nanocomposites," *Acs Nano*, vol. 4, pp. 3471–3481, June 2010.

[23] A. Gitsas, B. Yameen, T. D. Lazzara, M. Steinhart, H. Duran, and W. Knoll, "Polycyanurate nanorod arrays for optical-waveguide-based biosensing," *Nano Letters*, vol. 10, pp. 2173–2177, June 2010.

[24] J. T. Chen, M. F. Zhang, and T. P. Russell, "Instabilities in nanoporous media," *Nano Letters*, vol. 7, pp. 183–187, Jan. 2007.

[25] K. Shin, E. Woo, Y. G. Jeong, C. Kim, J. Huh, and K.-W. Kim, "Crystalline structures, melting, and crystallization of linear polyethylene in cylindrical nanopores," *Macromolecules*, vol. 40, pp. 6617–6623, SEP 4 2007.

[26] J. L. Lutkenhaus, K. McEnnis, A. Serghei, and T. P. Russell, "Confinement Effects on Crystallization and Curie Transitions of Poly(vinylidene fluoride-co-trifluoroethylene)," *Macromolecules*, vol. 43, pp. 3844–3850, APR 27 2010.

[27] C.-C. Wang, Q.-D. Shen, S.-C. Tang, Q. Wu, H.-M. Bao, C.-Z. Yang, and X.-Q. Jiang, "Ferroelectric polymer nanotubes with large dielectric constants for potential all-organic electronic devices," *Macromol. Rapid Commun.*, vol. 29, no. 9, pp. 724–728, 2008.

[28] Z. J. Hu, M. W. Tian, B. Nysten, and A. M. Jonas, "Regular arrays of highly ordered ferroelectric polymer nanostructures for non-volatile low-voltage memories," *Nature Materials*, vol. 8, pp. 62–67, Jan. 2009.

[29] K. J. Kim, G. B. Kim, C. L. Vanlencia, and J. F. Rabolt, "Curie Transition, Ferroelectric Crystal Structure, and Ferroelectricity of a VDF/TrFE (75/25) Copolymer 1. The Effect of the Consecutive Annealing in the Ferroelectric State on Curie Transition and Ferroelectric Crystal-Structure," *Journal Of Polymer Science Part B-Polymer Physics*, vol. 32, pp. 2435–2444, NOV 30 1994.

[30] M. A. Barique and H. Ohigashi, "Annealing Effects on the Curie Transition Temperature and Melting Temperature of Poly(vinylidene Fluoride/trifluoroethylene) Single Crystalline Films," *Polymer*, vol. 42, pp. 4981–4987, MAY 2001.

[31] R. Tanaka, K. Tashiro, and M. Kobayashi, "Annealing effect on the ferroelectric phase transition behavior and domain structure of vinylidene fluoride (VDF)-trifluoroethylene copolymers: a comparison between uniaxially oriented VDF 73 and 65% copolymers," *Polymer*, vol. 40, pp. 3855–3865, JUN 1999.

[32] K. Tashiro, R. Tanaka, K. Ushitora, and M. Kobayashi, "Annealing effect on ferroelectric phase transitional behavior of vinylidene fluoride-trifluoroethylene copolymers: An interpretation based on the concept of domain and trans-gauche conformational disorder," *Ferroelectrics*, vol. 171, no. 1, pp. 145–162, 1995.

[33] R. G. Kepler and R. A. Anderson, "Ferroelectric Polymers," *Advances In Physics*, vol. 41, pp. 1–57, JAN-FEB 1992.

[34] F. J. B. Calleja, A. G. Arche, T. A. Ezquerra, C. S. Cruz, F. Batallan, B. Frick, and E. L. Cabarcos, "Structure and Properties of Ferroelectric Copolymers of Poly(vinylidene fluoride)," *Advances in Polymer Science*, vol. 108, pp. 1–48, 1993.

[35] A. J. Lovinger, "Ferroelectric Polymers," *Science*, vol. 220, no. 4602, pp. 1115–1121, 1983.

[36] T. Furukawa, "Ferroelectric Properties of Vinylidene Fluoride Copolymers," *Phase Transitions*, vol. 18, no. 3-4, Part B, pp. 143–211, 1989.

[37] H. S. Nalwa, ed., *Ferroelectric Polymers: Chemisty, Physics and Applications.* Marcel Dekker, 1995.

[38] D. K. Dasgupta, "Pyroelectricity In Polymers," *Ferroelectrics*, vol. 118, no. 1-4, pp. 165–189, 1991.

[39] K. Tashiro, S. Sasaki, and S. Saragai, "Time-resolved wide-angle X-ray scattering measurements during the isothermal crystallization and ferroelectric phase-transition processes of a vinylidene fluoride/trifluoroethylene copolymer," *Journal of Polymer Science Part B-Polymer Physics*, vol. 42, pp. 4175–4181, NOV 15 2004.

[40] K. Tashiro and R. Tanaka, "Structural Correlation Between Crystal Lattice and Lamellar Morphology in the Ferroelectric Phase Transition of Vinylidene Fluoride-trifluoroethylene Copolymers as Revealed by the Simultaneous Measurements of Wide-angle and Small-angle X-ray Scatterings," *Polymer*, vol. 47, pp. 5433–5444, JUL 12 2006.

[41] S. Sasaki, A. Funato, K. Kubo, and A. Chiba, "Macrostructure of melt-crystallized vinylidene fluoride trifluoroethylene copolymers (37/63-mol-percent, 65/35-mol-percent, 73/27-mol-percent)," *Japanese Journal of Applied Physics Part 1-regular Papers Short Notes & Review Papers*, vol. 34, pp. 3177–3185, June 1995.

[42] M. V. Fernandez, A. Suzuki, and A. Chiba, "Study of annealing effects on the structure of vinylidene fluoride trifluoroethylene copolymers using waxs and saxs," *Macromolecules*, vol. 20, pp. 1806–1811, Aug. 1987.

[43] E. L. Cabarcos, B. de las Rivas, T. A. Ezquerra, and F. J. B. Calleja, "Toward chain extension in crystals of fluorinated copolymers as revealed by real time ultra-small-angle x-ray scattering," *Macromolecules*, vol. 31, pp. 6157–6163, Sept. 1998.

[44] M. Hikosaka, K. Sakurai, H. Ohigashi, and A. Keller, "Role of transient metastable hexagonal phase in the formation of extended-chain single-crystals of vinylidene fluoride and trifluoroethylene copolymers," *Japanese Journal of Applied Physics Part 1-regular Papers Short Notes & Review Papers*, vol. 33, pp. 214–219, Jan. 1994.

[45] H. Masuda and K. Fukuda, "Ordered Metal Nanohole Arrays Made by a 2-step Replication of Honeycomb Structures of Anodic Alumina," *Science*, vol. 268, pp. 1466–1468, JUN 9 1995.

[46] C. Kittel, *Introduction to Solid State Physics*. John Wiley & Sons, inc., eighth ed., 2005.

[47] V. Randel and O. Engler, *Introduction to Texture Analysis: Macrostructure, Microstructure and Orientation Mapping*. CRC Press, 2000.

[48] V. B. F. Mathot, ed., *Calorimetry and Thermal Analysis of Polymers.* Hanser, 1993.

[49] M. von Heimendahl, *Electron Microscopy of Materials: An Introduction.* Academic Press, 1980.

[50] L. Schulz, "A Direct Method of Determining Preferred Orientation of a Flat Reflection Sample Using a Geiger Counter X-ray Spectrometer," *Journal Of Applied Physics*, vol. 20, no. 11, pp. 1030–1032, 1949.

[51] T. E, "Defocusing for Schulz Technique of Determining Preferred Orientation," *Journal of Applied Physics*, vol. 41, no. 10, pp. 3944–&, 1970.

[52] H. EM and G. Rieck, "Defocusing Effects in Reflection Technique for Determination of Preferred Orientation," *Journal of Applied Crystallography*, vol. 7, no. APR1, pp. 286–290, 1974.

[53] W. Chernock and P. Beck, "Analysis of Certain Errors in the X-ray Reflection Method for the Quantitative Determination of Preferred Orientations," *Journal of Applied Physics*, vol. 23, no. 3, pp. 341–345, 1952.

[54] M. Birkholz, *Thin Film Analysis by X-Ray Scattering.* WILEY-VCH Verlag GmbH & Co. KGaA, Weinheim, 2006.

[55] R.-J. Roe, *Methods of X-Ray and Neutron Scattering in Polymer Science.* Oxford University Press, 2000.

[56] G. D. Sulka, *Nanostructured Materials in Electrochemistry.* WILEY-VCH Verlag GmbH & Co. KGaA, Weinheim, 1 ed., 2008.

[57] *X'Pert MRD Service Manual.*

[58] M. Steinhart, J. Wendorff, and R. Wehrspohn, "Nanotubes a la carte: Wetting of porous templates," *ChemPhysChem*, vol. 4, pp. 1171–1176, NOV 14 2003.

[59] M. Steinhart, R. Wehrspohn, U. Gosele, and J. Wendorff, "Nanotubes by template wetting: A modular assembly system," *Angewandte Chemie-international Edition*, vol. 43, no. 11, pp. 1334–1344, 2004.

[60] M. Zhang, P. Dobriyal, J. Chen, T. Russell, J. Olmo, and A. Merry, "Wetting transition in cylindrical alumina nanopores with polymer melts," *Nano Letters*, vol. 6, pp. 1075–1079, MAY 2006.

[61] D. Bonn and D. Ross, "Wetting Transitions," *Reports on Progress in Physics*, vol. 64, pp. 1085–1163, SEP 2001.

[62] P.-G. de Gennes, F. Brochard-Wyart, and D. Quere, *Capillarity and Wetting Phenomena*. Springer-Verlag, 2004.

[63] L. Girifalco and R. Good, "A Theory for the Estimation of Surface and Interfacial Energies .1. Derivation and Application to Interfacial Tension," *Journal Of Physical Chemistry*, vol. 61, no. 7, pp. 904–909, 1957.

[64] H. Tavana and A. W. Neumann, "Recent progress in the determination of solid surface tensions from contact angles," *Advances in Colloid and Interface Science*, vol. 132, pp. 1–32, MAR 28 2007.

[65] M. Daoud and C. E. Williams, eds., *Soft Matter Physics*. Springer-Verlag, 1999.

[66] H. Fox, E. Hare, and W. Zisman, "Wetting Properties of Organic Liquids on High Energy Surfaces," *Journal of Physical Chemistry*, vol. 59, no. 10, pp. 1097–1106, 1955.

[67] D. W. Van Krevelen, *Properties of Polymers*. Elsevier, third ed., 1990.

[68] K. Balani and A. Agarwal, "Wetting Of Carbon Nanotubes By Aluminum Oxide," *Nanotechnology*, vol. 19, APR 23 2008.

[69] H. Wu, W. Wang, Y. Huang, and Z. Su, "Orientation of Syndiotactic Polystyrene Crystallized in Cylindrical Nanopores," *Macromolecular Rapid Communications*, vol. 30, pp. 194–198, FEB 2 2009.

[70] F. Heslot, A. Cazabat, and P. Levinson, "Dynamics of Wetting of Tiny Drops - Ellipsometric Study of the Late Stages of Spreading," *Physical Review Letters*, vol. 62, pp. 1286–1289, MAR 13 1989.

[71] F. Heslot, N. Fraysse, and A. Cazabat, "Molecular Layering in the Spreading of Wetting Liquid-drops," *Nature*, vol. 338, pp. 640–642, APR 20 1989.

[72] M. Bernadiner, "A capillary microstructure of the wetting front," *Transport in Porous Media*, vol. 30, pp. 251–265, MAR 1998.

[73] L. Rayleigh, "On the instability of cylindrical fluid surfaces," *Phill. Mag. Series 5*, vol. 34, pp. 177–180, 1892.

119

[74] J.-T. Chen, M. Zhang, and T. P. Russell, "Instabilities in nanoporous media," *Nano Lett.*, vol. 7, p. 183, JAN 2007.

[75] J. Legrand, "Structure and Ferroelectric Properties of P(vdf-trfe) Copolymers," *Ferroelectrics*, vol. 91, pp. 303–317, 1989.

[76] T. Yagi, M. Tatemoto, and J. Sako, "Transition Behavior and Dielectric-properties in Trifluoroethylene and Vinylidene Fluoride Co-polymers," *Polymer Journal*, vol. 12, no. 4, pp. 209–223, 1980.

[77] C. L. Jackson and G. B. Mckenna, "The melting behavior of organic materials confined in porous solids," *Journal of Chemical Physics*, vol. 93, pp. 9002–9011, Dec. 1990.

[78] C. L. Jackson and G. B. McKenna, "Vitrification and crystallization of organic liquids confined to nanoscale pores," *Chemistry of Materials*, vol. 8, pp. 2128–2137, Aug. 1996.

[79] M. V. Massa, J. L. Carvalho, and K. Dalnoki-Veress, "Direct visualisation of homogeneous and heterogeneous crystallisation in an ensemble of confined domains of poly(ethylene oxide)," *European Physical Journal E*, vol. 12, pp. 111–117, Sept. 2003.

[80] M. V. Massa and K. Dalnoki-Veress, "Homogeneous crystallization of poly(ethylene oxide) confined to droplets: The dependence of the crystal nucleation rate on length scale and temperature," *Phys. Rev. Lett.*, vol. 92, p. 255509, June 2004.

[81] A. Guinier, *X-Ray Diffraction In Crystals, Imperfect Crystals, and Amorphous Bodies*. W. H. Freeman and Company, 1963.

[82] H. Wu, W. Wang, H. Yang, and Z. Su, "Crystallization and orientation of syndiotactic polystyrene in nanorods," *Macromolecules*, vol. 40, pp. 4244–4249, JUN 12 2007.

[83] M. Steinhart, S. Senz, R. Wehrspohn, U. Gosele, and J. Wendorff, "Curvature-directed crystallization of poly(vinylidene difluoride) in nanotube walls," *Macromolecules*, vol. 36, pp. 3646–3651, MAY 20 2003.

[84] J. A. Day, E. L. V. Lewis, and G. R. Davies, "X-Ray Structural Study Of Oriented Vinylidene Fluoride Trifluoroethylene Copolymers," *Polymer*, vol. 33, no. 8, pp. 1571–1578, 1992.

[85] H. Ohigashi, K. Omote, H. Abe, and K. Koga, "Chain motions in the paraelectric phase in single crystalline films of vinylidene fluoride and trifluoroethylene copolymer p(vdf/trfe)," *Journal of the Physical Society of Japan*, vol. 68, pp. 1824–1827, June 1999.

[86] Y. Luo, *Functional Nanostructures by Ordered Porous Templates*. PhD thesis, Martin Luther University, Halle, 2005.

[87] K. M. Rabe, C. H. Ahn, and J.-M. Triscone, eds., *Physics of Ferroelectrics: A Modern Perspective*. Springer-Verlag, 2007.

[88] A. Schilling, R. M. Bowman, G. Catalan, J. F. Scott, and J. M. Gregg, "Morphological control of polar orientation in single-crystal ferroelectric nanowires," *Nano Letters*, vol. 7, pp. 3787–3791, DEC 2007.

APPENDIX I

Table 1 shows the sample details for the ferroelectric P(VDF-TrFE).

Sample name	Nonopore diameter	Wetting temperature	Wetting time	Cooling history	Morphology
cP_{400}-200-12h	400 nm	200°C	12 hours	1 K/min	Tubes
cP_{400}-200-10m	400 nm	200°C	10 minutes	1 K/min	Tubes
cP_{400}-250-12h	400 nm	250°C	12 hours	1 K/min	Tubes
cP_{400}-250-10m	400 nm	250°C	10 minutes	1 K/min	Tubes
qP_{400}-200-10m	400 nm	200°C	10 minutes	quenched	Tubes
qP_{400}-250-10m	400 nm	250°C	10 minutes	quenched	Tubes
qP_{400}-250-12h	400 nm	250°C	12 hours	quenched	Tubes
cP_{60}-200-10m	60 nm	200°C	10 minutes	1 K/min	Tubes
cP_{60}-250-10m	60 nm	250°C	10 minutes	1 K/min	Tubes
cP_{60}-200-12h	60 nm	200°C	12 hours	1 K/min	Tubes
cP_{60}-250-12h	60 nm	200°C	12 hours	1 K/min	Rods
cP_{35}-250-10m	35 nm	250°C	10 minutes	1 K/min	Tubes
cP_{35}-250-12h	35 nm	250°C	12 hours	1 K/min	Rods

Table 1: Details of the P(VDF-TrFE) nanostructures samples

APPENDIX II

Figure 1 shows the proton NMR spectra for the P(VDF-TrFE) dissolvd in protonated acetone. The peaks between the 2-3.2 PPM corresponds to the VDF unit and the peaks between 5-6 PPM corresponds to the TrFE unit of the P(VDF-TrFE).
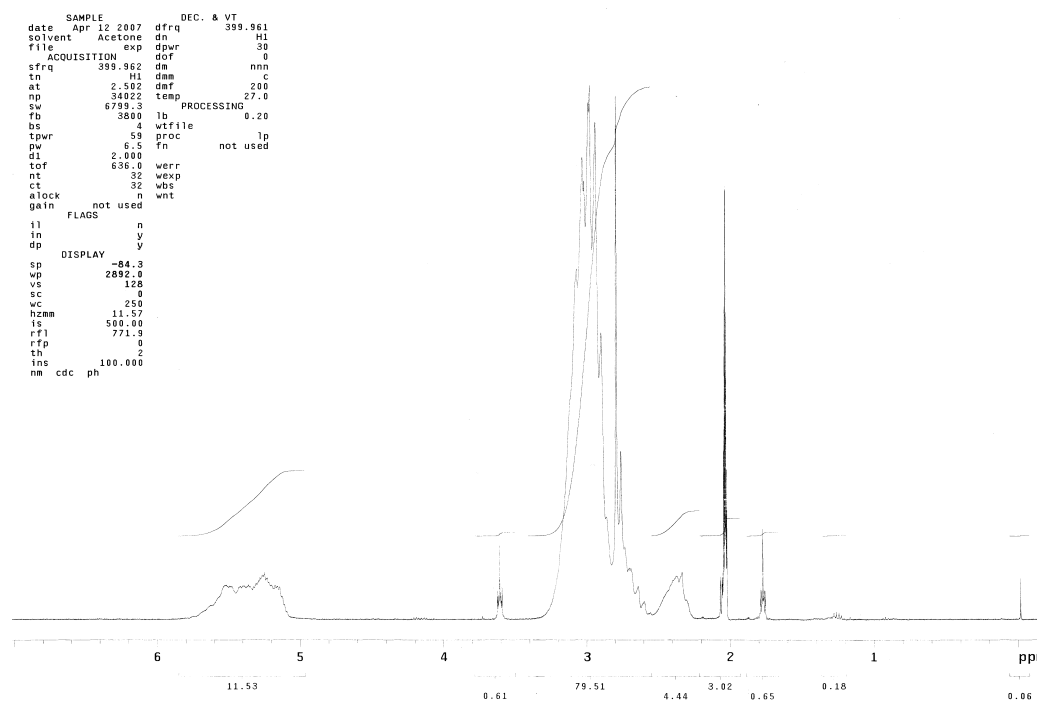

Figure 1: Proton NMR spectra for P(VDF-TrFE)

Acknowledgements

Eidesstattliche Erklärung

Ich erkläre hiermit, dass ich keine anderen als die von mir angegebenen Quellen und Hilfsmittel zur Erstellung meiner Dissertation verwendet habe. Den benutzten Werken wörtlich oder inhaltlich entnommene Stellen sind als solche gekennzeichnet.

Nitin Shingne

Halle (Saale), im December 2010

Curriculum vitae

First Name	Nitin
Family Name	Shingne
Date of Birth	January 7, 1979 (Amravati, India)
Nationality	Indian
E-mail	nitin.shingne@physik.uni-halle.de

EDUCATION

Sept. 2006 - present	Ph.D. candidate in Martin-Luther-University (Halle) and Max Planck Institute of Microstructure Physics (Supervisors: Prof.Dr. Thomas Thurn-Albrecht and Prof.Dr. Martin Steinhart)
Apr. 2004 - June 2006	Masters in Applied Polymer Science (M.Sc.) Martin-Luther-University (Halle)
Jul. 1999 - Jul. 2002	Bachelor of Technology (B.Tech.) College of Engineering and Technology (Akola, India) Amravati University (Amravati, India)
June 1996 - May 1999	Diploma in Polymer Engineering and Technology Government Polytechnic (Amravati, India)

Publication

- Akihiro Sato, Yan Pennec, Nitin Shingne, Thomas Thurn-Albrecht, Wolfgang Knoll, Martin Steinhart, Bahram Djafari-Rouhani and George Fytas "Tuning and Switching the Hypersonic Phononic Properties of Elastic Impedance Contrast Nanocomposites", *ACS Nano*, vol. **4**, pp. 3471-3481, 2010.

List of Presentations

- Nitin Shingne, Markus Geuss, Martin Steinhart, Lili Zhao, Ulrich Goesele, Elke Hempe and Thomas Thurn-Albrecht "Texture Engineering in Nanotubes Consisting of Partially Crystalline Polymers", *MRS fall meeting*, Boston, USA, November 27 - December 01, 2006

- Nitin Shingne, Markus Geuss, Martin Steinhart and Thomas Thurn-Albrecht "Morphology and Crystal Orientation of Ferroelectric P(VDF-ran-TrFE) in Cylindrical Nanopores", *APS March meeting*, Portland (Or.), USA, March 15 - 19, 2010